A Study of Low-Frequency Response of the Atmosphere to the Sea Surface Temperature Variations(Dissertation_全文)

AUTHOR(S):

Kitoh, Akio

主論文

(2)

A Study of Low-Frequency Response of the Atmosphere to the Sea Surface Temperature Variations
(海面水温の変化に対する大気の応答の研究)

鬼頭昭雄

A Numerical Experiment on Sea Surface Temperature Anomalies and Warm Winter in Japan

By Akio Kitoh

Reprinted from the Journal of the Meteorological Society of Japan
Vol. 66, No. 4, August 28, 1988

A Numerical Experiment on Sea Surface Temperature Anomalies and Warm Winter in Japan

By Akio Kitoh

Meteorological Research Institute, Tsukuba, Ibaraki 305, Japan
(Manuscript received 25 March 1988, in revised form 18 June 1988)

Abstract

Impact of the sea surface temperature anomalies (SSTAs) on atmospheric circulations are studied with emphasis on the winter climate in Japan with the use of an atmospheric general circulation model.

The empirical orthogonal function analyses are performed for precipitation, geopotential height at 500 mb and surface air temperature. It is shown that leading eigenvectors of precipitation are zonally elongated in the tropics and that the distribution of positive and negative precipitation anomalies is dependent on the SST and precipitation field in the control run. Surface air temperature in East Asia is mostly governed by the temperature contrast between Japan-East China region and the Sea of Okhotsk. This is associated with high pressure anomalies in the North Pacific Ocean, which weakens the cold surge from Siberia. This circulation is found in the first eigenvector in the present experiment El(Z500) and is dominant in the run which uses the composited January SSTA observed during warm winter in Japan. The simulated anomalies in mid-latitude circulation correspond well with the observations.

An additional run with the SSTA over the equator east of the dateline gives the largest anticyclonic circulation response over the North Pacific Ocean and the warmest surface air temperature anomalies in East Asia. The pattern relevant to warm winter in Japan is not a simple atmospheric response to tropical heating. It is conceivable that inherently there is a dominant circulation mode like El(Z500) and that this mode can be activated either by a direct and/or an indirect orographic effect or by anomalous heating induced by the SSTA. This pattern can be understood as a response to subtropical mass source/sink distribution under the framework of a linear theory.

1. Introduction

Numerical experiments to study atmospheric responses to the sea surface temperature anomalies (SSTAs) were commenced by Rowntree (1972), being inspired by the pioneering work of Bjerknes (1966, 1969). It is followed by Julian and Chervin (1978), Shukla and Wallace (1983), Blackmon *et al.* (1983), Geisler *et al.* (1985) and Tokioka *et al.* (1986a) among others. In particular since the big 1982/83 El Niño, much attention is paid to El Niño and its influence on the atmosphere, and many experiments using the observed 1982/83 El Niño SSTA or an idealized SSTA were performed and intercomparison of model results is made (Nihoul, 1985; WCP, 1986).

The interannual variation of the interaction between the tropics and mid-latitudes during the northern winter has been investigated associated with the El Niño/Southern Oscillation phenomena (*e.g.*, Horel and Wallace, 1981; van Loon and Rogers, 1981; Lau and Chan, 1983a, b). Keshavamurty (1982) performed sensitivity experiments with warm idealized SSTAs over the eastern, central and western equatorial Pacific Ocean during northern summer season with the GFDL GCM and obtained a larger atmospheric response in case of the central and western Pacific anomalies. Simmons *et al.* (1983) and Branstator (1985) show that the winter atmos-

phere is most sensitive to the forcing over the Southeast Asia/Indochina region. A review of the studies of SSTAs and atmospheric circulations in mid-latitudes can be found in Frankignoul (1985).

As to the direct relation between winter climate in Japan and the global SSTAs, several groups have undertaken an analysis of the observational data (*e.g.*, Kawamura, 1984, 1986; Iwasaka *et al.*, 1987). The winter climate in Japan tends to be mild in El Niño years. That was true in 1982/83 and 1986/87 winter, but not in the 1976/77 winter. The surface air temperature in central Japan is shown to have high temporal correlation with warm SSTA over the equatorial central Pacific Ocean, but also with warm SSTA over south and east off Japan, the South China Sea and the Indian Ocean. On the other hand it is reported that SSTA in the North Pacific Ocean is caused by an atmospheric fluctuation (Kawamura, 1984; Iwasaka *et al.*, 1987). Kawamura (1984) claims that warm SSTA off Japan is a result of the weaker cold surge than normal.

The purpose of this experiment is to study whether the SSTA observed in a "warm year" in Japan can produce circulation anomalies relevant to warm Japan, and, if so, to study which SSTA mostly affect those circulation anomalies. Section 2 shows the relation between winter climate in Japan and the SSTA. Section 3 describes the model used and the design of the experiment. The model climate in the control run is briefly shown in Section 4. Characteristics of low-latitude precipitation are studied in Section 5, and mid-latitude circulation variability is examined in terms of geopotential height at 500 mb in Section 6. Discussions are presented in Section 7 and conclusions are made in Section 8.

2. Winter temperature in Japan and global sea surface temperature

a. Surface air temperature in Japan

In order to define years of warm/cold winter in Japan, areal mean surface air temperature in Japan is calculated from twelve climatological observation stations* from 1970 to 1984 (Japan Meteorological Agency, 1980, 1981, 1984, 1987). Here 'winter' is defined as December, January and February, and the year of 1970 represents a mean of December 1969, January 1970 and February 1970. Figure 1 shows the winter temperature anomaly from the 15-year mean. The four warm winters in Japan in the upper quartile of this distribution include 1979, 1973, 1972 and 1983 (in the descending order of temperature anomaly). The four cold winters in Japan of this distribution include 1984, 1977, 1981 and 1974 (in the ascending order). The El Niño years in this period are 1970, 1973, 1977 and 1983 (Rasmusson and Carpenter, 1982; Weare, 1986). Among these four years, two years and one year are selected as warm and cold years in Japan, respectively.

* Sapporo, Nemuro, Akita, Miyako, Wajima, Matsumoto, Yonago, Shionomisaki, Fukuoka, Kagoshima, Shimizu (Ashizuri) and Ishigakijima.

Fig. 1. December-January-February surface air temperature anomalies in Japan calculated from 12 climatological observation stations from 1970 to 1984.

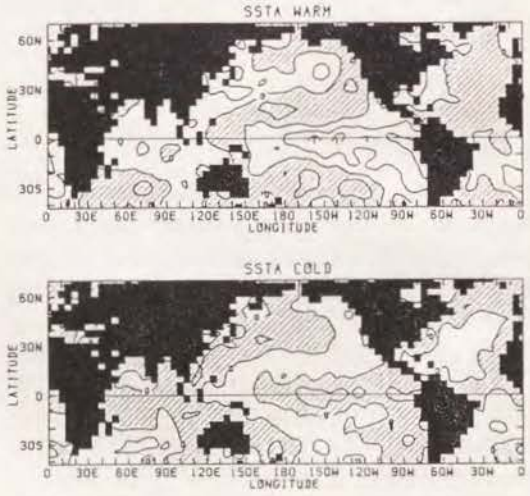

Fig. 2. The composited January sea surface temperature of 1972, 1973, 1979 and 1983 (top) and of 1974, 1977, 1981 and 1984 (bottom). Contour interval is 0.5°C. Negative values are shaded.

b. Sea surface temperature composite

Here the SST averaged for four warm and four cold winters in Japan are compared with the normal SST. The SST data edited by U. S. NOAA north of 40°S from 1970 to 1984 is used and the 15-year mean is defined as the normal SST in the present experiment.

Figure 2 (top) shows the composited SSTA in four Januarys when the surface air temperature in Japan is warm. The SSTA is characterized by a warmer than normal SST in the central and the eastern equatorial Pacific Ocean surrounded by a horseshoe-shaped colder SST in the subtropics. In the western Pacific Ocean, it is warm to the south and east of Japan, in the South China Sea and to the northwest of Australia, while it is cool to the east of the Philippines. It is also warm in the tropical Indian Ocean. In the Atlantic Ocean it is warm in the southen hemisphere and is cold in the northern hemisphere. Among four years used to compose this SSTA, two years (1973 and 1983) are El Niño years and the composited SSTA in the tropical Pacific Ocean still shows the characteristic pattern of El Niño, although its magnitude is smaller than the El Niño composite of Rasmusson and Carpenter (1982).

Figure 2 (bottom) shows the composited SSTA in four Januarys when the surface air temperature in Japan is cold. The pattern in Fig. 2 (bottom) is similar to that in Fig. 2 (top) if the sign is reversed in broad regions in the Pacific and the Indian Ocean.

3. Outline of the model and the design of the experiment

a. Model

The model used is the Meteorological Research Institute GCM (MRI·GCM-I) with a horizontal resolution of 5° in longitude and 4° in latitude. In the computation of radiative heating rate, the model uses Katayama's parameterization (1972). Predicted amount of water vapor and cloud are used in the computation. The dry convective adjustment, middle level convection and penetrative cumulus parameterization by Arakawa and Schubert (1974) are used for parameterizing convective processes as well as the grid-scale condensation due to supersaturation. Surface fluxes of sensible heat, water vapor and momentum are computed by the bulk method with the transfer coefficient proposed by Deardorff (1972). Ground temperature, snow mass and soil moisture (ground wetness) are predicted by considering ground thermodynamics and hydrology after Katayama (1978). Further details of the model are described in Tokioka *et al.* (1984). The January performances of the model are reported by Tokioka *et al.* (1985).

b. Experiment

The control run (C) started from the NMC analysis of 12Z 15 December 1982 and was integrated for one month to 15 January under the seasonal cycle. Then the seasonal march was stopped and the integration was performed for 180 days under the perpetual January condition. The normal SST is used in C.

Eight anomaly runs were performed for 180 days from 15 January of the control run with the SSTAs as summarized in Table 1. Run AW used the composited SSTA (Fig. 2a) for warm winter in Japan, while run AC used the composited SSTA (Fig. 2b) for cold winter in Japan. Runs A1 through A6 were performed mainly to increase the sample size, although their SSTA regions correspond to key regions in AW. They adopted an idealized rectangular SSTA with its maximum of 1.0°C (Fig. 3), which have the positive SSTA over the south maritime continent, the north maritime continent, the Indian Ocean, south of Japan, the central equatorial Pacific Ocean and the negative SSTA east of the Philippines, respectively.

By discarding the first 30 days' data, the remaining 150 days' data in each run were used in the following analyses. For the purpose of empirical orthogonal function (EOF) analyses, 150 days were divided into five 30-day subperiods.

An additional run A7 was also performed with the positive SSTA to the east of the dateline over the equator. This run is not included in the EOF analyses and is independently treated in Section 7.

4. Control run

Before discussing the results obtained in this

Table 1. Summary of numerical simulations

Run C	15-year mean SST from 1970 to 1984
Run AW	composited SST of Januarys in 1972, 1973, 1979 and 1983
Run AC	composited SST of Januarys in 1974, 1977, 1981 and 1984
Run A1	positive SSTA in 105°E-130°E, 14°S-2°S
Run A2	positive SSTA in 105°E-130°E, 2°N-14°N
Run A3	positive SSTA in 55°E-80°E, 14°S-2°S
Run A4	positive SSTA in 125°E-150°E, 18°N-30°N
Run A5	positive SSTA in 165°E-170°W, 14°S-2°S
Run A6	negative SSTA in 125°E-150°E, 2°N-14°N
Run A7	positive SSTA in 180°W-155°W, 6°S-6°N
N	ensemble average of above 9 cases excluding run A7

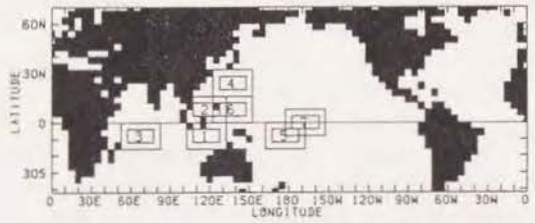

Fig. 3. Sea surface temperature anomalies used in runs A1 through A7. Magnitude is 0.5°C in a large rectangle and 1.0°C in a small rectangle. The sign of SSTA is negative in A6 and positive in the rest.

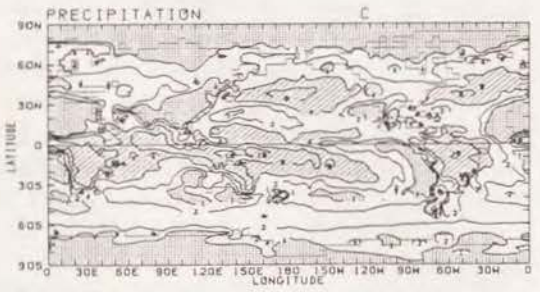

Fig. 4. The precipitation rate in the control run averaged for 150 days. Contours of 1, 2, 4, 8 and 16 mm d^{-1} are drawn. Values greater than 4 mm d^{-1} are shaded and those less than 1 mm d^{-1} are stippled.

experiment, a brief look is made into the model climate in the control run.

Figure 4 shows the horizontal distribution of the 150-day mean precipitation rate in C. Well-organized precipitation areas are found in the tropics except over the eastern oceans where the SST is low. Heavy precipitation greater than 8 mm d^{-1} is simulated over the zonally elongated belt in the south of the equator with its center in the maritime continent, which extends toward the South Pacific Convergence Zone (SPCZ). There is also large precipitation over land in the tropics, *i.e.*, over southern Africa and Brazil. Also found are large precipitation areas over the North Pacific and Atlantic Oceans, which correspond to cyclonically active areas. The control run has produced fairly well the basic climatological characteristics in the precipitation field in this season such as reported by Schutz and Gates (1971).

Overall circulation patterns in the control run also compare favorably with the climatological ones (not shown) and are close to those in Tokioka *et al.* (1985). For example, a subtropical jet at 300 mb with the zonal velocity greater than 70 m s^{-1} is simulated to the southeast of Japan. That over the east coast of North America has a speed of about 45 m s^{-1}. Mid-oceanic troughs are present over the Pacific and Atlantic Oceans in both hemispheres. At the equator, westerlies are found over the eastern Pacific Ocean and over the Atlantic Ocean.

5. Precipitation in low latitudes

a. Local response

Figure 5 shows the 150-day mean precipitation anomaly (AW-C, AC-C, Al-C, ..., A6-C). Anomalies in precipitation and evaporation in Al through A6 averaged over the corresponding anomaly region are shown in columns 4 and 5 of Table 2 together with the SST and precipitation in C. Response of precipitation over the anomaly region is large in A5 and A1. That in A3 and A2

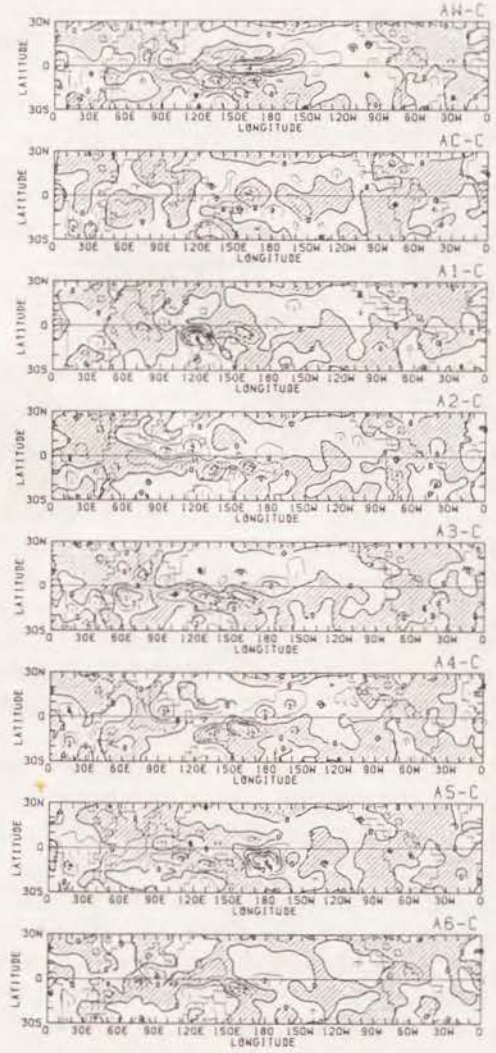

Fig. 5. The 150-day mean precipitation anomaly. Contour interval is 1 mm d^{-1}. Negative values are shaded.

is moderate, while that in A4 is small. The largest response of a local precipitation anomaly is obtained where the normal SST is above 28.5°C and the precipitation in C is great. Thus response to the SSTA is not spatially uniform, but is large where there is lots of precipitation in the control run and the low-level circulation is such that the moisture flux convergence maintains the large precipitation. As shown in Table 2, the contribution of the increased local evaporation has a minor role in the increase of precipitation. The increase in precipitation is largely due to the increased moisture flux convergence induced by the circulation change. This is in agreement with the earlier studies (e.g., Cornejo-Garrido and Stone, 1977; Julian and Chervin, 1978; Shukla and Wallace, 1983; Mechoso *et al.*, 1987).

In A2 and A4, the evaporation even decreases in spite of the increased local SST. The weakened cold surge gives rise to this result.

b. EOF analysis

As shown in the previous subsection, a contribution by the increase in local evaporation is generally less than that by moisture flux convergence, although the relative importance of anomalous evaporation and moisture flux convergence in maintaining anomalous precipitation varies in space (Mechoso *et al.*, 1987). When there is an anomalous increase in precipitation which originates from the prescribed SSTA, or whatever the reason, it is accompanied by an anomalous decrease in precipitation caused by moisture flux divergence. In this subsection the characteristic pattern of anomalous precipitation distribution resulting from this SSTA experiment under the perpetual January condition is

Table 2 Sea surface temperature and precipitation for C averaged over the six SSTA region, and anomalies in precipitation and evaporation in six runs A1 through A6 averaged in their SSTA region.

Region	SST in C	precipitation in C	precipitation anomaly	evaporation anomaly	
1	28.7°C	9.55 mm d^{-1}	+3.89 mm d^{-1}	+0.92 mm d^{-1}	(A1-C)
2	27.1	3.69	+1.87	−0.02	(A2-C)
3	28.0	5.42	+2.26	+0.49	(A3-C)
4	23.0	1.96	+0.45	−0.29	(A4-C)
5	28.9	9.21	+4.82	+1.34	(A5-C)
6	28.2	4.59	−1.05	−0.37	(A6-C)

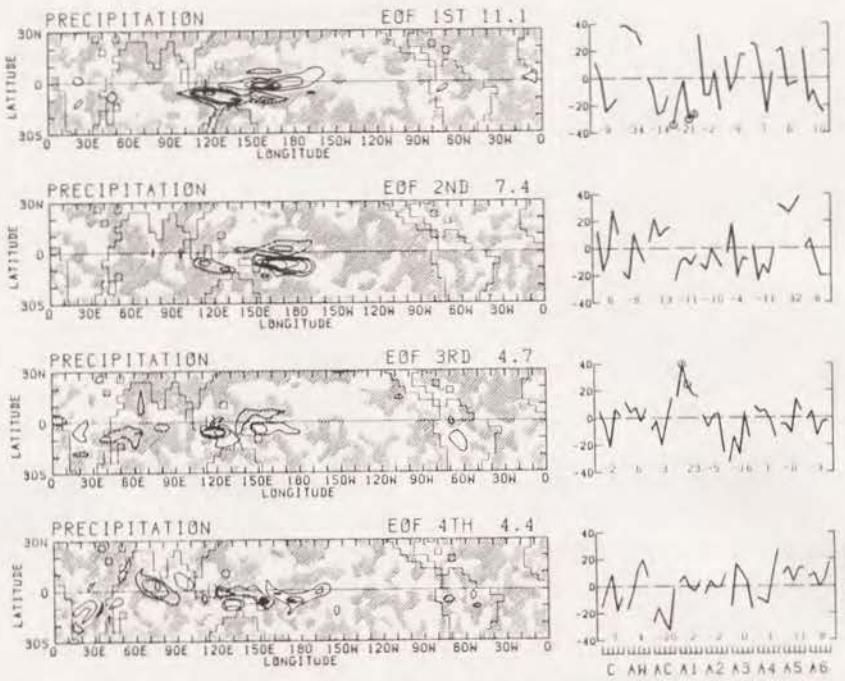

Fig. 6. The leading four eigenvectors (left) and eigencoefficients (right) obtained for precipitation between 30°S and 30°N. Contour interval is 0.04. Negative values are shaded.

investigated by the EOF analysis using the covariance method.

The precipitation data used is the 30-day averaged precipitation on all grid points between 30°S and 30°N. The 150 days' data in each run is divided into five successive 30 days' data. Therefore, at each grid point, there are 45 data from one control and eight anomaly runs.* The first four eigenvectors and eigencoefficients are shown in Fig. 6.

Firstly the zonally elongated precipitation pattern is noted in low latitudes. A similar structure can be seen in a precipitation pattern map for the Pacific Ocean which is associated with the El Niño/Southern Oscillation (Ropelewski and Halpert, 1987).

* To check the stability of the result, the EOF analysis is repeated by reducing grid points by narrowing the region from 0°-360°, 30°S-30°N to 0°-360°, 14°S-14°N, and again to 30°E-150°W, 14°S-14°N. The leading eigenvectors hardly change over the region discussed here, except that the third and fourth eigenvectors obtained in two broader regions appear in the fourth and third eigenvectors in the other, respectively.

The first eigenvector (denoted as El) of precipitation (Pr), El (Pr), explains 11.1% of the total variance. It is characterized by the precipitation anomaly zonally elongated over the equator north of New Guinea. It stretches more than 60° wide from Borneo to the east of the dateline, although its meridional scale is about 8° (2 grids in the model). This region is accompanied with other zonally elongated anomaly regions with opposite sign on both sides. The maximum is located over oceans between Indonesia and Australia (120°E, 6°S), which is contrasted with a center at 150°E, 2°S. It is noted that the precipitation anomalies in El (Pr) show not a small anomaly northeastward from 0°N, 180°E to 16°N, 160°W.

Overall response in the southern hemisphere is larger than that in the northern hemisphere. Since the present experiment is performed under the perpetual January condition, the SST in the control run is higher in the southern hemisphere than in the northern hemisphere and the precipitation is also larger in the southern hemisphere. It is inferred that meridional

asymmetry in the precipitation variability is due to this experimental condition.

The coefficient of El (Pr), denoted as Cl (Pr), shows that AW, Al and AC are the main contributors to El (Pr). AW has consistently large coefficients in all five subperiods. On the other hand, Al and AC have negative values of coefficients, indicating large positive precipitation anomalies between Indonesia and Australia accompanied by negative ones over the equator to the northeast of the positive anomalies.

E2 (Pr) (7.4%) is mainly explained by A5. When there are positive precipitation anomalies to the east of New Guinea, the counteracting negative anomalies appear in a zonally elongated band to the north of it and over the maritime continent to the west of New Guinea. AC, Al and A4 have moderate contributions to this mode.

A1 and A3 have mostly contributed to E3 (Pr) (4.7%). When precipitation in the south maritime continent is large, there are positive anomalies south of the equator and negative anomalies north of the equator between 120°E and 180°E. At the same time there are large negative anomalies in the western Indian Ocean. This anomaly is paired with the anomaly of opposite sign in Central Africa.

The fourth component (E4 (Pr), 4.4%) has a smaller spatial scale of anomalies than the preceding three EOFs. E4 (Pr) is characterized by chains of positive and negative anomalies in equatorial latitudes in the eastern hemisphere from Africa to the dateline. The coefficients of AC show large negative values in four out of five subperiods.

It is indicated that A1, in which the positive SSTA is assigned over the south maritime continent, shows large contributions both in El (Pr) and E3 (Pr). Figure 6 shows that the magnitude of Cl (Pr) is large in subperiods 1, 4 and 5 of Al, and that of C3 (Pr) is large in subperiods 2 and 3 of Al, as marked by open circles. In the 150-day mean precipitation anomaly map (Fig. 5), positive precipitation anomalies over the SSTA region are flanked with two negative anomalies on the eastern and western sides. Clear distinction into two subperiods (1-4-5) and (2-3) of the eigencoefficients of Al suggests that the eastern and western pairs of precipitation anomalies occurred independently, resulting in one positive and two negative anomalies in the long-term mean. These precipitation anomalies are accompanied by an east-west circulation. This east-west cell, with its center over the maritime continent and its width of about 60°, can exist on both sides. However, these two east-west cells do not appear simultaneously, but either cell appears at one time.

6. Mid-latitude circulation

a. Geopotential height

The 30-day averaged grid data of geopotential height at 500 mb (Z500) are transformed into spherical harmonic functions which have a zonal wavenumber up to 8 and meridional nodes up to 13 as in Tokioka *et al.* (1986a). The EOF analysis is applied for this time series data of truncated modes. Figure 7 shows the first and second eigenvectors of Z500. El (Z500) explains 33.8% of the total variance and is characterized by the high pressure region (if a coefficient is positive) over the North Pacific Ocean and the low pressure region over northern Siberia. The former has a center at 165°W, 42°N, but extends toward Japan. Zonally symmetric anomalies are also noted.

Figure 7 also shows Cl (Z500). By looking at individual 30-day subperiods, large coefficients are scattered in different runs. For example, the first six largest Cl (Z500) are found in separate runs. But AW has consistently positive coefficients and the mean coefficient becomes the largest (a mean of the coefficients of five subperiods, C1M, is 26). Therefore a high pressure anomaly in the North Pacific Ocean is the strongest. A4 (C1M = 19) and A3 (C1M = 9) follows that. On the other hand, a low pressure anomaly is strong in C (C1M = −20), A6 (C1M = −14) and AC (C1M = −10) in the 150-day mean.

E2 (Z500) explains 13.4% of the total variance and is characterized by eddies in northern high latitudes around North America. This pattern corresponds to the intensity of the Aleutian low. C2M is the largest in A5 and the smallest in A2.

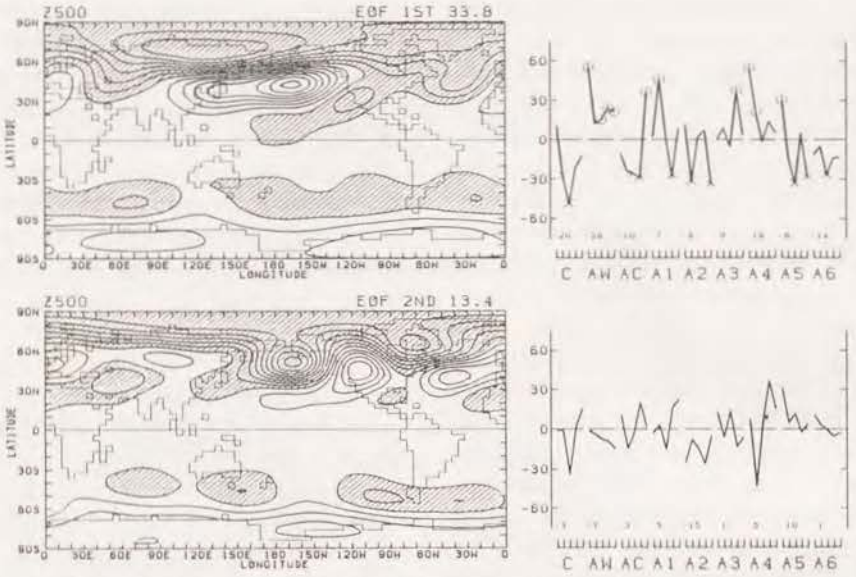

Fig. 7. The first (top) and second (bottom) eigenvectors and their coefficients for geopotential height at 500 mb. Contour interval is 0.5. Negative values are shaded. Open circles and crosses in eigencoefficients of EOF1 indicate the subperiods with the ten largest and smallest values referenced in the text.

b. Surface air temperature

E1 (Z500) has a good correspondence with wintertime temperature in Japan. A composite is taken for 10 subperiods when C1 (Z500) is large (indicated by open circles in Fig. 7 (top)) and small (crosses in Fig. 7 (top)). A composite for surface air temperature (Ts) is shown in Fig. 8. This pattern is very similar to E2 (Ts), which is shown in Fig. 9 together with E1 (Ts). E1 (Ts) explains 17.6% of the total variance. Its variance is almost confined in high latitudes in the northern hemisphere north of 50°N. E2 (Ts) explains 15.4% of the total variance and is characterized by a large temperature contrast between East Asia and the Sea of Okhotsk. A composited mean surface air temperature anomaly map of 10 subperiods when Ts over Japan is warm (not shown) is almost identical to Fig. 8 (top).

The correlation coefficient between C1 (Z500) and C2 (Ts) is 0.83. This high correlation is because the mid-latitude circulation response is quasi-barotropic and the anomalous warm surface air temperature in East Asia is mainly caused by anomalous warm advection by southerly winds or a weakened cold surge at the western edge of high pressure anomalies over the North Pacific Ocean. Therefore in the present experiment Japan experiences a warm (cold)

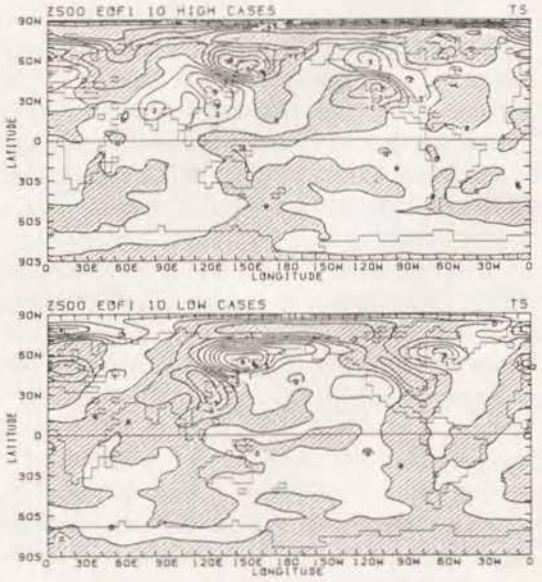

Fig. 8. The surface air temperature anomaly composited for 10 subperiods when C1 (Z500) is large (top) and small (bottom). Contour interval is 1.0°C. Negative values are shaded.

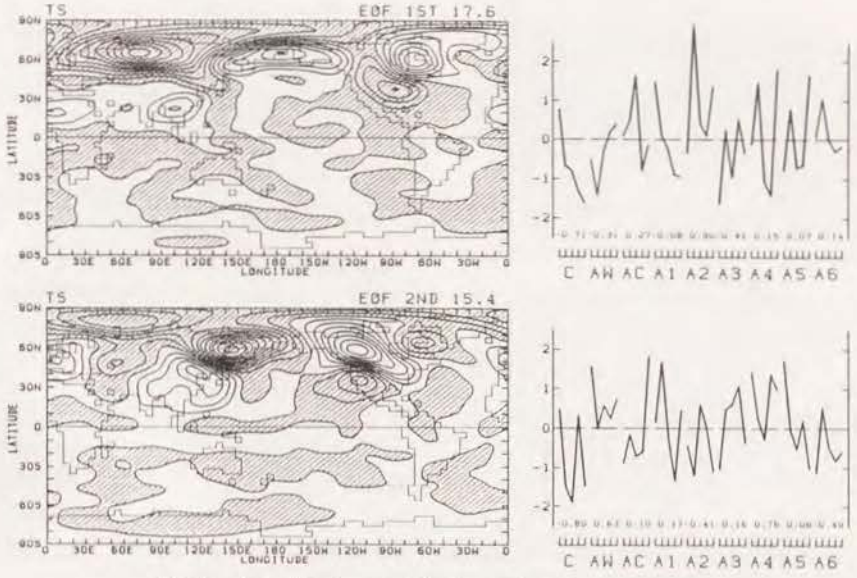

Fig. 9. As in Fig. 7 except for the surface air temperature.

winter when C1 (Z500) is positive (negative). From Fig. 7, AW, where the SSTA observed during warm winter in Japan are prescribed, results in the warmest temperature in Japan.

In six runs A1 through A6, a characteristic SSTA from the composited SSTA distribution during warm winter in Japan is selected and occurs in six different regions. Among them, run A4, where a positive SSTA occurs to the south of Japan, gives the second largest C1 (Z500) and the largest C2 (Ts), resulting in a warm winter in Japan comparable to AW and the corresponding circulation anomalies.

The coldest winter in Japan is simulated in AC, where the characteristic SSTA of cold winter in Japan occurs. On the other hand, it is run C without any SSTA that has the minimum C1 (Z500) and the minimum C2 (Ts).

c. Comparison with the observation

We shall compare our results with observations. Figure 10 shows the 150-day mean sea level pressure anomalies in AW and AC from the mean of all nine cases (N). In this paper, a mid-latitude circulation anomaly relevant to a warm winter in Japan is sought as an intrinsic mode of the atmosphere. Introduction of an EOF analysis is made on this standpoint. The "normal" climate should be an ensemble mean of many realizations obtained by using different SSTs, and is not C, which is only one realization obtained by using a normal SST. Thus N instead of C is used as a reference of anomalies.

As C is the case in which C1 (Z500) is the minimum in nine cases, an anomaly map of AC relative to C is very different from that in Fig. 10. In C-N a cyclonic sea level pressure anomaly in the North Pacific Ocean is dominant with −8 mb in its central part (not shown). The pattern of AW-C is similar to that of AW-N. Also shown are the observed January sea level pressure anomalies in warm and cold winters defined in Section 2 from the 15-year mean. Observed data are provided by the Japan Meteorological Agency but covers only the northern hemisphere with a resolution of 10° by 10°.

In both warm and cold winters, sea level pressure anomalies are characterized by a hemispheric spatial scale with positive and negative anomalies over the North Pacific Ocean and northern Eurasia. The January sea level pressure anomalies in both the warm and cold winters are reproduced well by experiments AW-N and AC-N, especially in the eastern hemisphere.

Figure 11 shows the 150-day mean surface air temperature anomalies obtained in AW-N and AC-N. Observed anomalies are calculated from

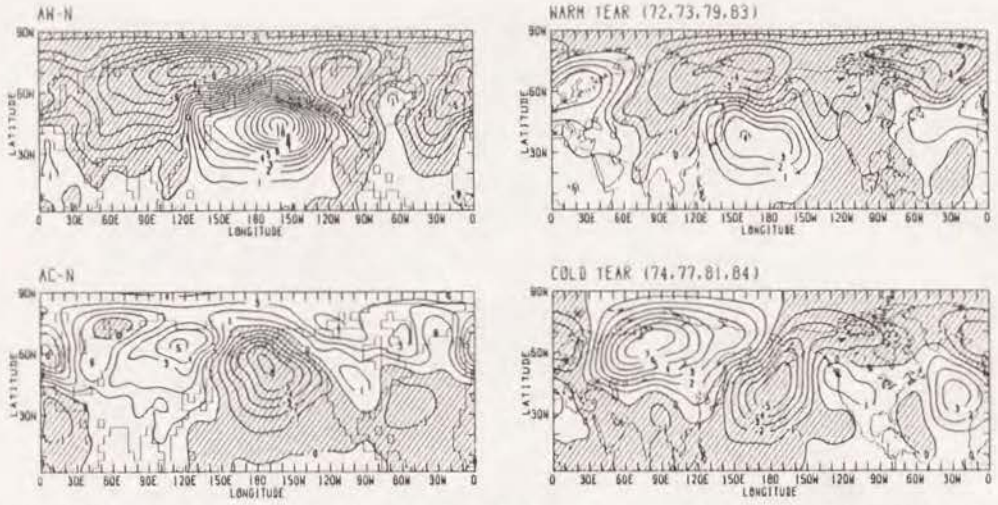

Fig. 10. Comparison with the 150-day mean sea level pressure anomalies for AW and AC from the means of all nine cases and the corresponding observations composited for four warm and cold Januarys in Japan between 1970 and 1984. Contour interval is 1 mb. Negative values are shaded.

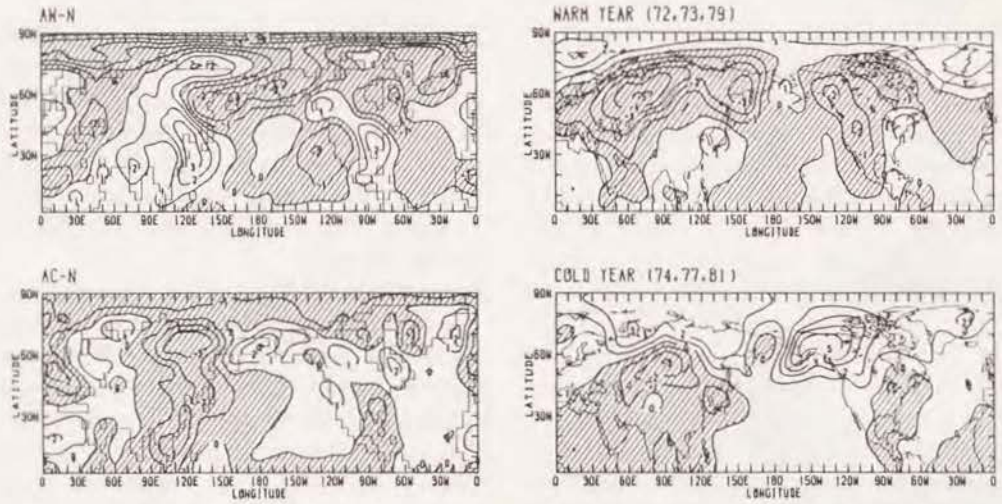

Fig. 11. Comparison with the 150-day mean surface air temperature anomalies for AW and AC from the means of all nine cases and the corresponding observations (Robock, 1982) composited for three warm and cold Januarys in Japan between 1970 and 1981. Contour interval is 1°C. Negative values are shaded.

the northern hemisphere surface air temperature anomaly dataset by Robock (1982). This dataset covers the northern hemisphere with a resolution of 5° in latitude and 10° in longitude from January 1891 to December 1981. Therefore, to compose surface air temperature anomalies, January data from 1970 to 1981 are used, where Januarys of 1972, 1973 and 1979 are chosen for the warm years and those of 1974, 1977 and 1981 are chosen for the cold years.

As suggested from a close relationship between E1 (Z500) and E2 (Ts), and a large contribution of E1 (Z500) by AW (Fig. 7), the surface air temperature distribution in AW-N resembles E2 (Ts). It is warm in broad areas in the eastern half of the Eurasian continent with its maximum over the East China Sea. It contrasts well with colder temperature over the Sea of Okhotsk and the Bering Sea. This northeast-southwest contrast of surface air

temperature with its node around North Japan resembles the observed pattern. This has a close relation with the finding by Miyazaki, Tanaka and Matsubayashi (1986, personal communications) that temperature over Japan tends to be above normal in winters of the mature phase of El Niño, but that it is statistically significant only in the Ryukyu islands. These temperature distributions correspond with wind anomalies near the surface.

Another large temperature anomaly in observations can be found in North America. It is warm in the eastern United States and cold in the rest of North America, which is associated with an anomalous trough over Canada and a ridge in the North Atlantic Ocean. These features in and around North America are seen in AW-N.

The surface air temperature anomalies obtained in AC-N are highlighted with the temperature contrast between the western and eastern peripheries of the North Pacific Ocean. Both the Siberian high and the Aleutian low are strong (Fig. 10). These bring cold arctic air into East Siberia and the cold surge over East Asia is strong. In the western part of North America, including Alaska, anomalous southerly winds bring about warm temperature anomalies. These features are in reasonable agreement with the observation. However the observed temperature distribution over northern Eurasia is not simulated and may not be explained solely by the sea surface temperature anomalies.

7. Discussions

a. Relationship between precipitation and circulation anomalies

In the previous section, it is shown that the circulation pattern which affects the winter climate in East Asia has a hemispheric scale and is particularly related with geopotential height anomalies around 40°N. In this subsection relationships between precipitation and circulation anomalies will be examined.

A composite map for the precipitation anomalies taken for 10 subperiods when C1 (Z500) is large is shown in Fig. 12. The spatial pattern of this mode is characterized by positive precipitation anomalies over a narrow belt on the equator over the western Pacific Ocean westward

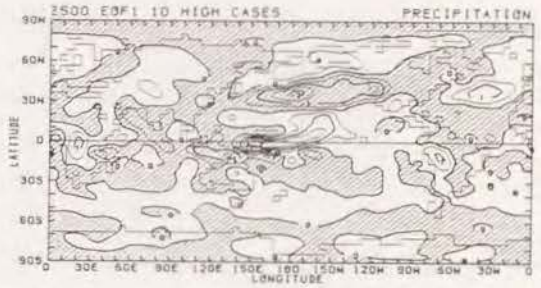

Fig. 12. As in Fig. 8 (top) except for the precipitation. Contour interval is 0.5 mm d^{-1}. Negative values are shaded.

of the dateline and around Hawaii, and negative ones between Indonesia and Australia and the North Pacific Ocean with a center around 40°N. Anomalous precipitation distribution in low latitudes resembles that found in El (Pr) shown in Fig. 6. The correlation coefficient between C1 (Pr) and C1 (Z500) is 0.53, but eight out of 10 cases with large C1 (Z500) have also large C1 (Pr) (see Figs. 6 and 7). Figure 12 indicates that the low-latitude precipitation pattern extracted from the EOF analysis has a close relationship with the mid-latitude circulation pattern, which strongly affects the surface temperature distribution in East Asia.

It is also indicated from Figs. 6 and 7 that a large portion of the total variance in E1 (Pr) and E1 (Z500) comes from run AW. However, even if five subperiods for AW are removed from compositing Figs. 8 and 12, the results (not shown) do not change much, only reducing the magnitude of a pair of strong precipitation anomalies between the maritime continent and northeast of New Guinea. In the composite map without AW, there are still positive precipitation anomalies over northeast of New Guinea on the equator and over a large part in the central Pacific Ocean between the equator and 20°N with its maximum south of Hawaii and a broad negative precipitation anomaly area in the central North Pacific Ocean.

Figure 13 shows the correlation coefficient map between grid values of precipitation anomalies in 45 subperiods and C1 (Z500). Regions with high correlation are found over the North Pacific Ocean. The precipitation anomaly south of Hawaii (155°W, 14°N) is highly

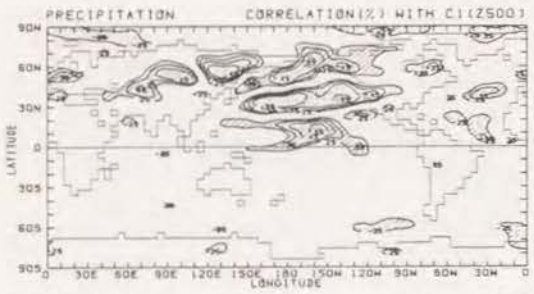

Fig. 13. Correlation map between precipitation and C1 (Z500) based on the 30-day mean values. Values larger than 25% are drawn with contour interval of 10%.

correlated with C1 (Z500). The moisture which is required for this precipitation anomaly comes from the southwest. A moisture budget analysis reveals that the weakened westerlies due to high pressure anomalies are responsible for the negative evaporation anomalies over the North Pacific Ocean around 40°N, which cause the negative precipitation anomalies there. The positive precipitation anomalies over Alaska are due to the anomalous westerly moisture flux and its convergence from the Bering Sea and the Sea of Okhotsk. Thus, the precipitation anomalies in northern mid-latitudes have been closely tied to mid-latitude circulation changes.

b. Additional run

Since it is shown that the heating anomaly around the dateline near the equator correlates well with the mid-latitude circulation pattern which mostly affects the climate in East Asia, an additional run was performed to test this relationship. This run, A7, used a positive SSTA to the east of the dateline on the equator, i.e., 180°–155°W, 6°S–6°N (see Fig. 3), with the maximum of 1°C in the central part of this anomaly region.

The top panel of Fig. 14 shows the result, A7-N, for precipitation. There is a large positive anomaly over the SSTA region at the equator. A large asymmetry with respect to the equator exists. Positive anomalies extend northeastward and join a positive anomaly belt at 20°N. This contrasts with large negative anomalies east of New Guinea at 10°S. Thus, the precipitation anomaly map obtained in A7-N is similar to Fig. 12. A sea level pressure anomaly map (Fig. 14,

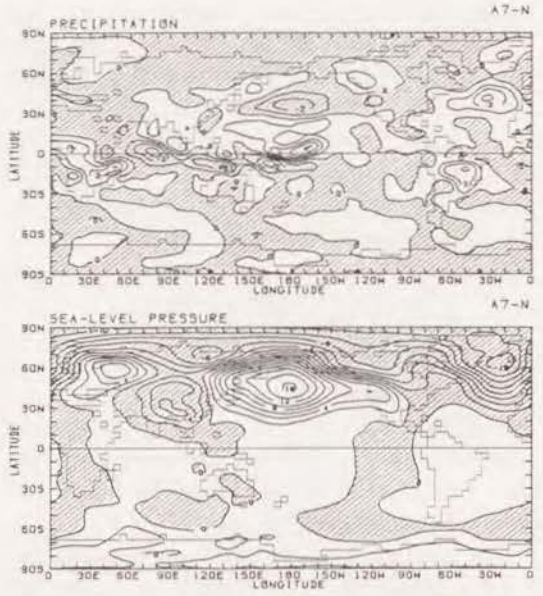

Fig. 14. The 150-day mean anomalies (A7-N) for precipitation (top) and sea level pressure (bottom). Contour intervals are 1 mm d^{-1} and 2 mb, respectively. Negative values are shaded.

bottom) shows strong high pressure anomalies over the entire North Pacific Ocean, which have a quasi-barotropic structure. Run A7 also shows warm surface air temperature anomalies over East Asia with its center in South China (not shown). It is noteworthy that the sea level pressure response in A7 is much stronger than in any other run. This again suggests the preference of the positive SSTA near the dateline on the equator, which creates heating anomalies between 180°E, 0°N and Hawaii, for producing anticyclonic mid-latitude circulation anomalies. This SSTA region is included in the NINO4 region, 160°E–150°W, 5°S–5°N, defined by the Climate Analysis Center of NMC.

c. Interpretation of mid-latitude response

A steady-state atmospheric response to an equatorial forcing is studied by Matsuno (1966), Gill (1980), Lau and Lim (1982), Lim and Chang (1983) and Heckley and Gill (1984). It is shown that for an isolated heat source over the equator, the Kelvin and the gravest Rossby modes dominate in the tropics. However, our present results are not simply explained by this scenario. The stationary stream function and velocity

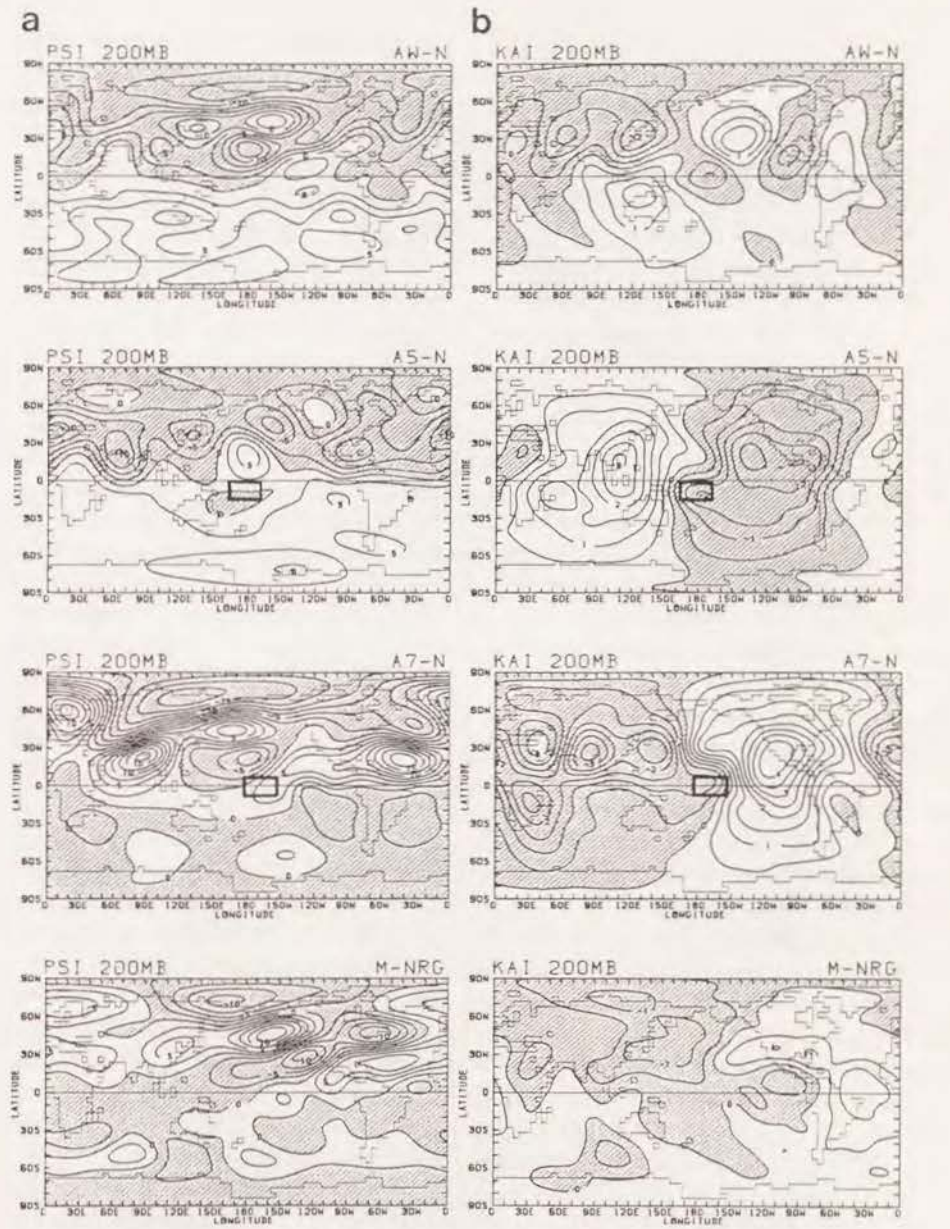

Fig. 15. (a) The 150-day mean stream function anomalies at 200 mb for AW-N, A5-N and A7-N. The bottom panel shows the stream function response at 200 mb to the Rockies plus Greenland forcing in M-NRG (Tokioka and Noda, 1986). Contour interval is 2.5×10^6 m^2 s^{-1}. Negative values (cyclonic circulation in the Northern Hemisphere) are shaded. Rectangles in A5-N and A7-N represent the areas where the SSTAs are imposed. (b) As in (a) except for the velocity potential at 200 mb. Contour interval is 0.5×10^6 m^2 s^{-1}.

potential anomalies at 200 mb in AW-N, A5-N and A7-N are shown in Fig. 15. Deep anomalous heating in AW exists around the dateline on the equator (Fig. 5). The stream function anomaly at 200 mb in AW is characterized by a cyclonic circulation to the north of the heating maximum. This is not attained directly by any equatorial forcing or a linear superposition of them. However, in A5 a different circulation pattern is found, which is similar to a heat induced tropical circulation. In this case anticyclones at 200 mb are found at the longitudes of the heating, not to the west of the heating, in both hemispheres. Hendon (1986) shows that this eastward shift of anticyclones from the position predicted by a linear theory results from the nonlinear response due to the larger forcing. A PNA (Pacific/North America)-like pattern, starting from an anticyclonic circulation west of Hawaii, covers the North Pacific Ocean and North America.

It is noteworthy that the response in A7 is closer to that in AW than that in A5. This indicates that although the SSTAs in A5 and A7 are similar in magnitude and are close in their positions, the atmospheric response is quite different, implying a high sensitivity of it to the precise position of the SSTA. Atmospheric responses obtained in some GCM studies (e.g., Blackmon *et al.*, 1983; Geisler *et al.*, 1985) which used a large El Niño SST such as that in 1982/83 winter rather resemble those obtained in A5. Tokioka *et al.* (1986a) found different atmospheric responses to the composited SSTA by Rasmusson and Carpenter (1982) when they used the whole SSTA as compared to the SSTA westward of 140°E eliminated. The latter case produced a PNA-like pattern, somewhat similar to that in A5. It should be stressed that the SSTA distribution in AW is not quite the same as the El Niño composite of Rasmusson and Carpenter (1982), again implying a high sensitivity of the atmospheric response to the characteristics of the SSTA.

A surprisingly similar atmospheric response to that in AW has been obtained in an orography experiment by Tokioka and Noda (1986). They have compared the stationary eddy response, under the perpetual January mode, of the atmosphere without mountains in North America and Greenland (NRG) with that in the control run (M). The difference in stream function and velocity potential at 200 mb, M-NRG, is shown in the bottom panel of Fig. 15. The similarity between this and AW-N or E1 (Z500) in the northern hemisphere is noted. The vertically integrated diabatic heating anomalies in M-NRG (Fig. 2 in Tokioka and Noda, 1986) also resemble Fig. 12 in the present experiment. Note that any anomaly in M-NRG may not be a direct response to orography but a result of nonlinear interaction among orographic forcing, diabatic heating and transient eddy forcing. It may be that there is a dominant circulation mode in this model as extracted in E1 (Z500) and this mode is activated either by an orographic effect of the Rockies through a direct and/or an indirect response, or by an anomalous heating induced by the SSTA. Moreover, this characteristic mode may not be a fabrication of this particular model, as the anomalous circulations obtained in this experiment capture some of the composited observations at least over the North Pacific Ocean and its surroundings (Figs. 10 and 11).

To ascertain the hypothesis that E1 (Z500) is an intrinsic mode in the northern mid-latitude atmosphere, the EOFs of Z500 in three different datasets are compared in Fig. 16. Figure 16a shows the first four eigenvectors (denoted as R1 through R4) obtained for the observed monthly northern hemisphere Z500 in January, February and December in a 41-year period from 1946 to 1986. R1 corresponds to the PNA pattern named by Wallace and Gutzler (1981). R2, R3 and R4 correspond to the eastern Atlantic (EA), the western Atlantic (WA) and the western Pacific (WP) patterns, respectively.

Figure 16b shows the first four eigenvectors (G1 through G4) obtained from a 12-year integration of the MRI-GCM-I (Tokioka *et al.*, 1986b). The integration is performed with the prescribed SST, which changes seasonally but has no year-to-year variation. G1, G2, G3 and G4 correspond to R2, R3, R1 and R4, respectively. The pattern correlation coefficient between G1 and R2, PCC (G1,R2), calculated in a region between 20°N and 80°N is −0.76, and PCC (G2,R3) is −0.50, PCC (G3,R1) is 0.58 and PCC (G4,R4) is 0.68. The model reproduces the

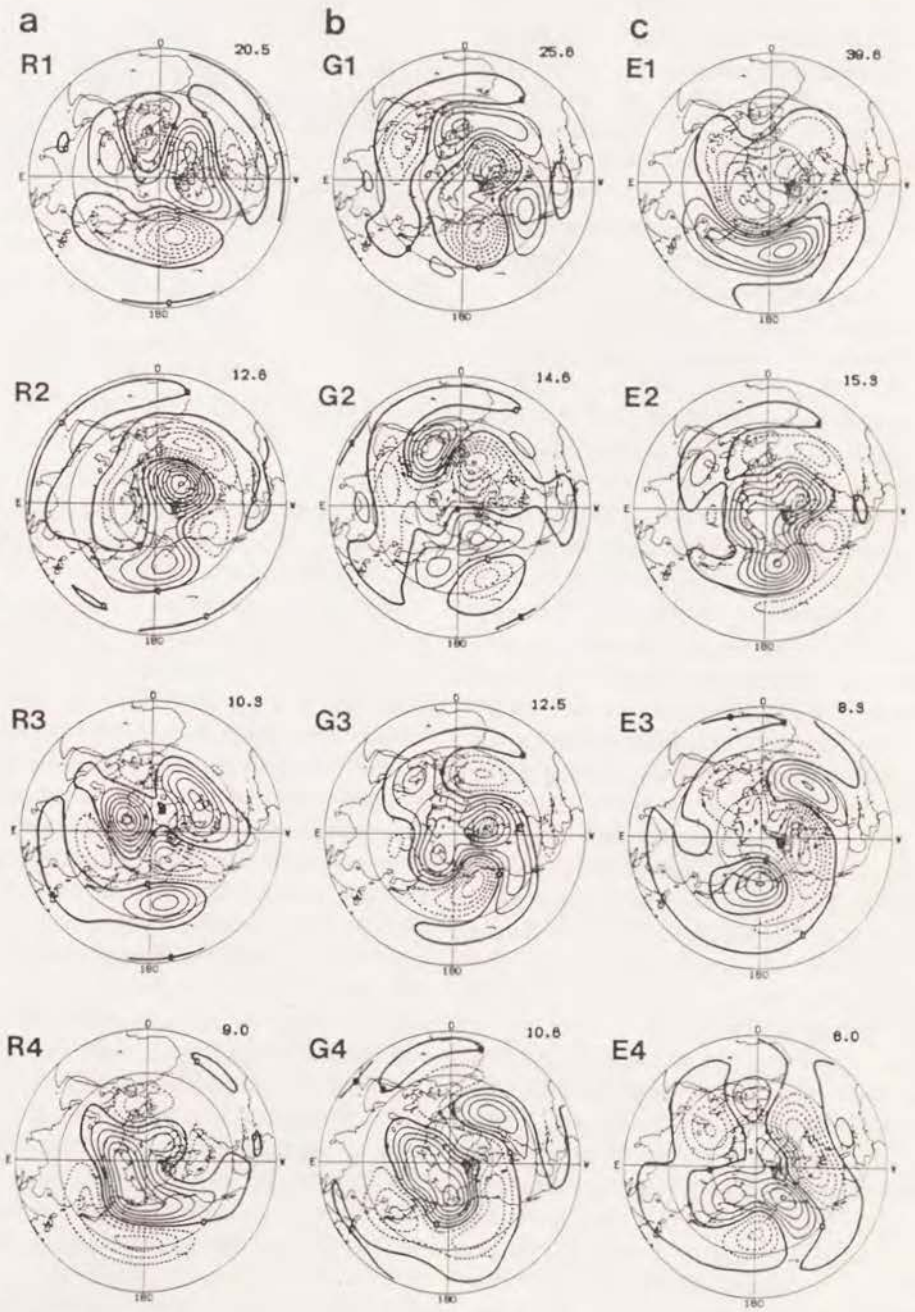

Fig. 16. The first four eigenvectors for geopotential height at 500 mb in the Northern Hemisphere. (a) Observations. Monthly means for January, February and December in 41 years from 1946 to 1986 are used. n (sample size) = 123. (b) 12-year run of the MRI-GCM-I (Tokioka *et al.*, 1986b). Monthly means for December, January and February are used. n = 36. (c) The present experiment. Same as in Fig. 7 except that only the northern hemisphere data are used. n = 45.

observed low-frequency variability patterns reasonably. The difference is that the PNA is weaker in the model than in the observation. Considering that no year-to-year variation of the SST is allowed in the model, the observed PNA mode seems to be highly influenced by a variable SST such as El Niño. Further comparison of the low-frequency variability of the atmosphere between the observation and the 12-year run will be the subject of a future paper.

Figure 16c shows E1 through E4 obtained in this experiment. PCC (E1,G4) is −0.73 and PCC (E2,G1) is −0.88. This indicates that the northern mid-latitude atmosphere has an intrinsic variation pattern such as E1 (Z500), which is closely related with warm winter in Japan, in this model and also in the observation. Resemblance of this mode to M-NRG suggests that this intrinsic mode is closely related with the existence of orography. Moreover, the fact that this mode is obtained as the first eigenvector in this experiment implies the positive role of the SSTA in increasing the variability of this mode.

It is already shown that the response in A5 can be understood as a circulation induced by an anomalous heating due to the SSTA. However the response in A7 or AW is quite different from that in A5 (Fig. 15). The pattern in A7 or AW can be understood as a response to subtropical mass source/sink distribution under the framework of a linear theory. To show this, the linearized shallow-water equation model by Grose and Hoskins (1979) is used.

It is shown in Fig. 15 that in AW and A7, the convergence in the upper troposphere in the eastern Pacific Ocean around 30°N forms a pair with the divergence in East Asia. They are very different from the anomalous divergent circulation in A5. Figure 17 shows a steady stream function response to a mass source at 140°E, 30°N and a mass sink at 140°W, 30°N with the same magnitude calculated by the use of the linear shallow-water model. The zonally averaged zonal wind at 200 mb in C is used as a basic field and the shape of the forcing is circular with a radius of 10°. The orography is not considered. Other details are the same as in Grose and Hoskins (1979). This map picks up some of the salient features appearing in AW-N in the North

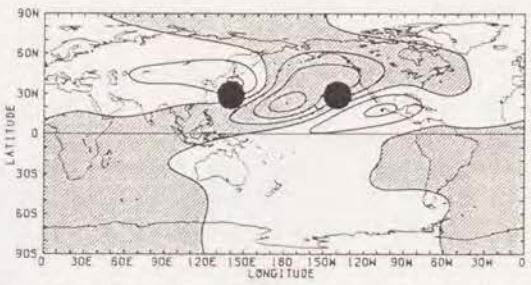

Fig. 17. A steady stream function response in the linear shallow-water model forced by mass source at 140°E, 30°N and mass sink at 140°W, 30°N (black circles). The zonally averaged zonal wind at 200 mb for C is used. Contour interval is arbitrary. Negative values are shaded.

Pacific Ocean. On the other hand, the mass source around the dateline at the equator yields a subtropical anticyclone pair and an extratropical wave train like that found in A5-N.

Held and Kang (1987) showed that subtropical divergence anomalies are of more importance than tropical anomalies in generating the extratropical wave train in a barotropic model because the divergence term becomes dominant in extratropics in vorticity generation. The reason for generating such an mass source/sink distribution should be sought in future research. There are some possibilities, including a possible role of a tropically forced Rossby wave in creating the subtropical divergence anomaly as suggested by Held and Kang (1987), as well as the interactions between the tropical forcings and a subtropical jet (Lau and Boyle, 1987), or the zonally averaged zonal wind (Kang and Lau, 1986). In the present experiment the prescribed SSTA to the south of Japan (run A4) results in large C1 (Z500), bringing less cold surge there. This suggests the possibility of directly creating a subtropical mass source or sink by mid-latitude SSTAs. As to the relationship between mid-latitude SSTAs and circulation anomalies, Kawamura (1984, 1986) and Iwasaka *et al.* (1987) show by lag-correlation analysis that the SSTA near Japan is highly correlated with the mid-latitude circulation one-month before in winter. The present experiment suggests that the warm SST over the western Pacific Ocean is not only modulated by thermal forcing (cold surge) of the atmosphere, but also may contribute to

forming such a circulation to some extent.

8. Conclusions

One control (C) and nine anomaly runs (AW, AC, A1, ... A7) under the perpetual January condition are performed to investigate the impact of sea surface temperature anomalies on atmospheric circulations with emphasis on the winter climate in Japan.

Run AW (AC) uses the composited SSTA of 1972, 1973, 1979 and 1983 (1974, 1977, 1981 and 1984) when Japan experienced warm (cold) winters between 1970 and 1984. Runs A1 through A6 use an idealized rectangular SSTA with its maximum of 1°C, which is positive over the south maritime continent, the north maritime continent, the Indian Ocean, south of Japan, the central equatorial Pacific Ocean and negative east of the Philippines, respectively. An additional run A7 specifies a positive SSTA over the equator to the east of the dateline. Each run has been integrated for 180 days and the last 150 days' data are used for the analysis.

The EOF analyses based on the 30-day average model data for 500 mb height, surface air temperature and precipitation are performed. It is shown that leading eigenvectors of precipitation are zonally elongated in the tropics and the distribution of a pair of positive and negative precipitation anomalies is highly dependent on the SST and precipitation field in the control run.

E1 (Z500) has a tendency to appear simultaneously with E2 (Ts). These eigenvectors are associated with a height anomaly over the North Pacific Ocean and warm temperature over China-Japan region and cold temperature over the Sea of Okhotsk. Run AW has the highest scores of C1 (Z500), resulting in the warmest Japan in the experiment. A4 (warm SSTA to the south of Japan) follows AW, in which the cold surge from Siberia is weak over China and Japan. On the other hand, run C (control experiment without any SSTA), A6 (cold SSTA to the east of the Philippines) and AC show the three small C1 (Z500). The simulated anomalies in mid-latitude circulation and surface air temperature for AW and AC are comparable to the composited observations in the North Pacific Ocean and its surroundings, suggesting the importance of the SSTAs as boundary forcings.

There is a high correlation between C1 (Pr) and C1 (Z500). The spatial pattern of this precipitation mode is characterized by positive anomalies over a narrow belt on the equator over the western Pacific Ocean westward of the dateline and to the south of Hawaii, and has negative ones between Indonesia and Australia, and over the North Pacific Ocean with its center at 40°N. It is indicated that a heating anomaly south of Hawaii is highly correlated with C1 (Z500). It is also suggested by an additional run that the SSTA just to the east of the dateline on the equator is effective in producing such a heating and circulation anomaly.

The response obtained in AW is not a simple atmospheric response to tropical heating. It is conceivable that there is inherently a dominant circulation mode like E1 (Z500) and that this mode can be activated either by a direct and/or an indirect orographic effect, or by an anomalous heating induced by the SSTA. This pattern can be understood as a response to subtropical mass source/sink distribution under the framework of a linear theory.

Acknowledgments

The author is grateful to Dr. T. Tokioka of MRI for his initial guidance, continuous encouragements and discussions throughout this work. He thanks Messrs. M. Ohzeki and Y. Tsuyuki of JMA for kindly providing him a program of the linearized shallow-water equation model. Thanks are extended to Dr. K. Yamazaki of MRI for discussions and two reviewers for comments to the original manuscript.

Computations are made with HITAC S810 at MRI.

References

Arakawa, A. and W.H. Schubert, 1974: Interaction of a cumulus cloud ensemble with the large-scale environment. Part I. *J. Atmos. Sci.*, **31**, 674-701.

Bjerknes, J., 1966: A possible response of the atmospheric Hadley circulation to equatorial anomalies of ocean temperature. *Tellus*, **18**, 820-829.

———, 1969: Atmospheric teleconnections from the equatorial Pacific. *Mon. Wea. Rev.*, **97**, 163-172.

Blackmon, M.L., J.E. Geisler and E.J. Pitcher, 1983: A general circulation model study of January climate anomaly patterns associated with interannual variation of equatorial Pacific sea surface temperatures. *J. Atmos. Sci.*, **40,** 1410-1425.

Branstator, G., 1985: Analysis of general circulation model sea-surface temperature anomaly simulation using a linear model. Part I: Forced solution. *J. Atmos. Sci.*, **42,** 2225-2241.

Cornejo-Garrido, A.G. and P.H. Stone, 1977: On the heat balance of the Walker circulation. *J. Atmos. Sci.*, **34,** 1155-1162.

Deardorff, J.W., 1972: Parameterization of the planetary boundary layer for use in general circulation models. *Mon. Wea. Rev.*, **100,** 93-106.

Frankignoul, C., 1985: Sea surface temperature anomalies, planetary waves, and air-sea feedback in the middle latitudes. *Rev. Geophys.*, **23,** 357-390.

Geisler, J.E., M.L. Blackmon, G.T. Bates and S. Munoz, 1985: Sensitivity of January climate response to the magnitude and position of equatorial sea surface temperature anomalies. *J. Atmos. Sci.*, **42,** 1037-1049.

Gill, A.E., 1980: Some simple solution for heat-induced tropical circulation. *Quart. J. R. Met. Soc.*, **106,** 447-462.

Grose, W.L. and B.J. Hoskins, 1979: On the influence of orography on large-scale atmospheric flow. *J. Atmos. Sci.*, **36,** 223-234.

Heckley, W.A. and A.E. Gill, 1984: Some simple analytical solutions to the problem of forced equatorial long waves. *Quart. J. R. Met. Soc.*., **110,** 203-217.

Held, I.M. and I.-S. Kang, 1987: Barotropic models of the extratropical response to El Niño. *J. Atmos. Sci.*, **44,** 3576-3586.

Hendon, H.H., 1986: The time-mean flow and variability in a nonlinear model of the atmosphere with tropical diabatic forcing. *J. Atmos. Sci.*, **43,** 72-88.

Horel, J.D. and J.M. Wallace, 1981: Planetary-scale atmospheric phenomena associated with the Southern Oscillation. *Mon. Wea. Rev.*, **109,** 813-829.

Iwasaka, N., K. Hanawa and Y. Toba, 1987: Analysis of SST anomalies in the North Pacific and their relation to 500 mb height anomalies over the Northern Hemisphere. *J. Meteor. Soc. Japan*, **65,** 103-114.

Japan Meteorological Agency, 1980: *Climatological Observations for 1971-1975.* Technical Data Series, No. 44, 73 pp.

————, 1981: *Climatological Observations for 1967-1970.* Technical Data Series, No. 45, 74 pp.

————, 1984: *Climatological Observations for 1976-1980.* Technical Data Series, No. 48, 74 pp.

————, 1987: *Climatological Observations for 1981-1985.* Technical Data Series, No. 52, 76 pp.

Julian, P.R. and R.M. Chervin, 1978: A study of the Southern Oscillation and Walker circulation phenomenon. *Mon. Wea. Rev.*, **106,** 1433-1451.

Kang, I.-S. and N.-C. Lau, 1986: Principal modes of atmospheric variability in model atmospheres with and without anomalous sea surface temperature forcing in the tropical Pacific. *J. Atmos. Sci.*, **43,** 2719-2735.

Katayama, A., 1972: *A simplified scheme for computing radiative transfer in the troposphere.* Tech. Report No. 6, Department of Meteorological, University of California, Los Angeles, CA, 77 pp.

————, 1978: Parameterization of planetary boundary layer in atmospheric general circulation models. Kisyo Kenkyu Note, Meteor. Soc. Japan, No. 134, 153-200. (in Japanese)

Kawamura, R., 1984: Relation between atmospheric circulation and dominant sea surface temperature anomaly pattern in the North Pacific during the northern winter. *J. Meteor. Soc. Japan*, **62,** 910-916.

————, 1986: Seasonal dependency of atmosphere-ocean interaction over the North Pacific. *J. Meteor. Soc. Japan*, **64,** 363-371.

Keshavamurty, R.N., 1982: Reponse of the atmosphere to sea surface temperature anomalies over the equatorial Pacific and the teleconnections of the Southern Oscillation. *J. Atmos. Sci.*, **39,** 1241-1259.

Lau, K.M. and H. Lim, 1982: Thermally driven motions in an equatorial β-plane: Hadley and Walker circulation during the winter monsoon. *Mon. Wea. Rev.*, **110,** 336-353.

———— and P.H. Chan, 1983a: Short-term climate variability and atmospheric teleconnection as inferred from satellite-derived outgoing longwave radiation. I: Simultaneous relationships. *J. Atmos. Sci.*, **40,** 2735-2750.

———— and ————, 1983b: Short-term climate variability and atmospheric teleconnection as inferred from satellite-derived outgoing longwave radiation. II: Lagged correlation. *J. Atmos. Sci.*, **40,** 2751-2767.

———— and J.S. Boyle, 1987: Tropical and extratropical forcing of the large-scale circulation: A diagnostic study. *Mon. Wea. Rev.*, **115,** 400-428.

Lim, H. and C.-P. Chang, 1983: Dynamics of teleconnections and Walker circulations forced by equatorial heating. *J. Atmos. Sci.*, **40,** 1897-1915.

Matsuno, T., 1966: Quasi-geostrophic motions in the equatorial area. *J. Meteor. Soc. Japan*, **44,** 25-43.

Mechoso, C.R., A. Kitoh, S. Moorthi and A. Arakawa, 1987: Numerical simulations of the atmospheric response to a sea surface temperature anomaly over the equatorial eastern Pacific Ocean. *Mon. Wea. Rev.*, **115,** 2936-2956.

Nihoul, L.C.J., 1985: *Coupled Ocean-Atmosphere Models.* Elsevier Science Publishers, Amsterdam.

Rasmusson, E. and T. Carpenter, 1982: Variations in tropical sea surface temperature and surface wind fields associated with the Southern Oscillation/El Niño. *Mon. Wea. Rev.*, **110,** 354-384.

Robock, A., 1982: The Russian surface temperature dataset. *J. Appl. Meteorol.*, **21,** 1781-1785.

Ropelewski, C.F. and M.S. Halpert, 1987: Global and regional scale precipitation patterns associated with the El Niño/Southern Oscillation. *Mon. Wea. Rev.*, **115,** 1606-1626.

Rowntree, P.R., 1972: The influence of tropical east Pacific Ocean temperature on the atmosphere. *Quart. J. R. Met. Soc.*, **98,** 290-321.

Schutz, C. and W.L. Gates, 1971: *Global climatic data for surface, 800 mb, 400 mb: January.* Advanced Research Projects Agency, Rep. R-915-ARPA, Rand Corporation, Santa Monica, 73 pp.

Shukla, J. and J.M. Wallace, 1983: Numerical simulation of the atmospheric response to equatorial Pacific sea surface temperature anomalies. *J. Atmos. Sci.*, **40,** 1613-1630.

Simmons, A.J., J.M. Wallace and G.W. Branstator, 1983: Barotropic wave propagation and instability, and atmospheric teleconnection pattern. *J. Atmos. Sci.*, **40,** 1363-1392.

Tokioka, T., K. Yamazaki, I. Yagai and A. Kitoh, 1984: *A description of the Meteorological Research Institute atmospheric general circulation model (MRI·GCM-I).* Technical Report of the Meteorological Research Institute, No. 13, MRI, Tsukuba, 249 pp.

————, A. Kitoh, I. Yagai and K. Yamazaki, 1985: A simulation of the tropospheric general circulation with the MRI atmospheric general circulation model. Part I: The January performance. *J. Meteor. Soc. Japan*, **63,** 749-778.

————, ———— and A. Katayama, 1986a: Atmospheric response to the sea surface temperature anomalies in the mature phase of El Niño: Numerical experiment under the perpetual January condition. *J. Meteor. Soc. Japan*, **64,** 347-362.

————, K. Yamazaki and A. Kitoh, 1986b: *Mean statistics of the tropospheric MRI·GCM-I based on 12-year integration.* Technical Report of the Meteorological Research Institute, No. 20, MRI, Tsukuba, 314 pp.

———— and A. Noda, 1986: Effects of large-scale orography on January atmospheric circulation: A numerical experiment. *J. Meteor. Soc. Japan*, **64,** 819-840.

van Loon, H. and J.C. Rogers, 1981: The Southern Oscillation. Part II: Associations with changes in the middle troposphere in the northern winter. *Mon. Wea. Rev.*, **109,** 1163-1168.

Wallace, J.M. and D.S. Gutzler, 1981: Teleconnections in the geopotential height field during the Northern Hemisphere winter. *Mon. Wea. Rev.*, **109,** 784-812.

WCP, 1986: *Comparison of Simulations by Numerical Models of the Sensitivity of the Atmospheric Circulation to Sea Surface Temperature Anomalies.* NCAR, Boulder, Colo., December 1985. WMO/TD-No. 138, WCP-121, 188 pp.

Weare, B.C., 1986: Extension of an El Niño index. *Mon. Wea. Rev.*, **114,** 644-647.

海面水温と日本の暖冬に関する数値実験

鬼頭昭雄

（気象研究所気候研究部）

日本の暖冬・寒冬に重点を置いて，海面水温偏差の大気に対するインパクトを調べた。5層MRI·GCM−Iを用いて，perpetual January modeで一連の180日間積分を9例行ない，30日平均降水量，500 mb高度，地表気温の主成分分析を行なった。

低緯度の降水量変動パターンは東西に細長い構造をしており，その正負偏差分布はコントロール・ランの海面水温並びに降水量分布に依存している。東アジアの地表気温は，日本から中国にかけての領域とオホーツク海との対照が特徴であり，これは北太平洋の高気圧偏差とシベリアからのコールド・サージの弱まりに対応している。この循環は500 mb高度の第1主成分に現われ，かつ日本の暖冬時の合成海面水温（1972,73,79,83）を用いたランで卓越している。この時の環太平洋領域の循環場のアノマリーは観測と対応している。

この中緯度循環パターンはハワイの南方の降水量偏差と高相関があり，これは赤道上，日付変更線付近に海面水温偏差を与えた追加実験により確認される。これらの循環は低緯度熱源に対する直接の応答ではない。日本暖冬パターンは大気に固有のモードであることが示され，海面水温偏差によりこのパターンの出現頻度が高くなったと示唆される。線形モデルの範囲では，このパターンは亜熱帯の発散場に対する力学的応答として理解される。従って低緯度の海面水温偏差並びに熱源の日本暖冬パターンへの影響は直接的なものではなく，亜熱帯循環の変動を通じて実現される間接的なものである。

Correlation between the Surface Air Temperature over Japan and the Global Sea Surface Temperature

By Akio Kitoh

Reprinted from the Journal of the Meteorological Society of Japan
Vol. 66, No. 6, December 28, 1988

Correlation between the Surface Air Temperature over Japan and the Global Sea Surface Temperature

By Akio Kitoh

Meteorological Research Institute, Tsukuba, Ibaraki 305, Japan
(Manuscript received 7 July 1988, in revised form 11 October 1988)

Abstract

Relationships between the global sea surface temperature (SST) and the surface air temperature over Japan (TsJ) are examined by computing lagged cross-correlations based on the monthly mean data for 1970-1984. High correlation is found between the TsJ for December and the preceding SST over the central equatorial Pacific around 0°N, 160°W. Since the SST anomaly in this area persists for a long period, this relationship holds significant back to the summer (the SST leading the TsJ by half a year). For the TsJ in January or February, there is no significant relationship with the SST in the tropics. Therefore this relationship cannot be obtained by using three-month mean data. There is a high correlation between the TsJ for January or February and the SST over the North Pacific around 40°N, 150°W for a 0 to 2 months' lag with a lead in the SST. The corresponding circulation anomaly for December differs from that for January or February, although both are associated with an anomalous southerly wind and warm air advection near Japan. It is also found that the TsJ and the associated circulation pattern for March are highly correlated with the *following* El Niño event. During summer there is a high correlation between the SST over the western Pacific and the TsJ for July.

1. Introduction

Interactions between the atmosphere and the surface, including the ocean, are among the most important processes which affect the atmospheric general circulation. Among them, much attention has been given to the sea surface temperature (SST).

The SST may be useful for seasonal forecasts, since the SST anomalies have a much longer persistence than the atmospheric anomalies. Namias (*e.g.*, 1959, 1963, 1968, 1969) and Bjerknes (1966, 1969) noted and investigated the role of the air-sea interactions in the middle latitudes and in the tropics, respectively. Namias (1969, 1978) examined the relationship between the SST over the North Pacific and climate in North America, whereas Namias (1967) and Ratcliffe and Murray (1970) investigated the North Atlantic SST anomalies near Newfoundland for application to long-range weather forecasting. A review of the studies of the SST and atmospheric circulations in the middle latitudes can be found in Frankignoul (1985).

Bjerknes (1966, 1969) studied teleconnections between equatorial SST anomalies and atmospheric circulation anomalies not only in the tropics but also in the extratropics of the Northern Hemisphere. Starting with Rowntree (1972), many general circulation model (GCM) studies have shown a high sensitivity of the atmosphere to tropical SST anomalies. Followed by the increased attention paid to the El Niño/Southern Oscillation (ENSO) phenomenon, teleconnections between tropical and extratropical latitudes have intensively been studied.

Many statistical studies have been accumulated in connection with monthly to seasonal climate forecasting in Japan (*e.g.*, Wada, 1969; JMA, 1981). Asakura (1980), using the 137°E oceanographic section data, found that the SST

at 6°N, 137°E during January is highly correlated with the annual frequency of typhoon formation for the coming year. He also showed that when the SST difference between 6°N and 24°N at 137°E is large, the rainy season (Baiu) in Tokyo ends late, and conversely when the difference is small the Baiu ends early. Kurihara (1984) also showed the relationship between the sea water temperature at a depth of 20 m at 3-6°N, 137°E during January or July and the date of the end of the Baiu season in Tokyo. The duration of the Baiu season or the date of its end mainly governs the monthly mean temperature for July. Thus, there is a high correlation between the temperature in central Japan during July and August, and water temperature in the western tropical Pacific (Kurihara, 1985). Kurihara and Kawahara (1986) and Nitta (1987) suggest the possible role of the higher SST in the western tropical Pacific in intensifying active convection during summer, which in turn influences the weather in East Asia. The relationship between the equatorial Pacific SST along with the North Pacific SST and the frequency of typhoon formation and typhoon landfall in Japan has been extensively examined by Aoki (1985).

In regard to the winter climate in Japan with respect to the global SST, there are fewer studies. Yamada (1986, personal communication) showed by simultaneous correlation analysis, using the three-month mean (December through February) data for 1970-1984, that the temperature in central Japan not only had a high temporal correlation with warm SST anomalies over the equatorial central Pacific, but also with warm SST anomalies near Japan, over the South China Sea and the Indian Ocean. Studies of SST anomalies in the North Pacific and their relation to atmospheric circulations include Kawamura (1984, 1986) and Iwasaka *et al.* (1987). Kurihara (1988), using three-month mean fields, showed that 500 mb height anomalies are significantly positive over the subtropical Pacific south of Japan and are negative over the Aleutians. The winter climate in Japan tends to be mild during El Niño years, but there have been exceptions, such as the 1976/77 winter.

Kitoh (1988) performed a GCM experiment to study the impact of SST anomalies on the resulting atmospheric circulation with emphasis on the winter climate in Japan. His results produced a northern mid-latitude circulation pattern which was closely related to the winter temperature in Japan and showed a possible role of the equatorial SST anomaly east of the dateline in inducing such a circulation pattern. This paper uses the global SST data over a 15-year period to study the relationship between the monthly mean SST and the monthly mean temperature in Japan to form an index for atmospheric circulation, with emphasis on winter.

2. Data

The SST data used in this study was provided by the U.S.NOAA. The monthly mean SST data extends from 40°S to 60°N on a 2° by 2° latitude-longitude grid for 1970-1984. The 2° by 2° grid data are interpolated to a 4° latitude by 5° longitude grid, in order to match the resolution employed by the GCM of the Meteorological Research Institute (MRI). The monthly SST anomaly (SSTA) fields were computed for each grid point as departures from the 15-year mean.

The monthly surface air temperature over Japan (TsJ) is given in this study by the arithmetic mean of those at Nemuro, Kanazawa, Tokyo, Miyazaki and Ishigakijima. These five stations are part of the climatological dataset of the Japan Meteorological Agency (JMA). Data over the period 1969-1985 are used to calculate the lag-correlations between the TsJ anomaly (TsJA) and the SSTA using a lag of ±12 months. Also, geopotential heights at 500 mb (Z500) and sea level pressure (SLP) over the Northern Hemisphere on a 10° by 10° grid spanning the same period are provided by the Long-Range Forecasting Division of JMA. The El Niño index (ENI) proposed by Weare (1986) and the Southern Oscillation index (SOI) are also used for comparison.

3. Lag-correlations between the TsJA in winter and the SSTA

a. Global distribution

Figures 1, 2 and 3 show the distribution of the correlation coefficient r between the TsJA for December, January and February, respectively,

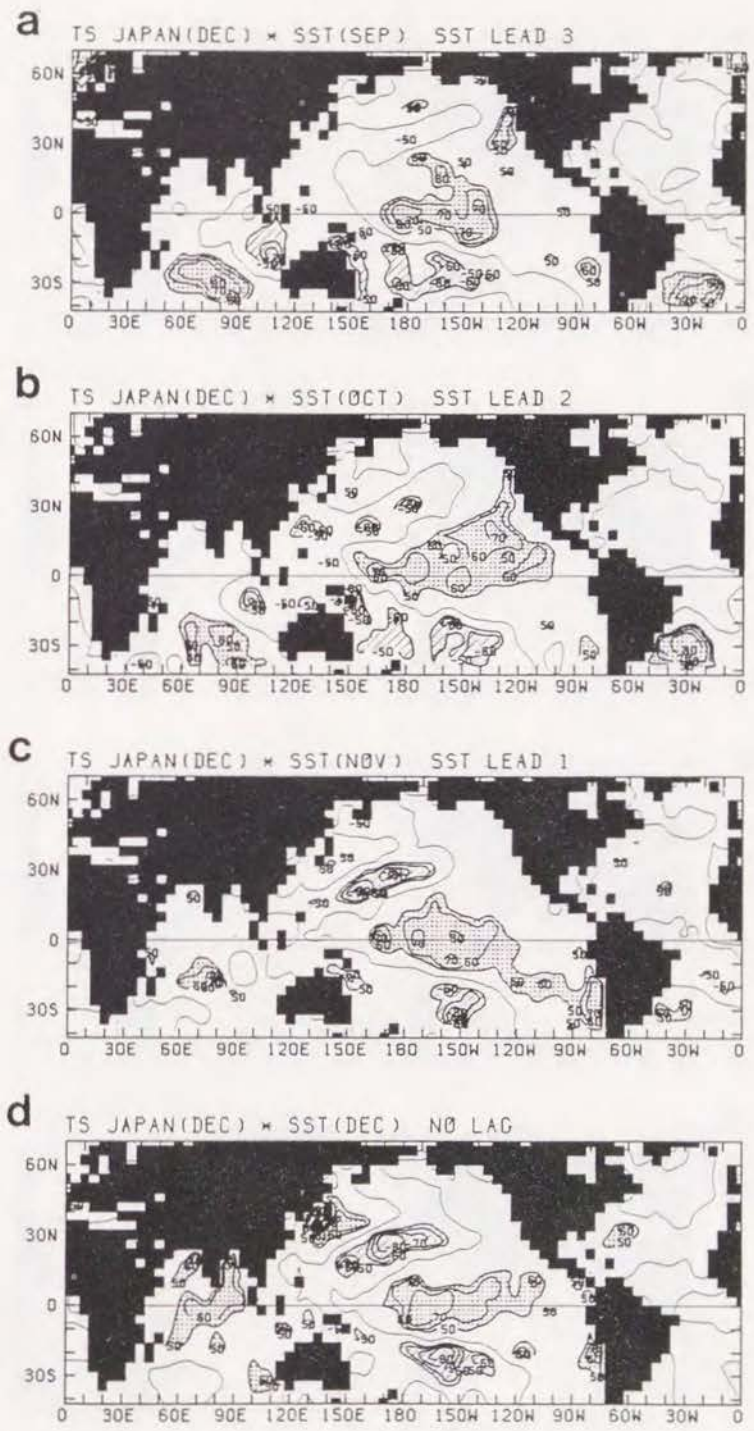

Fig. 1 Distributions of the correlation coefficients between the surface air temperature anomaly in Japan for December and the SST anomalies in (a) September, (b) October, (c) November and (d) December, respectively. Values greater than 50% (stippled) or less than −50% (hatched) are shown with a contour interval of 10%. A thin line denotes 0%.

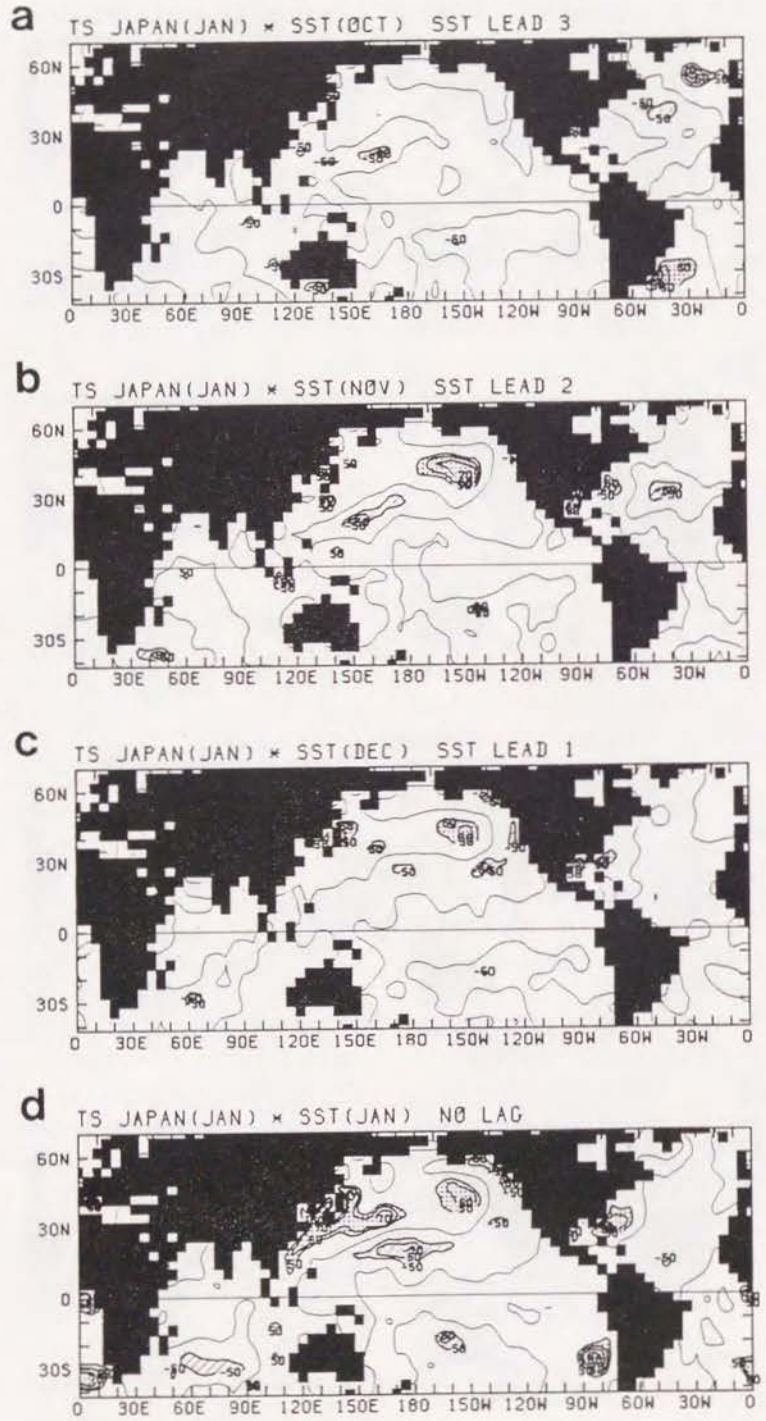

Fig. 2 As in Fig. 1 except for the surface air temperature anomaly for January and the SST anomalies in (a) October, (b) November, (c) December and (d) January.

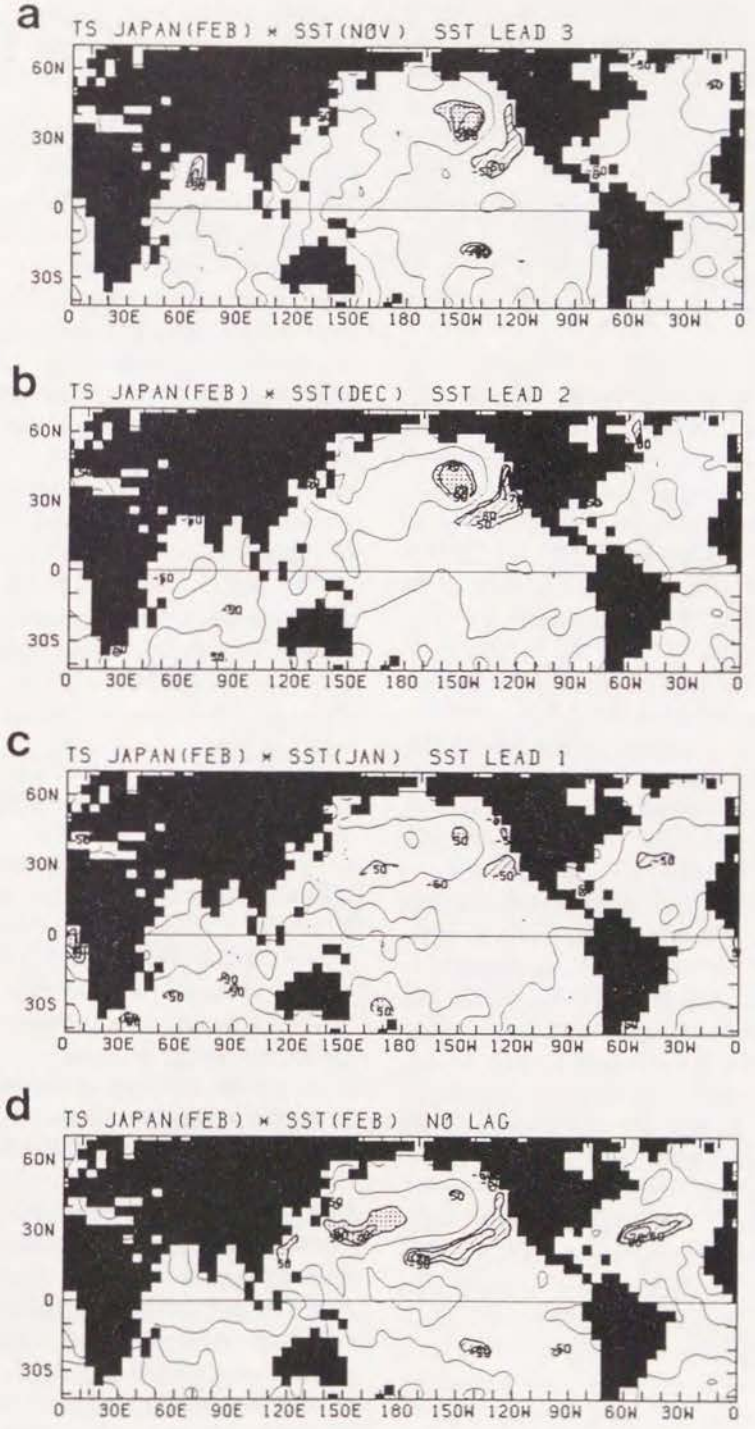

Fig. 3 As in Fig. 1 except for the surface air temperature anomaly for February and the SST anomalies in (a) November, (b) December, (c) January and (d) February.

and the global SSTA using a lag of −3 to 0 months (*i.e.*, the SSTA leading the TsJA by 3 to 0 months). If the SSTA and TsJA are normally distributed, the statistical significance of r can be assessed as follows (Panofsky and Brier, 1958): if $|r\,(n-2)^{1/2}| \geq 1.6$, 2.0 or 2.6, then r is significant at the 10, 5 or 1% level, respectively, where n is the number of independent values. When $n = 15$, values of $|r| \geq 0.44$, 0.55 or 0.72 are significant at the 10, 5 or 1% level, respectively.

The simultaneous (lag = 0) correlation map for December (Fig. 1d) shows regions with significantly large correlation coefficients; positive correlations over the central equatorial Pacific, equatorial Indian Ocean and near Japan, with negative values over the central subtropical Pacific in both hemispheres. The shape of this pattern is similar to the composited SSTA in the mature phase of El Niño (Rasmusson and Carpenter, 1982), although it is the central equatorial Pacific rather than the eastern Pacific that is significantly correlated with the TsJA.

Lag-correlation maps show that the SSTA over the central equatorial Pacific has a persistently high correlation with the TsJA with leads in the SSTA of a few months. For example, the SSTA for September over the equator, between 170°E and 130°W, is highly correlated three months later with the TsJA. This is useful information to the statistical long-range forecasting in Japan and is more thoroughly discussed later. Another region with high correlation can be found over the Indian Ocean, although the region having the maximum correlation coefficient changes with lag from the South Indian Ocean for September to the equatorial Indian Ocean for December.

Figure 2 shows the lag-correlation maps between the TsJA of January and the SSTA. The overall pattern of signs in the simultaneous correlation for January (Fig. 2d) has some resemblance to that for December (Fig. 1d), with regard to positive correlations near Japan and negative correlations over the subtropical Pacific. However, it is considerably different over the equatorial Pacific, where the correlation is insignificant. Another notable difference can be found over the central North Pacific, where high positive correlations appear around 40°N, 150°W, showing persistently high correlations when there is a lead in the SSTA of 1 to 2 months.

Figure 3 shows the distributions of lag-correlation coefficients for the TsJA in February. The maximum positive simultaneous correlation east of Japan and negative correlations over the subtropical Pacific are located to the east of those in January. As with those found in January there exists high correlation between the TsJA and the SSTA around 40°N, 150°W, when the SSTA leads the TsJA by a few months.

Lag-correlations between the TsJA and the SSTA in three regions are more thoroughly examined in the following subsections. The selected regions are for areas of 8° latitude by 10° longitude, centered at (0°N, 160°W), (40°N, 150°W) and (30°N, 150°E). The first region was chosen for the high correlation in December (Fig. 1). The second area shows high correlation in both January and February (Figs. 2 and 3). The third region is a representative of the neighboring waters of Japan.

b. The SSTA in the central equatorial Pacific and the TsJA

Figure 4a shows the lag-correlation coefficients between the TsJA and the SSTA at 0°N, 160°W. The ordinate shows the month of the SSTA, the abscissa represents the number of months of lag of the TsJA relative to the SSTA while the slanted lines correspond to months of the TsJA.

As has already been shown in Figs. 1d and 1a, there was a high correlation of $r = 0.77$ for the SSTA in December with a lag = 0 and $r = 0.74$ for the SSTA in September with lag = 3 (the TsJA lags the SSTA by three months). This high correlation, diagonally distributed in this figure, is strong back to July (Jag = 5) with $r = 0.70$ and June (lag = 6) with $r = 0.55$, both of which are significant at the 5% level. The high correlation persists until March (lag = −3, $r = 0.58$). This relationship holds good only for the TsJA in December, as shown by small correlation coefficients in the central equatorial Pacific for January and February (Figs. 2 and 3).

Next, the circulation anomalies associated

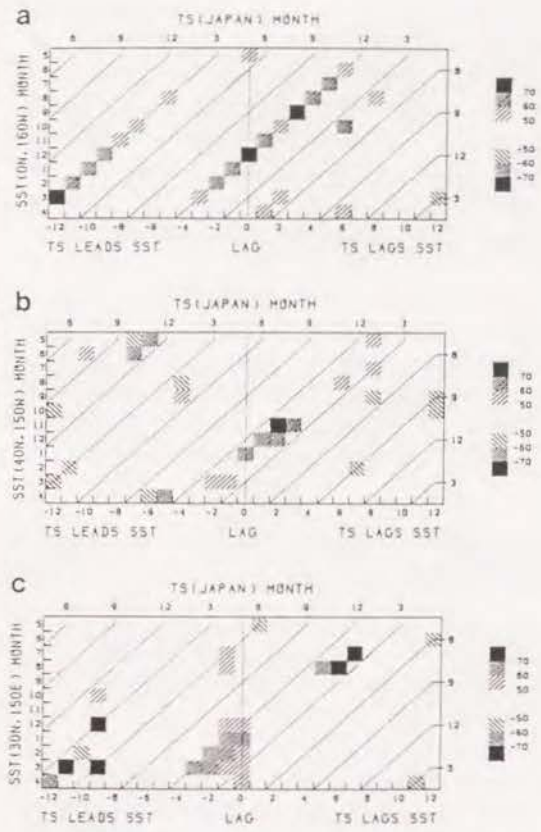

Fig. 4 Lag-correlations between the surface air temperature anomaly over Japan and the SST anomaly at (a) 0°N, 160°W, (b) 40°N, 150°W and (c) 30°N, 150°E. Values greater than 50% or less than −50% are shown.

with a warm/cold Japan are shown with the use of correlation maps between the SSTA and the Z500 or SLP anomalies. Figure 5 shows the distributions of the correlation coefficients between the SSTA of July at 0°N, 160°W and the Z500 (Fig. 5a) and SLP anomalies (Fig. 5b) for December. The month of July was chosen as representative with a high correlation. The main characteristics of the circulation anomalies for the SSTA in September or December are similar to those shown in Fig. 5. High pressure anomaly at 500 mb occurs over Japan (Fig. 5a) while low pressure anomalies appear over Siberia and north of Hawaii during December when the SST at 0°N, 160°W for July is warm. This teleconnection pattern can be found from the North Atlantic through northern Europe and Siberia to Japan. It is recognized as the Eurasian (EU) pattern obtained by Wallace and Gutzler (1981) and Gambo and Kudo (1983).

The correlation pattern for the SLP (Fig. 5b) shows general agreement in its sign with that for the Z500 over the extratropics. However, they differ in the position of maximum correlation. A notable feature in the SLP field is the weakened anticyclone in Siberia and China when the SST at 0°N, 160°W is warm. The anomalous surface wind is southerly over East Asia, leading to a warmer than normal surface air temperature in Japan. Over the North Atlantic, the low pressure around 50°-60°N contrasts with the high pressure around 20°N. The North Atlantic Oscillation (NAO) is the dominant teleconnection pattern in the North Atlantic (van Loon and Rogers, 1978), which is associated with a pressure difference between the Azores (40°N) and Iceland (65°N). The pattern in Fig. 5b is shifted southward relative to the NAO. This is closer to the Eastern Atlantic (EA) pattern found by Barnston and Livezey (1987), who applied the rotated principal component analysis to Northern Hemisphere monthly mean 700 mb heights.

The fact that there are high correlations in a straight line for several months ($r > 0.5$ for 10 months in this case) implies two things; a high persistence of the SSTA and a strong sensitivity in the relationship between the SSTA around 0°N, 160°W and the TsJA of December.

To show the persistence of the SSTA this region, an auto-correlation is calculated with a lag of ±12 months for every month (Fig. 6). The persistence of the SSTA differs from month to month, however, in this region it persists for a long period during the northern summer. The auto-correlation coefficient for June with a lag of 6 months is 0.85. The coefficient in August is 0.94 with a lag of 4 months and 0.82 with a lag of 7 months. However, the SSTAs in April and May do not persist very long. For example, the auto-correlation coefficient for May drops immediately to 0.67 after 2 months. Thus the SSTA in this region tends to change during the northern spring and that formed in summer tends to persist through autumn, lasting until late

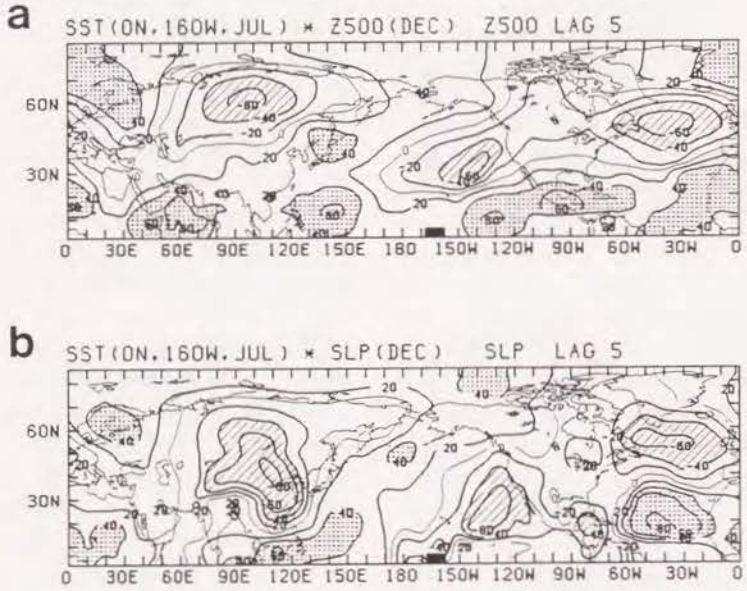

Fig. 5 (a) Distributions of the correlation coefficients between the SST anomaly at 0°N, 160°W for July and the geopotential height anomalies at 500 mb for December. The contour interval is 20%. Values greater than 40% are stippled and those less than −40% are hatched. (b) as in (a) except for the sea level pressure.

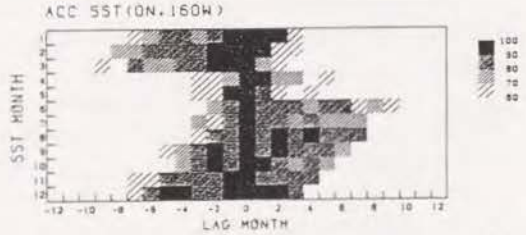

Fig. 6 Auto-correlations of the SST anomaly at 0°N, 160°W. Values greater than 60% are shown.

winter. Composited SST anomalies for six El Niño events by Rasmusson and Carpenter (1982) along ship track 6 (their Fig. 9), which crosses the equator at 170°W, show greater than 0.5°C positive SST anomalies from June through the next March, a period of 10 months. Thus the characteristics of persistence in the SSTA reflect a life cycle of a typical composited El Niño.

The persistence of the SSTA also differs from region to region. Figure 7 shows the distribution of the number of months in which the auto-correlation coefficient of the SSTA is successively greater than 0.70 from August. This figure reveals two regions of high persistence where the auto-correlation coefficient in summer lasts almost half a year until the next winter. One is the region around 0°N, 160°W, and the other is located around 120°W, south of the equator. The most prominent mechanism responsible for forming the relatively cold water in the central equatorial Pacific is considered to be the upwelling due to surface easterlies. Therefore, the structure of the seasonal variation of atmospheric circulation must play an important role in forming and maintaining the SSTA in this region. For the atmospheric part, an auto-correlation

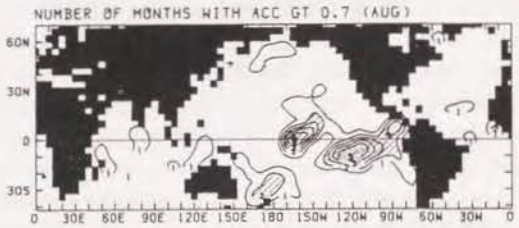

Fig. 7 Number of successive months with the auto-correlation coefficient greater than 0.70 for the SST anomaly in August. The contour interval is 1 month. Values greater than 2 are lightly hatched and those greater than 4 are heavily hatched.

pattern similar to Fig. 6 but of less magnitude has been obtained for the SLP at Darwin (Trenberth and Shea, 1987). Since the ENSO greatly affects atmospheric as well as oceanic circulations, not only in the tropics but also in the extratropics, the study of the regional and seasonal difference in the persistence of the SSTA is an interesting and important problem to be solved.

The second point to be mentioned with respect to Fig. 4a is that the high correlations are not broadly distributed but fall in a straight line. The SSTA for December is highly correlated with the TsJA for December ($r = 0.77$), but less than that for November ($r = 0.47$) or that for January ($r = 0.44$). This indicates that although the SSTA around 0°N, 160°W persists from June until March of the next year, it is in December and not in November nor in January that the TsJA highly correlates with that SSTA. The present result implies that the circulation anomalies, which cause the positive TsJA and are related to the positive SSTA at 0°N, 160°W (and conversely those which cause the negative TsJA and are related to the negative SSTA), tend to appear mainly in December.

This high sensitivity in the relationship is clearly seen in Fig. 8, which shows simultaneous correlation maps between the SSTA at 0°N, 160°W and the Z500 anomalies for December,

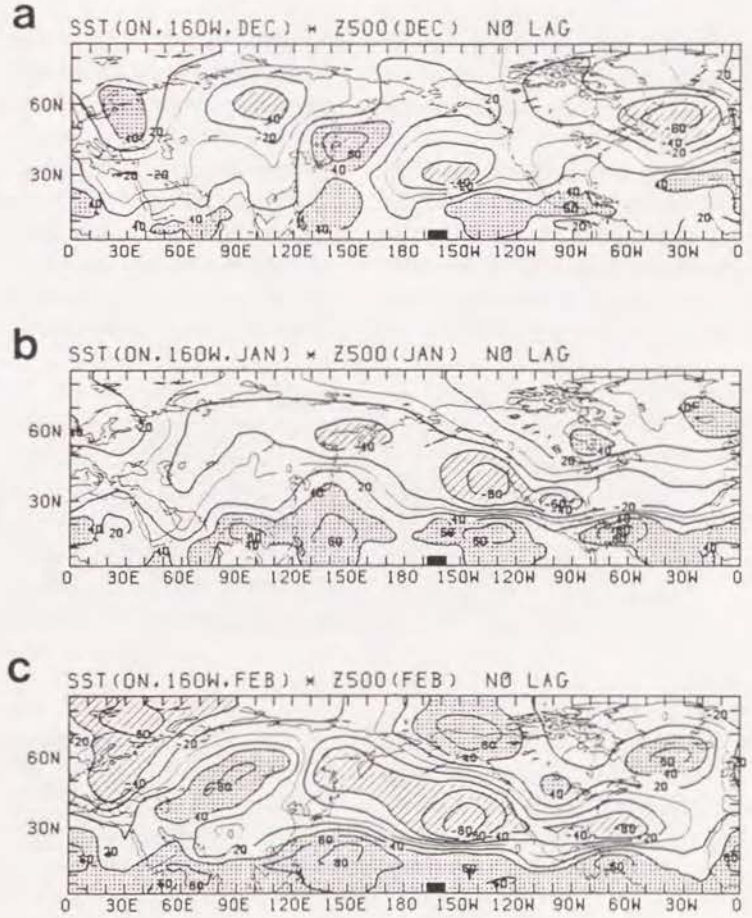

Fig 8 (a) Distributions of the simultaneous correlation coefficients between the SST anomaly at 0°N, 160°W and the geopotential height anomalies at 500 mb for December. The contour interval is 20%. Values greater than 40% are stippled and those less than -40% are hatched. (b) as in (a) except for January. (c) as in (a) except for February.

January and February. The difference between the map for December and those for January and February is striking. In December, the pattern is almost identical to that of Fig. 5a due to the SSTA at 0°N, 160°W being very persistent from July to December. In January and February, the SSTA at 0°N, 160°W highly correlates with positive Z500 anomalies south of Japan and negative Z500 anomalies over the Sea of Okhotsk. If three-month mean (December to February) SST and Z500 data are used, the resultant correlation map (not shown, but similar to Fig. 2 of Kurihara, 1988) captures characteristics of January and February, but not those of December. As already shown in Figs. 2, 3 and 4a, there are no significant correlations between the TsJA and the SSTA over the equatorial Pacific for January or February, although the surface air temperature anomalies far south of Japan become positive in relation to the SSTA over the central equatorial Pacific.

Figure 4a also shows high correlations where the TsJA leads the SSTA. The TsJA for March is highly correlated with the SSTA from October until March (the SSTA lags the TsJA by 7 months to one year). This relationship appears strongest over the tropical eastern Pacific, and will be discussed in Section 5.

c. The SSTA in the central North Pacific and the TsJA

Figure 4b shows the lag-correlations between the TsJA and the SSTA at 40°N, 150°W. The SSTA for November in this region correlates well with the TsJA for January with $r = 0.76$ and with the TsJA for February with $r = 0.69$. Also, the SSTA for December correlates well with the TsJA for January, having $r = 0.62$, and with the TsJA for February with $r = 0.69$. This result implies that the warm SSTA over the central North Pacific, which persists from November to January, tends to precede the atmospheric variations leading to warm January and February in Japan.

The anomaly distributions for the Z500 and SLP in January when the SST at 40°N, 150°W in November is warm are shown in Figs. 9a and 9b. Once again the EU pattern appears, but the anomalous circulations over the Pacific and the North American sector are quite different from those found in Fig. 5. In this case, the anomalous anticyclone at 500 mb extends zonally at 40°N, with its center over Japan. A low pressure area extends from Siberia toward the Caspian Sea and

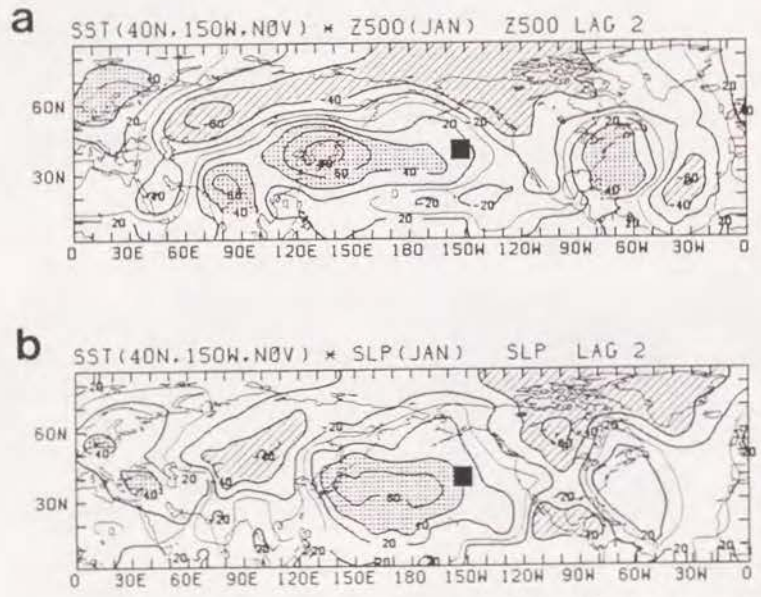

Fig. 9 As in Fig. 5 except for the SST anomaly at 40°N, 150°W for November and the circulation anomalies of January.

another trough appears over the west coast of North America. It should be noted that the Pacific/North American (PNA) pattern (Wallace and Gutzler, 1981) is easily recognized in this map.

The SLP field is characterized more by a strong anomalous anticyclone over the subtropical Pacific than the weak Siberian high. Thus, the circulation changes, both in December and January, are associated with the anomalous southerly wind and warm air advection near Japan. However, the details are different: the Siberian high is weaker than normal in December, while the Pacific subtropical anticyclone belt is stronger in January with a weaker than normal Siberian high.

Davies (1976) and Lanzante (1984) show evidence of the atmosphere driving the ocean circulation in the North Pacific. Iwasaka *et al.* (1987) also shows that the dominant SST anomaly pattern in the North Pacific is caused by the atmospheric fluctuation corresponding to the PNA pattern, but that the SST anomaly in the North Pacific is not always connected with El Niño events. On the other hand, the present analysis shows an example of the ocean leading the atmosphere in the middle latitudes. There are studies concerning transitions between circulation regimes during the Northern Hemisphere winter, including the PNA and EU patterns (Kimoto, 1987; Kanaya, 1988). The present result suggests a possible linkage between the PNA and EU patterns accompanied by a change in the SST in the North Pacific. Whether the role of the SSTA in the North Pacific is active or passive remains unclear in the present study, but should be examined more extensively in the future.

b. The SSTA near Japan and the TsJA

Kawamura (1984, 1986) shows by lag-correlation analyses that the SSTA near Japan lags one month behind and is highly correlated with the mid-latitude circulation in winter, claiming that a warm SSTA off Japan is a result of a weaker than normal cold surge and conversely a cold SSTA results from a stronger than normal cold surge. Figure 4c shows the lag-correlations between the TsJA and the SSTA at 30°N, 150°E. High correlations in winter are distributed where the TsJA leads the SSTA with the maximum ($r = 0.69$) between the TsJA for January and the SSTA for February, confirming the results by Kawamura (1984, 1986). The anomaly distributions for the Z500 and SLP in January when the SST at 30°N, 150°E during February is warm (not shown) are quite similar to Fig. 5 of Kawamura (1984). It should be noted that there are other high correlations between the SSTA during July or August and the TsJA for February of the following year (lag = 7 or 6 months, $r = 0.80$ or 0.75). Also, high correlations occur between the SSTA for March and the TsJA for April of the previous year (lag = −11 months, $r = -0.80$).

4. Relationship with the ENSO

It has been shown that there are good relationships between the SSTA for June through March at 0°N, 160°W and the TsJA for December, and also between the SSTA for November through January at 40°N, 150°W and the TsJA for January and February. In this section the year-to-year variations of these indices together with two of the ENSO (meteorological and oceanographic indices) are examined. The ENI proposed by Weare (1986) uses coefficients of the first eigenvector of the SSTA in the Pacific and was calculated until December 1983. The SOI is defined as the sea level pressure difference between Tahiti and Darwin (Parker, 1983).

Figure 10 shows the simultaneous (lag = 0) correlation coefficients of the ENI (Fig. 10a) and SOI (Fig. 10b) correlated with the global SST for all months during 1970-1984. Both have significant correlations over the central and eastern equatorial Pacific and the Indian Ocean. Another region having the opposite sign is found over the subtropical Pacific in both hemispheres and the North Pacific. A notable difference is in the position of the maximum correlation. The interannual variability of the SST is the largest over the eastern equatorial Pacific (Weare *et al.*, 1976; Hsiung and Newell, 1983) and the ENI is more correlated with the SSTA in the eastern equatorial Pacific as shown in the first eigenvector map of the Pacific SST by Weare (1986). On the other hand, the SOI is highly correlated with the

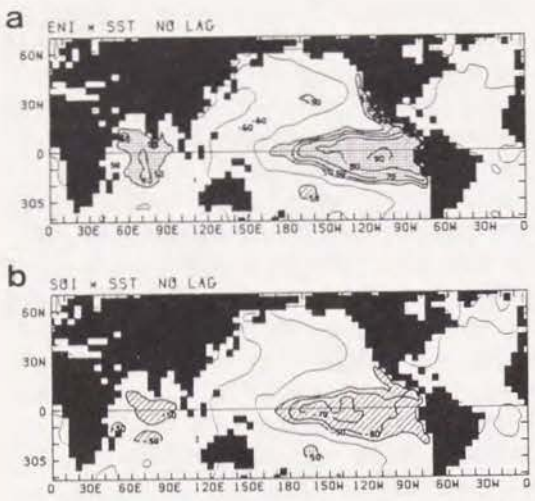

Fig. 10 (a) Distributions of the correlation coefficients between the ENI and the global SST for 180 months over 1970-1984. Values greater than 50% (stippled) or less than −50% (hatched) are shown with contour interval of 10%. A thin line denotes 0%. (b) As in (a) except for the SOI and SST.

SSTA at 0°, 160°W with $r = -0.74$. Over the eastern equatorial Pacific where the signal of the ENI is the largest, correlation coefficients are smaller than those over the central Pacific.

Figure 11 shows the TsJA for December (thick solid line) versus the SSTA at 0°N, 160°W during July (thick dashed line) for the years 1970-1984. Also, the ENI is represented by a thin dashed line and the SOI by circles. All indices are deviations from the 15-year mean (14-year for the ENI). In the two strong El Niño years of 1972 and 1982, both the SST for July and the TsJ of December are warm. In 1976, the ENI is large but the SSTA is also large off the west coast of South America; the SSTA at 0°N, 160°W for July is small and the TsJA for December is also small. In 1979, the ENI is very small but positive SSTAs are distributed in the broad region of the central equatorial Pacific; the SSTA at 0°N, 160°W for July is large and the TsJA for December is very large. The relationship between the SOI for July and the TsJA for December is good with $r = -0.52$, although it is less than that for the SSTA chosen ($r = 0.70$). On the other hand the relationship between the ENI and the TsJA is insignificant ($r = 0.16$). Thus the TsJA for December has a close link to the Southern Oscillation as well as to the SSTA over the central equatorial Pacific, but not to the ENI nor the SSTA over the eastern Equatorial Pacific.

Figure 12 shows the SSTA at 40°N, 150°W for November of the designated years (thick dashed line) and the TsJA for January of the following year (thick solid line), together with

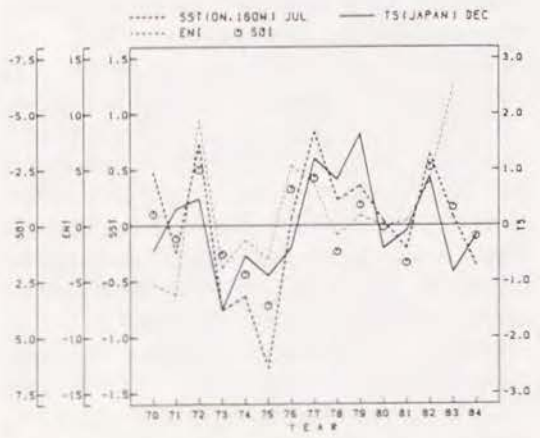

Fig. 11 Comparison with the SST anomaly at 0°N, 160°W for July (thick dashed line) and the surface air temperature anomaly over Japan for December (thick solid line). A thin dashed line and circles denote the ENI and the SOI, respectively in July.

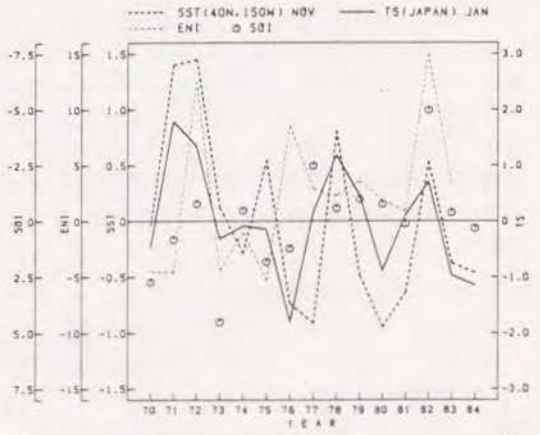

Fig. 12 Comparison with the SST anomaly at 40°N, 150°W for November in the designated years (thick dashed line) and the surface air temperature anomaly over Japan for the following January (thick solid line). A thin dashed line and circles denote the ENI and the SOI in November.

the ENI and the SOI in November. In this case the correspondence of the ENI and SOI versus the TsJA is very poor with $r = 0.07$ and −0.30, respectively. In November 1971, the ENI is negative while the SOI is positive when the SST at 40°N, 150°W is very warm. Two months later, the ENI and SOI hardly change, while the TsJ is very warm. In 1972, all four indices show positive values. In November 1976, the ENI is large, the SST at 40°N, 150°W is very cold and the TsJ two months later is very cold. In November 1980, the ENI and the SOI are small but the SST at 40°N, 150°W is very cold. Two months later, the ENI is still small while the TsJA is negative.

Figure 13 shows the TsJA for January (solid line) and the SSTA to the east of Japan during the next month (dashed line). The correlation is high ($r = 0.69$) as already shown in Fig. 3 and 4c. An almost perfect correlation can be seen in the most recent six winters. Neither the ENI nor SOI has a significant correlation with the TsJ.

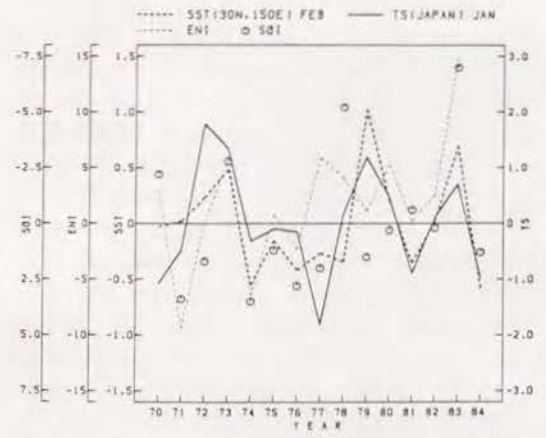

Fig. 13 Comparison with the SST anomaly at 30°N, 150°E for February (thick dashed line) and the surface air temperature anomaly over Japan for January (thick solid line). A thin dashed line and circles denote the ENI and the SOI in February.

5. Circulation anomalies preceding the ENSO

It was shown that the TsJA for March was highly correlated with the succeeding SSTA at 0°N, 160°W with a lead of 7 to 12 months (Fig. 4a). The correlation becomes higher if the SSTA over the eastern equatorial Pacific is used. Figure

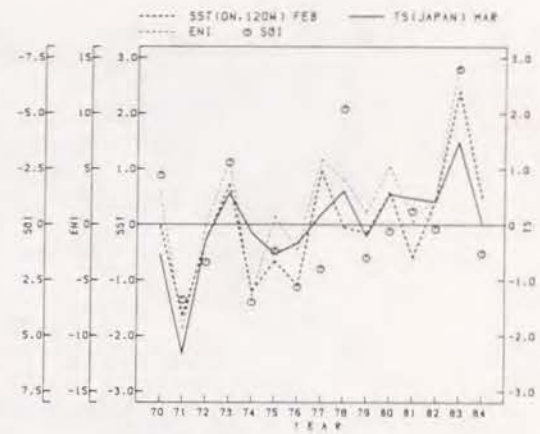

Fig. 14 Comparison with the SST anomaly at 0°N, 120°W for February in designated years (thick dashed line) and the surface air temperature anomaly over Japan in March during the preceding year (thick solid line). A thin dashed line and circles denote the ENI and the SOI in February.

14 shows the SSTA at 0°N, 120°W, the ENI and SOI for February of the designated years (thick and thin dashed lines and circles, respectively) and the TsJA for March of the *preceding* year (thick solid line). Correlation coefficients of the TsJA versus the SSTA, ENI and SOI are 0.78, 0.83 and −0.67, respectively. The interannual variability of the SST in this area is clearly manifested in the El Niño phenomenon. It is worth noting that there is a increasing linear trend in all the four indices, suggesting a close relationship among them. Correlation coefficients after the removal of the linear trend are 0.67, 0.74 and −0.67 for the SSTA, ENI and SOI, respectively. A lag-correlation map similar to Fig. 4a but for the SSTA at 0°N, 120°W (not shown) reveals persistently high correlation ($r > 0.50$) with the TsJA of March and the SSTA during May through March of the following year (TsJA leads SSTA by 2 to 12 months).

The corresponding circulation pattern for March is shown in Fig. 15. There are negative anomalies around Iceland and a wave train is evident in the Z500 field from Eurasia to the central tropical Pacific. Over the central tropical Pacific, negative sea level pressure anomaly appears south of Hawaii. The circulation pattern obtained in Fig. 15 may be one manifestation of

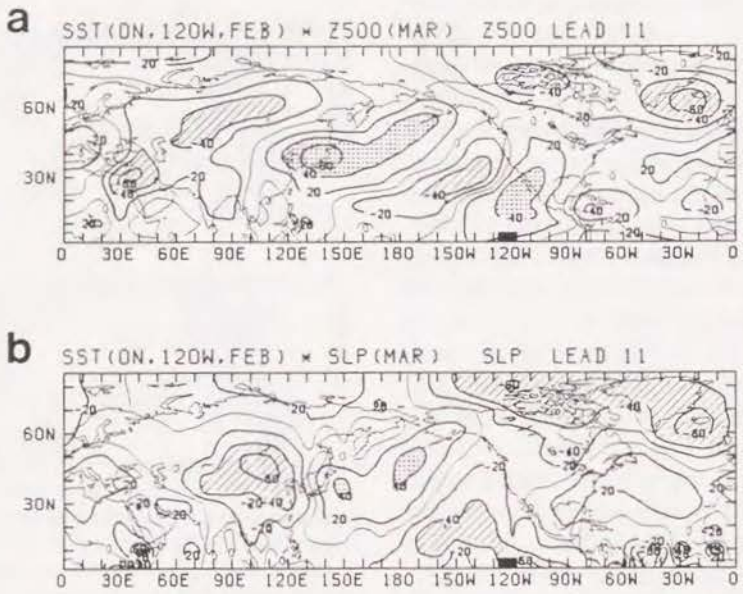

Fig. 15 As in Fig. 5 except for the SST anomaly at 0°N, 120°W for February and circulation anomalies for March of the preceding year.

the process of atmospheric circulation changes preceding El Niño or an ENSO cycle, including the process over Eurasia (Barnett, 1985).

6. Lag-correlations between the TsJA in summer and the SSTA

The statistical relationship has been examined between the TsJA for every month and the global SSTA. For the TsJA in July, a good relationship exists when the SSTA leads the TsJA by a few months (Fig. 16). In the simultaneous (lag = 0) relation, the warmer than normal TsJ for July correlates with warmer than normal SST and conversely the colder TsJ correlates with the colder than normal SST southeast of the Philippines in agreement with Kurihara (1984). The July temperature tends to be higher than normal in years when the Baiu season ends earlier than normal and vice versa. There is high correlation northeast of the Philippines during June or May. The SSTA for April already has a region with $r > 0.5$ far northeast of the Philippines. Together with the migrating positive correlation region over the western Pacific, there is a region with negative correlation over the equatorial eastern Pacific.

It appears from Fig. 16 that the SSTA slowly propagates westward around 14°N, with the North Equatorial Current, until it reaches the Philippines. It is interesting to note the resemblance between the movement of the high correlation area and the slow westward propagation of the oceanic heat content anomaly mentioned by McCreary (1983) and others. Miyakoda *et al.* (1988) has found, by using an ocean GCM with atmospheric forcing, that before El Niño occurs, the positive oceanic heat content anomaly in the 325 m layer slowly propagates westward in the western subtropical ocean (5°-15°N and S), preceding its reflection at the Philippines and New Guinea and eastward propagation of the ocean-atmosphere coupled mode at the equator. It may be plausible that the movement of the high correlation area is a manifestation of the previously mentioned oceanic heat content anomaly propagation.

There is no meaningful relationship between the TsJA for June and the SSTA. On the other hand, there is some relationship between the TsJA for August and the SSTA in the maritime continent during summer (figures not shown), although the correlation is weaker than for the

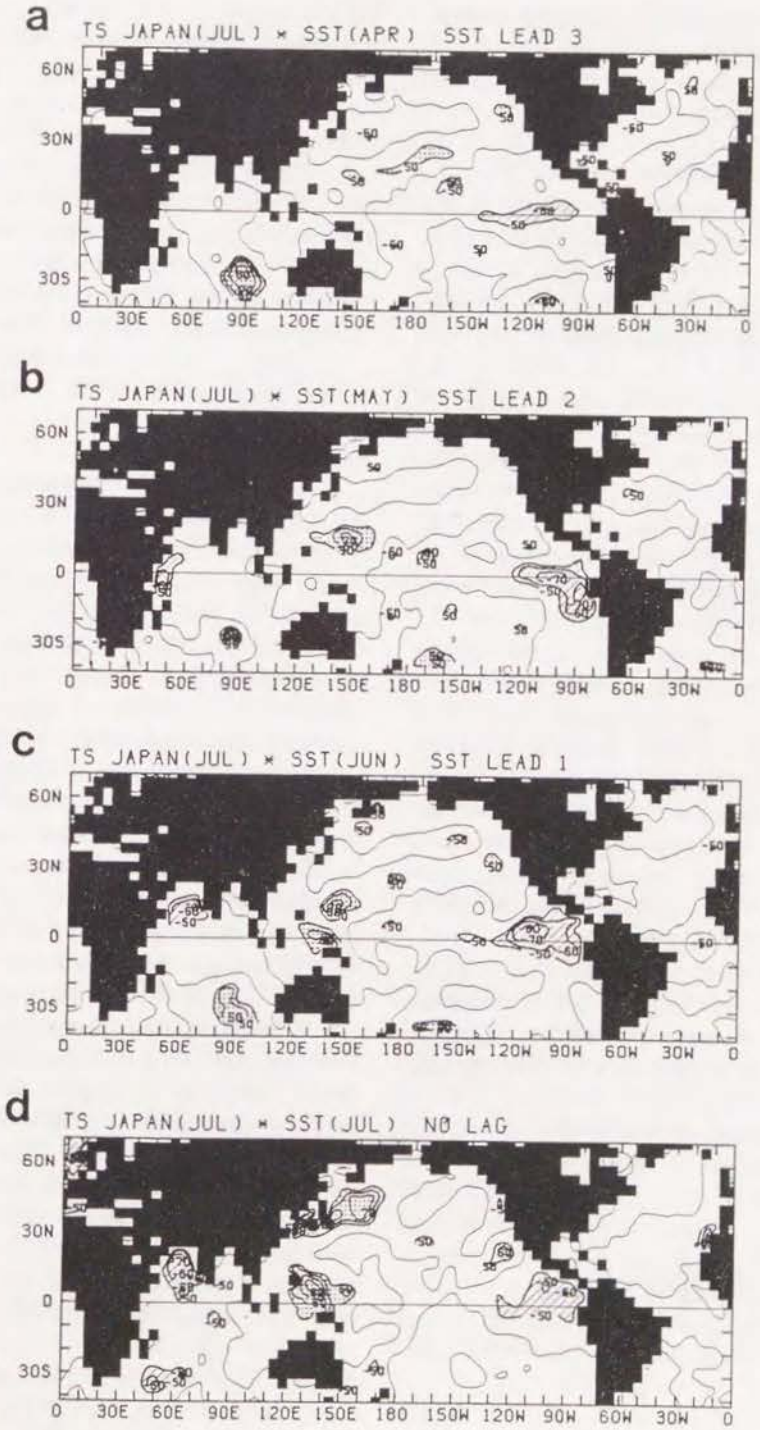

Fig. 16 As in Fig. 1 except for the surface air temperature anomaly for July and the SST anomalies in April, May, June and July.

TsJA in July. A similar relationship between the SST over the western Pacific and the summer weather in Japan is found by Kurihara (1984, 1985) and Nitta (1987).

7. Discussion and summary

The interannual variability of the SST is the largest over the eastern equatorial Pacific as demonstrated by the EOF analysis of Weare *et al.* (1976) and Hsiung and Newell (1983). It is well recognized through GCM studies (*e.g.*, Shukla and Wallace, 1983; Blackmon *et al.*, 1983; Geisler *et al.*, 1985) that atmospheric responses such as the PNA pattern can be obtained for the El Niño SSTA compiled by Rasmusson and Carpenter (1982). Although such a variation over the eastern equatorial Pacific is well related to the weather over North America, correlation with the TsJ in winter was insignificant as was shown in Fig. 13.

Over the western tropical Pacific, the climatological SST is high and a small variability in it could give rise to large atmospheric fluctuations (Simmons *et al.*, 1983; Branstator, 1985; Hamilton, 1988). Tokioka *et al.* (1986) showed the large indirect impact of the SSTA over the western Pacific by comparing the atmospheric response to the SSTA composited by Rasmusson and Carpenter (1982) to that where the SSTA westward of 140°E was eliminated.

The present study has shown that it is the SSTA over the central equatorial Pacific and not that over the eastern or western equatorial Pacific which has a significant relationship with the December temperature in Japan and its relevant circulation. It is also shown that the TsJA for December is significantly correlated with the SSTA at 0°N, 160°W, but the TsJA for November, January or February is not, while the TsJA for January and February is significantly correlated with the SSTA at 40°N, 150°W. The corresponding anomaly circulation pattern is different between December and January.

The impact of the SSTA over the North Pacific and/or the North Atlantic on the winter northern atmosphere has been examined, with a review by Frankignoul (1985). Earlier attempts by GCM studies (*e.g.*, Houghton *et al.*, 1974; Kutzbach *et al.*, 1977) did not show significant atmospheric responses to a mid-latitude SSTA with a reasonable magnitude. However their model integrations were relatively short. Palmer and Sun (1985) investigated the response of the U.K. Meteorological Office GCM to a SSTA over the North Atlantic near Newfoundland. The model's response was statistically significant, although the amplitude was small. Pitcher *et al.* (1988) using the NCAR GCM under perpetual January conditions found the PNA-like response to the SSTA in the North Pacific for the 1976/77 winter. More studies of the possible effects of the mid-latitude SSTA on the atmosphere are still needed.

It was shown that the relationship between the SST and the TsJ in December is quite different from that in January or February. These imply that the characteristics of the atmospheric circulation in December are different from those in Januay or February. Branstator (1984) showed the observational evidence for a link between the zonal mean flow and quasi-stationary eddies while Kang and Lau (1986) have found this zonal/eddy relationship in GCM experiments. The nature of the subtropical jet in December is different from that in January or February. The 6-year mean zonallly averaged zonal wind at 200 mb for December (1978 to 1983) has a maximum of 37.3 ms^{-1} at 32.5°N, while it has its maximum of 44.0 and 46.0 ms^{-1} at 30.0°N for January and February (1979 to 1984), respectively. Thus, the zonally averaged zonal wind in December is substantially weaker than that in January or February. This may be related to the different relationship between the SST and the TsJ in the winter months. Orography as well as SST anomalies must play an important role in such a zonal/eddy relationship.

Kitoh (1988) performed ten 180-day runs with the MRI-GCM under perpetual January conditions and obtained a circulation pattern relevant to a warm winter in Japan for run AW (the composited SST when Japan experienced warm winters) or for run A7 (positive SSTA over the equator east of the dateline), but not for run A5 (very close to A7, but positive SSTA south of the equator on the dateline).

The composited SSTA for AW (Fig. 2 in Kitoh, 1988) include the positive anomalies around 40°N, 150°W and near Japan as well as over the central and eastern equatorial Pacific Ocean. Both AW and A7 show roughly similar atmospheric responses but are slightly different in their detail. The 500 mb height anomalies in AW (not shown, but see Fig. 15 in Kitoh, 1988, for the stream function anomalies at 200 mb) show an anticyclonic anomaly over the entire North Pacific, while that in A7 is more concentrated in the eastern hemisphere. These differences qualitatively agree with the different correlation patterns of the Z500 to the SSTA at 0°, 160°W in December and to the SSTA at 40°N, 150°W in January (Fig. 7). This suggests a non-negligible role of the SSTA around 40°N, 150°W in AW. Moreover, the high sensitivity of the atmospheric response to the position of the SSTA, shown by the results of A7 and A5, seems to be consistent with the present result (Fig 1). A precise comparison between the present analyses and the numerical experiment by Kitoh (1988) is not possible because the latter is performed under perpetual January conditions. However these results encourage further studies on air-sea interactions and their role in the zonal/eddy relationship.

Seasonal means are often used in studies of long-range weather forecasting, mainly because the sampling error or noise level can be reduced by increasing the averaging period (Leith, 1973). This strategy obscures the signal in the present case as discussed with respect to Fig. 8. If the three-month mean TsJA for December, January and February is used, the resulting lag-correlation maps are different from those shown in Figs. 1, 2 and 3. There is no significant correlation over the tropical Pacific, while there is still a high correlation over the North Pacific when the SSTA leads the TsJA with high correlations over the central Pacific around 20°N and near Japan when the TsJA leads the SSTA. This is not surprising since the SSTA over the central equatorial Pacific correlates well with the TsJA only in December. Thus, taking a simple seasonal average may not be justified for some types of study or for long-range weather forecasting if there is a strong sensitivity in the atmospheric response to the SSTA with a time-scale less than a season, due to possible changes in the zonally averaged field over that time-scale. It should be stressed that the present study does not claim that the monthly average is the most appropriate. A suitable averaging period or different means should be further investigated.

The results of this study may be summarized as follows:

(1) The TsJA for December is highly correlated with the SSTA over the central equatorial Pacific around 0°N, 160°W, but not with that over the western or eastern Pacific. Since the SSTA in this area persists for a long period, a significant relationship holds back to the summer, with the SSTA leading the TsJA by half a year. For the TsJA of January or February, there is no significant relationship with the SSTA in the tropics. Therefore, this relationship cannot be obtained by three-month mean data.

(2) The TsJA for January or February is highly correlated with the SSTA over the North Pacific around 40°N, 150°W for a lag of 0 to 2 months with a lead in the SST. Thus the effect of the SSTA in the middle latitudes on the atmosphere should be more thoroughly investigated.

(3) The corresponding circulation anomaly in December is different from that in January or February, although both are associated with an anomalous southerly wind and warm air advection near Japan.

(4) It was also found that the TsJA and the associated circulation pattern in March are highly correlated with the following El Niño.

(5) In summer there is a high correlation between the SSTA over the western Pacific and the TsJA for July.

Acknowledgments

The author wishes to express his thanks to T. Tokioka of the MRI for his continuous encouragement and discussions throughout this work and to K. Kurihara, T. Yasunari and a reviewer for helpful comments on an earlier draft. Thanks are extended to members of the Long-Range Forecast Division of the JMA for discussions during the investigation of this paper.

Computations are made with HITAC M-280D at the MRI.

References

Aoki, T., 1985: A climatological study of typhoon formation and typhoon visit to Japan. *Pap. Met. Geophys.*, **36**, 61-118.

Asakura, T., 1980: Long-range Forecast, in *Climatic Change and Long-range Forecast* by J. Nemoto and T. Asakura, Asakura Publishing Company, 202 pp. (in Japanese)

Barnett, T.P., 1985; Variations in near-global sea level pressure. *J. Atmos. Sci.*, **42**, 478-501.

Barnston, A.G. and R.E. Livezey, 1987: Classification, seasonality and persistence of low-frequency atmospheric circulatin patterns. *Mon. Wea. Rev.*, **115**, 1083-1126.

Bjerknes, J., 1966: A possible response of the atmospheric Hadley circulation to equatorial anomalies of ocean temperature. *Tellus*, **18**, 820-829.

———, 1969: Atmospheric teleconnections from the equatorial Pacific. *Mon. Wea. Rev.*, **97**, 163-172.

Blackmon, M.L., J.E. Geisler and E.J. Pitcher, 1983: A general circulation model study of January climate anomaly patterns associated with interannual variation of equatorial Pacific sea surface temperatures. *J. Atmos. Sci.*, **40**, 1410-1425.

Branstator, G., 1984: The relationship between zonal mean flow and quasi-stationary waves in the mid-troposphere. *J. Atmos. Sci.*, **41**, 2163-2178.

———, 1985: Analysis of general circulation model sea-surface temperature anomaly simulation using a linear model. Part I: Forced solution. *J. Atmos. Sci.*, **42**, 2225-2241.

Davies, R.E., 1976: Predictability of sea surface temperature and sea level pressure anomalies over the North Pacific Ocean. *J. Phys. Oceanogr.*, **6**, 249-266.

Frankignoul, C., 1985: Sea surface temperature anomalies, planetary waves, and air-sea feedback in the middle latitudes. *Rev. Geophys.*, **23**, 357-390.

Gambo, K. and K. Kudo, 1983: Three-dimensional teleconnections in the zonally asymmetric height field during the Northern Hemisphere winter. *J. Meteor. Soc. Japan.*, **61**, 36-50.

Geisler, J.E., M.L. Blackmon, G.T. Bates and S. Munoz, 1985: Sensitivity of January climate response to the magnitude and position of equatorial sea surface temperature anomalies. *J. Atmos. Sci.*, **42**, 1037-1049.

Hamilton, K., 1988: A detailed examination of the extratropical El Niño/Southern Oscillation events. *J. Climatology*, **8**, 67-86.

Houghton, D.D., J.E. Kutzbach and M.McClintock, 1974: Response of a general circulation model to sea surface temperature perturbations. *J. Atmos. Sci.*, **31**, 857-868.

Hsiung, J. and R.E. Newell, 1983: The principal nonseasonal modes of variations of global sea surface temperature. *J. Phys. Oceanogr.*, **13**, 1957-1967.

Iwasaka, N., K. Hanawa and Y. Toba, 1987: Analysis of SST anomalies in the North Pacific and their relation to 500 mb height anomalies over the Northern Hemisphere. *J. Meteor. Soc. Japan*, **65**, 103-114.

Japan Meteorological Agency, 1981: *Manual of One-month Weather Forecasting in Japan*. Technical Note for Long-range Forecasting No. 11, JMA, 301 pp. (in Japanese)

Kanaya, T., 1988: On the process of transitions between circulation regimes during winter over the Pacific and North America. *J. Meteor. Soc. Japan*, **66**, 277-290.

Kang, I.-S. and N.-C. Lau, 1986: Principal modes of atmospheric variability in model atmospheres with and without anomalous sea surface temperature forcing in the tropical Pacific. *J. Atmos. Sci.*, **43**, 2719-2735.

Kawamura, R., 1984: Relation between atmospheric circulation and dominant sea surface temperature anomaly pattern in the North Pacific during the northern winter. *J. Meteor. Soc. Japan*, **62**, 910-916.

———, 1986: Seasonal dependency of atmosphere-ocean interaction over the North Pacific. *J. Meteor. Soc. Japan*, **64**, 363-371.

Mimoto, M., 1987: *Analysis of recurrent flow patterns in the Northern Hemisphere winter*. M.S. Thesis, Univ. of Calif., Los Angeles, 104 pp.

Kitoh, A., 1988: A numerical experiment on sea surface temperatures and warm winter in Japan. *J. Meteor. Soc. Japan*, **66**, 515-533.

Kurihara, K., 1984: Analysis of the statistical relationship between the end of the Baiu in Tokyo and sea water temperatures in the western tropical Pacific Ocean. *Geophys. Mag.*, **41**, 159-171.

———, 1985: Relationship between the surface air temperature in Japan and sea water temperature in the western tropical Pacific during summer. *Tenki*, **32**, 407-417. (in Japanese)

———, 1988: ENSO and long-range weather forecasting. *Kaiyo-kagaku*, **20**, 284-289. (in Japanese)

——— and M. Kawahara, 1986: Extremes of East Asian weather during the post ENSO years of 1983/84. – Severe cold winter and hot dry summer –. *J. Meteor. Soc. Japan*, **64**, 493-503.

Kutzbach, J.E., R.M. Chervin and D.D. Houghton, 1977: Response of the NCAR general circulation model to prescribed changes in ocean surface temperature. Part I: Mid-latitude changes. *J. Atmos. Sci.*, **34**, 1200-1213.

Lanzante, J.R., 1984: A rotated eigenanalysis of the correlation between 700 mb heights and sea surface temperatures in the Pacific and Atlantic. *Mon. Wea. Rev.*, **112**, 2270-2280.

Leith, C.E., 1973: The standard error of time-average estimates of climatic means. *J. Appl. Meteor.*, **12**, 1066-1069.

McCreary, J.P., 1983: A Model of tropical ocean-atmosphere interaction. *Mon. Wea. Rev.*, **111**, 370-389.

Miyakoda, K., A. Rosati, R. Gudgel and Y. Chao, 1988: Study of the 1982/83 El Niño and Southern Oscillation with uncoupled GCMs. Part I: El Niño sequence. (Submitted to *Mon. Wea. Rev.*)

Namias, J., 1959: Recent seasonal interactions between North Pacific waters and the overlying atmospheric circulation. *J. Geophys. Res.*, **64**, 631-646.

———, 1963: Large-scale air-sea interactions over the North Pacific from summer 1962 through the subsequent wnter. *J. Geophys. Res.*, **68**, 6171-6186.

———, 1967: Further studies of drought over Northeastern United States. *Mon. Wea. Rev*, **95**, 497-508.

———, 1968: Long range weather forecasting – history, current status and outlook. *Bull. Amer. Met. Soc.*, **49**, 438-470.

———, 1969: Seasonal interactions between the North Pacific Ocean and the atmosphere during the 1960's. *Mon. Wea. Rev.*, **97**, 173-192.

———, 1978: Multiple causes of the North American abnormal winter 1976-77. *Mon. Wea. Rev.*, **106**, 279-295.

Nitta, T., 1987: Convective activities in the tropical western Pacific and their impact on the Northern Hemisphere summer circulation. *J. Meteor. Soc. Japan*, **65**, 373-390.

Palmer, T.N. and Z. Sun, 1985: A modelling and observational study of the relationship between sea surface temperature in the norh-west Atlantic and the atmospheric general circulation. *Quart. J. Roy. Met. Soc.*, **111**, 947-975.

Panofsky, H.A. and G.W. Brier, 1958: *Some Applications of Statistics to Meteorology*. The Pennsylvania State University, 224 pp.

Parker, D.E., 1983: Documentation of a Southern Oscillation index. *Met. Mag.*, **112**, 184-188.

Pitcher, E.J., M.L. Blackmon, G.T. Bates and S. Munoz, 1988: The effect of North Pacific sea surface temperature anomalies on the January climate of a general circulation model. *J. Atmos. Sci.*, **45**, 173-188.

Rasmusson, E. and T. Carpenter, 1982: Variations in tropical sea surface temperature and surface wind fields associated with the Southern Oscillation/El Niño. *Mon. Wea. Rev.*, **110**, 354-384.

Ratcliffe, R.A.S. and R. Murray, 1970: New lag associations between North Atlantic sea temperatures and European pressure, applied to long-range weather forecasting. *Quart. J. Roy. Met. Soc.*, **96**, 226-246.

Rowntree, P.R., 1972: The influence of tropical east Pacific Ocean temperature on the atmosphere. *Quart. J.R. Met. Soc.*, **98**, 290-321.

Shukla, J. and J.M. Wallace, 1983: Numerical simulation of the atmospheric response to equatorial Pacific sea surface temperature anomalies. *J. Atmos. Sci.*, **40**, 1613-1630.

Simmons, A.J., J.M. Wallace and G.W. Branstator, 1983: Barotropic wave propagation and instability, and atmospheric teleconnection pattern. *J. Atmos. Sci.*, **40**, 1363-1392.

Tokioka, T., A. Kitoh and A. Katayama, 1986: Atmospheric response to the sea surface temperature anomalies in the mature phase of El Niño: Numerical experiment under the perpetual January condition. *J. Meteor. Soc. Japan*, **64**, 347-362.

Trenberth, K.E. and D.J. Shea, 1987: On the evolution of the Southern Oscillation. *Mon. Wea. Rev.*, **115**, 3078-3096.

van Loon, H. and J.C. Rogers, 1978: The seesaw in winter temperatures between Greenland and northern Europe. Part I: General description. *Mon. Wea. Rev.*, **106**, 296-310.

Wada, H., 1969: *Chokiyoho shinko. (New Aspects in Long-range Weather Forecasting)* Chijin shokan, 234 pp. (in Japanese)

Wallace, J.M. and D.S. Gutzler, 1981: Teleconnections in the geopotential height field in the northern hemisphere winter. *Mon. Wea. Rev.*, **109**, 784-812.

Weare, B.C., 1986: Extension of an El Niño index. *Mon. Wea. Rev.*, **114**, 644-647.

———, A.R. Navato and R.E. Newell, 1976: Empirical orthogonal analysis of Pacific sea surface temperatures. *J. Phys. Oceanogr.*, **6**, 671-678.

日本の気温と全球海面水温の関係

鬼 頭 昭 雄
（気象研究所気候研究部）

日本の気温と全球海面水温との関係について月平均値を用いて調べた。12月の日本の気温とそれに先だつ中部赤道太平洋（0°N，160°W）の海面水温との間には高い相関がある。この海域の海面水温偏差の持続性は高く，半年前の6月から高相関が続く。しかし11月や1・2月の日本の気温との相関は低いため，3か月平均値を使うと有意な相関は得られない。1・2月の日本の気温は，前年の11月以降の40°N，150°W付近の海面水温と高相関がある。これらの違いは12月と1・2月の東西平均帯状流などの基本場の相違から来ると考えられる。またそれぞれの暖冬・寒冬パターンは異なっている。さらにエル・ニーニョに先行する3月の日本の気温と，その後の夏から冬にかけての東部赤道太平洋の海面水温との間に高い相関が見出された。夏の日本の気温に対しては，初夏の西部太平洋の海面水温と7月の気温の高相関が確認された。

Interannual Variations of the Tropical Atmosphere in an Atmospheric GCM Forced by the 1970–1989 SST

By Akio Kitoh

Meteorological Research Institute, Tsukuba, Ibaraki 305, Japan

November 1990

Abstract

Interannual variations of the tropical atmosphere in a 20.5 year integration with an atmospheric general circulation model (GCM) forced by the observed near–global (40°S–60°N) sea surface temperatures from September 1969 to February 1990 are presented.

Simulated interannual variations in the tropical Pacific related to El Niño/Southern Oscillation (ENSO) are comparable to the observed. An eastward propagating signal which moves from the Indian Ocean to the central Pacific taking about one and a half year is clearly demonstrated by the 850 mb zonal wind not only in the observed data but also in the simulated fields.

The annual cycle and interannual variations of wind stresses over the tropical Pacific are investigated. The empirical orthogonal function (EOF) analysis of the zonal wind stress anomalies shows that the simulated first and second EOF modes resemble the observed counterparts both in its spatial structure as well as the coefficient time-series. The eastward propagation of the zonal stress anomalies represented by these two modes has been reproduced by the GCM. However the model tends to show smaller zonal wind stresses over the western tropical Pacific during a development stage of ENSO. The magnitude of the simulated meridional wind stress over the equatorial Pacific is much smaller than the observation in its mean annual cycle as well as in its interannual variations, although its spatial structure and time evolution is very similar to the observed.

1. Introduction

This paper describes the response of the tropical atmosphere of the Meteorological Research Institute (MRI) general circulation model (GCM) to the prescribed interannually varying sea surface temperatures (SST) over the period 1970–1989. Similar GCM experiments using evolving prescribed SST to examine the atmospheric variability in the tropics with respect to El Niño/Southern Oscillation (ENSO) have been reported by Lau (1985, 1988), Graham *et al.*(1989), Storch *et al.*(1989) and Latif *et al.*(1990).

Lau (1985) has forced the Geophysical Fluid Dynamics Laboratory (GFDL) GCM with the observed tropical Pacific SST for the period 1962–1976 and has assessed the model capability to simulate meteorological features relevant to ENSO. Lau (1988) has relaxed the limitation of the tropical Pacific SST of Lau (1985) to incorporate near-global (north of 40°S) SST variations. Graham *et al.*(1989) have described the response of the National Center for Atmospheric Research (NCAR) GCM surface wind stress over the tropical Pacific to the observed SST for the period 1961–1972. They show that the NCAR GCM reproduces the central equatorial Pacific zonal wind stress which resembles observed ENSO-related changes, but not away from the equatorial regions. Moreover, the overall amplitude of the GCM response is about the half of the observed. Storch *et al.*(1989) and Latif *et al.*(1990) have integrated the European Centre for Medium Range Weather Forecast (ECMWF) GCM for 16 years using the near global 1970–1985 SST. The principal component analysis of the observed tropical Pacific zonal wind stress reveals that the two leading modes are related with ENSO and they explain the eastward propagation of the westerly wind stress anomaly. They show that the model succeeds to reproduce the observed first mode with less magnitude but fails for the second mode. Thus no eastward propagation is simulated.

Such a study to assess the model capability to simulate meteorological features relevant to ENSO is important because atmospheric responses to the SST anomalies, particularly surface wind stresses, are among key factors of the interaction processes for a coupled

ocean–atmosphere GCM. As the climate system, of course, evolves under mutual interactions between atmosphere and ocean, it is not sufficient to have an atmospheric/oceanic GCM which responds to the prescribed oceanic/atmospheric forcings and completely simulates the interannual variations of the atmosphere/ocean. However, it is meaningful to fully understand behaviors of respective medium of the coupled ocean–atmosphere GCM, here an atmospheric part of it, upon the forcing of the other part. And it is also necessary to add another literature here with a GCM whose physical processes are differently parameterized than others.

We begin in section 2 by giving a model outline. Sections 3–6 present the tropical atmosphere responses to evolving SST by using some indices over the central equatorial Pacific, a lagged correlation method, Hovmöller analysis and principal component analysis of the simulated and observed surface wind stress over the tropical Pacific. Some concluding remarks follow in section 7.

2. The model and the experiment

a. Model

The model (MRI·GCM) used for this study is a 5-level atmospheric general circulation model. The model is of grid representation with a horizontal resolution of 4° latitude and 5° longitude with a top at 100 mb. Physical processes included are the parameterized cumulus convection, planetary boundary layer (PBL), radiation interactive with model-generated cloud. Ground hydrology parameterization predicts snow mass and ground soil moisture. Diurnal as well as seasonal variation of insolation is included. Details of this model (MRI·GCM-I) are described in Tokioka *et al.*(1984) and the mean statistics of a 12-year run under the climatological SST in Tokioka *et al.*(1986).

Some modifications have been made to MRI·GCM-I. The Arakawa and Schubert (1974) cumulus parameterization scheme is modified to impose an additional constraint between the minimum entrainment rate and the depth of the predicted PBL layer (Tokioka *et al.*, 1988). This modification lowers the maximum level of the heating when compared with the original model and provides favorable conditions for the occurrence of the equatorial intraseasonal oscillation. We now use the observed seasonally varying surface albedo over land compiled by Matthews (1983). Surface albedo over the snow is a function of snow depth and the terrain height dependent masking depth. The model uses the one-layer bucket model, in which field capacity is a function of latitude with large value in the tropics (15 g cm^{-2} at the equator) and small value in high latitudes (3 g cm^{-2} poleward of 60° latitude). This makes an improvement of summer surface air temperatures over the Eurasian continent where the MRI·GCM-I shows systematically cooler temperature in summer. The effect of sub-grid scale topography is incorporated by increasing surface drag coefficients over the continents as a function of the standard deviation of sub-grid scale topography after Yagai and Tokioka (1987).

b. Experiment

A 20.5 year integration has been performed with the prescribed SST from September 1969 to February 1990 over the worldwide oceans for 40°S–60°N. They are from Climate Analysis Center/NOAA before 1984 and from Numerical Prediction Division/JMA after 1985. There may be some small differences between the two datasets due to different analysis method, but no adjustment is made in this study. Polewards of these latitudes we use Alexander and Mobley (1976) climatological SST. For the sea ice distributions climatological seasonal change is prescribed.

For this particular experiment one year consists 360 days and each month is 30 days long. Monthly means are used for most part of the analyses of this paper. A five-month running mean filter is applied to the original data to remove the high-frequency fluctuations.

c. Observed data

In order to compare simulated results with observations, we use the Southern Oscillation Index (SOI), surface wind stress and 850 mb wind. SOI used here is the normalized sea-level pressure (SLP) difference between Tahiti and Darwin.

The subjectively analyzed observed wind stress data by Florida State University (FSU) on a 2° by 2° grid as described in Goldenberg and O'Brien (1981) is used. The data covers from January 1961 to May 1989. The FSU pseudo stresses were interpolated on a 4° by 5° grid used in the GCM and were then converted to stresses by multiplying the air density (ρ = 1.2 × 10^{-3} g cm^{-3}) and the constant drag coefficient (C_D = 1.3 × 10^{-3}). It should be noted that the data density is not satisfactory around and south of the equator (Goldenberg and O'Brien, 1981).

Also used are the observed wind at 850 mb and 200 mb provided by the U.S. National Meteorological Center (NMC) which covers a period from January 1979 to December 1987 and outgoing longwave radiation (OLR) for the 12 year period 1975–1987 except 1978.

3. Time-series of tropical Pacific indices

The time-series of some of the simulated tropical Pacific indices are shown in Fig. 1. The five selected variables are SST, the zonal wind at 200 mb (U200), the zonal wind at 850 mb (U850) and the precipitation (RR) in the central equatorial Pacific (averaged for 4°N–4°S, 180°–140°W), and SOI. The model climatology for each month is removed from the original monthly mean data and a five-month running mean filter is applied. The SOI in the model is calculated with the normalized SLP at the model grid point corresponding to Tahiti and Darwin (150°W, 18°S and 130°E, 10°S, respectively). Longitudes, 180°–140°W, are chosen to fully describe the Southern Oscillation. The SST anomaly at 0°N, 160°W has the highest simultaneous correlation with SOI (Kitoh, 1988).

Large interannual variations of the tropical Pacific atmosphere are simulated as a response to the SST forcing. Warm SSTs in 1972/73, 1976/77, 1982/83 and 1986/87 El Niño events accompany upper tropospheric easterly anomalies, lower tropospheric westerly anomalies, above average precipitation and negative SOI. The cold events (La Niña) in 1970/71, 1973/74, 1975/76 and 1988/89 accompany upper tropospheric westerly anomalies, lower tropospheric easterly anomalies, below average precipitation and positive SOI.

Figure 2 shows the time-series of the observed and simulated SOIs. The model reasonably reproduced the observed interannual variations of the large-scale sea-level pressure fields in the Pacific represented by SOI. Large positive and negative SOIs in La Niña and El Niño years, respectively, are captured with the model, although the fluctuations with small amplitudes, such as in 1978–1980, are not well captured.

The simultaneous correlation coefficient between the two curves is 0.74. The correlation becomes maximum with $r = 0.76$ when the GCM leads the observation one month. This may reflect the immature development (early decay) of the 1982/83 warm event in the model. The simulated SOI shows a strongly reduced amplitude during the later stage of the 1982/83 event. The simulated SOI becomes minimum in September 1982, which is 4 months earlier than

and about a half of the magnitude of the observed SOI. In the 1982/83 winter (December–Januar–Februar), low-pressure area spreads over the eastern Pacific, extending toward the South Pacific. The GCM does simulate low-pressure area over the equatorial eastern Pacific corresponding to the above normal precipitation there, but its horizontal extent shrunk much from the previous season and is smaller than the observed counterpart and high-pressure area is simulated over the eastern South Pacific. In January 1983 in the model, the Tahiti SLP has only -0.3 standard deviation while the Darwin SLP has $+1.6$ standard deviation. Therefore the east–west pressure redistribution at the equator is well simulated but not off the equator in the Southern Hemisphere at this time. Another discrepancy can be seen in 1973/74 and 1975/76 cold events, when the simulated SOI is much weaker than the real atmosphere. Other events including the very recent 1988/89 cold event are remarkably well simulated.

Lau (1985) has presented the simulated SOI defined by the Tahiti minus Darwin 1000 mb height difference in two 15-year GFDL GCM integrations forced by the 1962–1976 tropical Pacific SST, while Lau (1988) shows indices for the simulation forced by the global 1950–1984 SST. He shows a realistic low-frequency response in simulated SOI and other tropical variables in both cases. A direct comparison of the simulated SOI with the observation is also done by Storch *et al.*(1989) and Latif *et al.*(1990). They used the ECMWF-T21 GCM and forced the model with 1970–1985 SST. On timescales longer than two years, the phase of the simulated SOI is as observed, but the intensity is weaker than the observed. On timescales shorter than one year, the coherence is low. They succeed to simulate the warm events of 1972/73 and 1982/83 and the cold event 1970/71, but fail in simulating the cold events 1973/74 and 1975/76 and the warm event 1976/77.

Another comparison between the simulation and the observation is shown in Fig. 3, which is the monthly eastward surface wind stress anomaly over the equator east of the date-line with a 5-month running mean filter applied. Although the data quality is not good due to rather poor data coverage over the equator (Goldenberg and O'Brien, 1981) and there is some ambiguity about the drag coefficient, there is a remarkable agreement in interannual variation

between the simulated and observed zonal surface wind stress. A correlation coefficient is 0.81 with no time lag. Rapid decay of the observed westerly anomaly in the 1982/83 warm event is not well simulated in the model. This is more thoroughly discussed later in section 3d. Easterly wind stress anomaly in the 1973/74 and 1975/76 cold events is as strong as that in the 1970/71 cold event in both the observed and GCM, although the simulated SOI in the former is much smaller than the latter. In the 1975/76 winter, the east–west pressure gradient over the equatorial Pacific is simulated but the simulated Darwin SLP is above normal due to below normal SST in the maritime continent, resulting the SOI amplitude small. In fact, the SST anomaly in the western Pacific in the 1973/74 and 1975/76 cold events is different from that in the 1970/71 or 1988/89 cold events when warm SST covered the maritime continent region. Therefore the reason of the disagreement of the SOI magnitude in the 1973/74 and 1975/76 events is not clear.

4. Lag-correlations

a. SST

Figure 4 shows lagged correlations between the SST in the central equatorial Pacific (4°N–4°S, 180°–140°W) and the SST (or the ground temperature for land grid points) at the equator on each longitude. And the lagged correlations between the same SST index and the simulated U200, U850 and precipitation at the equator are shown in Fig. 5. The observed counterparts for U200, U850 and OLR are shown in Fig. 6. Note that the observed data covers only 9-year period 1979–1987 and is much more influenced by the largest 1982/83 event than from Fig. 5 which is based on the 20-year simulated data. Lagged correlation maps using the simulated 9-year data for 1979–1987 are also plotted but are not shown. Here the "equator" means the average between 4°S and 4°N. All variables are again passed by a 5-month running mean filter. All seasons are treated without distinction in the calculation. Auto-correlation of the SST index falls to zero at lag = 12 month. Other indices more rapidly decorrelate than the SST. For example U850 decorrelates at lag = 10 month. When we assume the number of degrees of freedom $n = 240/12 - 2 = 18$, correlation coefficients greater than 0.47 are significant at 95% level.

Figure 4 shows the lagged correlations for SST/ground temperatures at the equator. The central equatorial Pacific SST keeps high correlations with the central and eastern equatorial Pacific SST for ± 6 months. This high persistence reflects the fact that the SST anomaly in this region tends to form around boreal early summer, persist throughout autumn and winter until it tends to change its sign in boreal spring (Wallace and Jiang, 1987; Kitoh, 1988).

The western equatorial Pacific SST tends to correlate negatively with the central equatorial Pacific SST, but correlation coefficient is small and insignificant. About one and a half year before the central Pacific SST becomes maximum, the western Pacific SST attains its peak value. But as the rather small correlation coefficients suggest, this relationship does not hold for all major warm/cold events. Individual SST data indicates (Fig. 7) that this is

the case for the 1982/83 warm event and 1973/74 and 1975/76 cold events but not well for others. There is also negatively correlated ocean over the easternmost equatorial Pacific at lag = -1.5 year. The overall picture suggests a frequency peak of the equatorial SST at about 3 years.

The Indian SST has strongly correlated with the central Pacific SST, the Indian SST lagging the Pacific SST for a few ($\sim$4) months. This relationship holds well for most of warm/cold events (Fig. 7). When seasonality is concerned, the variance of the central Pacific SST anomalies is maximum in January followed by November and December and is minimum in northern summer, while the variance of the Indian SST has a semi-annual cycle with the maxima in February and August. The equatorial Atlantic SST also lags the Pacific SST. The lag is half a year to a year and the lag differs from event to event.

b. U200

The response of the upper troposphere zonal wind (U200) at the equator is shown in Fig. 5a. There are significant easterly anomalies over the Pacific when in situ SST is warmer than normal. There is an indication of slow eastward phase propagation with a speed which takes 5–6 years to circle the globe. The observed easterlies (Fig. 6a) are stronger and extend more eastward to the eastern equatorial Pacific than the simulated winds. In the upper troposphere of the tropical Atlantic, there were strong westerly wind anomalies in the 1982/83 event, accompanied by a pair of cyclonic circulations straddling the equator in the tropical America and the Atlantic. This is reflected in the high correlation in the observed U200 (Fig. 6a) and is also simulated in the model and appears in the correlation map when data of the same period 1979–1987 are used (not shown). Over the Indian Ocean, at lag = -6 month, positive correlation is found. This is not well supported by the observed map, but is related to the weak Asian summer monsoon (the tropical easterly jet over India is weak) 6 months prior to the mature phase of El Niño.

c. U850

Comparing lower (U850) and upper (U200) tropospheric zonal wind correlation maps (Figs. 5b and 5a), we notice that the Walker-type circulation anomaly (opposite directions between the lower and upper troposphere) with eastward phase propagation is distinct over the Pacific. In the model, U850 has systematically larger magnitude in correlations with the SST than U200 has. At lag = 0, when the central equatorial Pacific SST anomaly is positive, 850 mb zonal wind anomaly is westerly between 160°E and 140°W and easterly between 80°E and 120°E and between 100°W and 40°W (with correlation coefficient larger than 60%). There are significant anomalous easterlies at 200 mb over the Pacific, indicating a Walker-type circulation anomaly. This east–west circulation is also seen over the Atlantic but with less correlation. Over the equatorial Indian Ocean, however, the anomalous upper tropospheric wind is not well organized in the model. In the model at the mature phase of El Niño, there are anomalous westerlies over Indochina and west of Australia, flowing equatorward to New Guinea converging with easterlies over the central equatorial Pacific (not shown). The maximum correlation is found when U850 leads SST by one month due to the 5-month running mean filtering.

Longitudes with large correlations with the central equatorial Pacific SST can be traced back westward as time goes back. U850 over the western equatorial Pacific at lag = -1 year has significantly large correlation with the central Pacific SST. This anomalous U850 seems to be propagated from far more westward from the Indian Ocean where correlation is maximum with a lead of 20 months when there is a negative anomaly over the central Pacific. This relationship is also confirmed by the 9-year observed data (Fig. 6b). This westerly anomaly over the Indian Ocean corresponds to the small but positive SST anomalies over the maritime continent at lag = -1.5 year (Fig. 4). This is not inconsistent with Barnett's (1983) finding, by complex EOF analysis of surface winds for the period 1952–1978, of a traveling disturbance which moves from the Indian Ocean eastward into the Pacific, preceding El Niño events. U200 has a smaller but similar lagged correlation pattern.

d. Precipitation

The simulated precipitation field is very noisy even in one-month mean maps. So 9-point spatial smoothing is done to the precipitation field before correlations are calculated (Fig. 5c). For the observed counterpart, we use the OLR data for the period 1979–1987 (Fig. 6c).

The overall pattern of the correlation map for the simulated precipitation is similar to that for the SST (Fig. 4). Above normal precipitation is simulated over the central equatorial Pacific when SST there is warmer than normal. At the same time, although not so significant, below normal precipitation is found over the western Pacific and the Atlantic and above normal precipitation over the Arabian Sea. They are all in accord with the observation. The SST anomaly over the equatorial Indian Ocean showed significantly high correlation with the central equatorial Pacific SST from lag = 0 to lag = +12 month. However this is not reflected in the simulated precipitation nor the observed OLR. Figure 6c shows that the longitudes of correlation maximum migrate from the central Pacific at lag = 0 to the eastern Pacific at lag = +4 month. This is associated with the SST field for the period, particularly with the 1982/83 event, and is also simulated with the GCM (not shown). Some other correlation maxima, *e.g.*, over the western Pacific at lag = -1 year and over the eastern Pacific at lag = -1.5 year, are accompanied by the SST peaks (Fig. 4).

5. Hovmöller maps

In order to examine individual year-to-year variations of the simulated equatorial atmospheric fields in more detail, Hovmöller diagrams of surface zonal wind stress and precipitation fields are compared with those of the observed counterparts.

a. SST

We begin with Fig. 7 which shows the longitude-time section of the prescribed SST over the ocean and the simulated ground temperature over land grid points. A climatology is removed and then 5-month running mean is applied. Time sequence of equatorial SST anomalies is discussed by many investigators with respect to ENSO phenomenon (*e.g.*, Rasmusson and Carpenter, 1982). The major warm and cold events can be clearly identified. SST anomalies in the Indian Ocean lagging a few months from those in the eastern Pacific, as found in Fig. 4, are seen in 1972/73, 1982/83 and 1986/87 warm events and 1973/74 and 1975/76 cold events. In the equatorial Atlantic still more lagging SST anomalies are also seen in those events. The warm SST anomalies in the central and eastern equatorial Pacific in 1972/73, 1982/83 and 1986/87 warm events are preceded by the positive anomalies in the western Pacific (120°E–150°E).

b. Precipitation

Next we compare the GCM responses with the observation. First, the simulated precipitation at the equator is shown in Fig. 8. This is compared with the observed OLR field (Fig. 9). A nine-point smoothing is applied to the noisy simulated precipitation field to make a comparison easy.

The simulated precipitation field shown by this Hovmöller diagram is less organized than the observed counterpart. The OLR anomaly field shows a distinct east–west contrast among strong convections in the central and eastern Pacific and weak convections in the western

Pacific and in the Atlantic in 1982/83 and 1986/87 warm events. A reversed situation is the case for the remaining period. The model reproduces well the precipitation field in 1982/83 El Niño with above normal precipitation with two maxima at 140°W in 1982/83 winter and at 90°W in 1983 spring. Below normal precipitation in the western Pacific and Atlantic is also simulated. During 1984–1986, there is a tendency with above normal precipitation west of the dateline, but this location is situated 20° eastward of the observed longitude dividing positive and negative anomalies.

c. Zonal wind stress

Next we compare the simulated zonal component of the surface wind stress at the equator (Fig. 10) with the FSU wind stress (Fig. 11). The GCM reproduces well the observed zonal wind stress anomalies. The eastward propagation of the stress anomaly and its amplification around the dateline are characteristic of not only the observed but also the simulated fields.

It is shown by the simulated Hovmöller diagram that the eastward propagation of the zonal wind stress anomaly is not confined in the Pacific but can be traced back to the maritime continent around 120°E and even in the Indian Ocean. The phase velocity of the eastward propagation is 0.2∼0.25 m s^{-1} or 50°∼70°longitudes per year, which corresponds to a speed to circle the globe in 5–6 years. This eastward phase propagation is seen in almost all events which attain large amplitude at the dateline. Thus the eastward propagation seen by the lagged correlation maps of zonal wind in Fig. 5 is not an artifact of a sole strong event, but rather a representative of equatorial interannual variations.

There are some differences between the simulated and the observed zonal wind stress in the equatorial Pacific. Firstly, the simulated wind stress reaches its maximum at about 10° eastward than the observed. Secondly, the shape of the simulated stress anomalies as seen in the Hovmöller diagram is fattish compared to the observed. This is seen in the major warm events such as in 1972/73 or 1982/83. The observed stress anomaly field shows a steady eastward movement with a phase speed of 90° longitude per year. On the other hand,

the GCM produces more eastward (~180°W) establishment of the anomaly and the more westward (~140°W) decay of the anomaly than the observed, thus of the twice slower phase speed with 40° longitude per year. We explore more on this difference in the next subsection in terms of the principal component analysis.

6. Variability of the surface wind stress over the tropical Pacific

In this section, the simulated wind stress is compared with the observation with respect to its annual cycle and interannual variations. Analyses are restricted to the tropical Pacific where the FSU dataset is available.

a. Annual cycle

Graham *et al.*(1989) have examined the annual cycle of the tropical wind fields, simulated by the GCMs at Oregon State University (OSU), ECMWF and NCAR. They show that these models show similar bahavior and resemble the real atmosphere more in major trade wind regions than in convectively active areas with light winds. These models have similar horizontal resolutions to the MRI·GCM, but vertical resolutions and physical parameterizations vary considerably.

Figure 12a and 12c shows the annual mean zonal wind stress for the observed and for the GCM, respectively. The strongest trade wind exceeding 0.08 N m^{-2} is observed south of Hawaii. The axis of strong trade winds extends toward the Philippines. These features are quite well simulated by the MRI·GCM. In the Southern Hemisphere, the strong trade wind is located around 20°–10°S, 120°–100°W and there is another strong wind area east of Australia. Regions extending east-south-eastward from north of New Guinea are confluent regions with light wind, corresponding to the South Pacific convergence zone (SPCZ). The intertropical convergence zone (ITCZ) over the eastern Pacific around 5°N is also discerned as locally weak wind regions. The model has succeeded to reproduce these prominent annual mean features quite well.

One notices weaker easterlies in the GCM than in the observed over the western Pacific from the dateline to east of the Philippines. On the other hand, north of 20°N, the simulated easterlies are stronger than the observed. These suggest a northward displacement of the subtropical high in the GCM (Tokioka *et al.*, 1986). At the equator the model has simulated proper magnitude of the easterlies.

To extract the annual cycle, climatological monthly means of the zonal wind stresses are first constructed. These monthly means are then Fourier analyzed and the amplitude and phase of the annual component are obtained at each grid point. Figure 12b and 12d shows the observed and simulated annual component of the zonal wind stress expressed by a vector format. The length of arrows is proportional to the amplitude and the direction indicates the phase. Arrows pointing toward north indicate maximum on 1 January and arrows pointing toward east indicate maximum on 1 April and so on.

In the first place, the amplitude of the annual component is large equatorward of the mean positions of the strong annual mean trade winds. In the Northern Hemisphere, along 10°N, westerly component becomes strongest in August and September. Easterly trade winds intensify in February and March and weaken in August and September at 10°N. In the western Pacific, easterlies weaken in July and August. In other words, trade winds migrate equatorward and expand westward in northern winter and spring, followed by poleward migration and eastward contraction in northern summer and fall (*e.g.,* Goldenberg and O'Brien, 1981; Graham *et al.*, 1989). In the Southern Hemisphere, trade winds migrate equatorward in northern summer over the eastern Pacific and east of New Guinea. They are separated by the SPCZ. Poleward of the annual mean trade wind axes, the annual cycle is opposite as shown by the direction of arrows.

The model (Fig. 12d) reproduces the above mentioned features. Different amplitude from region to region is also simulated. To the south of Hawaii at 10°N, the annual cycle in the GCM lags behind the observation by about one month. In the Southern Hemisphere, the amplitude in the GCM is smaller than the observed to the south of SPCZ and is larger in the eastern Pacific. At the equator to the east of 120°W, relatively large annual cycle of the zonal wind stress is simulated in the GCM while small annual cycle is observed.

The annual mean and the amplitude and phase of the annual component of the meridional wind stress are shown in Fig. 13. Figure 13a clearly shows the mean position of the ITCZ and the SPCZ as the meridional confluent zones. The model (Fig. 13c) does reproduce the

overall pattern as well as the ITCZ and the SPCZ but fails to have a proper magnitude.

Smaller meridional components are the common deficiencies in many GCMs. Graham *et al.*(1989) mention the problems with the model boundary layers and the limited spatial resolution as possible candidates of this discrepancy. A possible reason is a way of treatment of the flux profiles. The problem here is the angle between the surface wind and the PBL mean wind. The current parameterization in the MRI·GCM assumes no turning angles between them, reducing northerly components of the trade winds.

Figure 13b shows the annual cycle of the observed meridional wind stress. This indicates a north–south displacement of the whole system, the ITCZ migrating equatorward in northern winter and spring and the SPCZ migrating equatorward in northern summer and fall, corresponding to the annual cycle of the zonal component. To the east of the Philippines there appear very strong annual cycles with northerly wind stress strengthening in winter. The simulated annual cycle of the meridional wind stress is very weak compared to the observation. Except for the amplitude, the general pattern of the simulated one resembles the observation.

b. Interannual variations

Principal component analysis is performed with the 5-month running mean zonal and meridional wind stress anomalies. Both data cover the tropical Pacific from 26°S to 26°N and from 125°E to 70°W. A total of 394 ocean grid points from November 1969 to March 1989 (233 months) are used.

Figure 14 shows the first and the second empirical orthogonal functions (EOF) and their coefficients of the observed zonal wind stress anomalies over the tropical Pacific. The eigenvectors will be denoted as E_1^{OBS} and E_2^{OBS}, and the coefficients as C_1^{OBS} and C_2^{OBS}. E_1^{OBS} explains 20.7% of the total variance and is characterized by large positive anomalies over the central equatorial Pacific with its maximum on the equator near the dateline. The anomalies extend from the maximum to southeast to 20°S. They are located northeast of

the SPCZ, suggesting zonal convergence/divergence to the SPCZ. Negative anomalies are found over the western Pacific around 20°N and 20°S and over the eastern equatorial Pacific. E_2^{OBS} (14.5%) is characterized by the northwest to southeast contrast of positive and negative anomalies with centers at 145°E, 6°N and 155°W, 6°S. Poleward of about 15° latitude, there are anomalies with a different sign with the equatorial sides.

Lagged correlations between the coefficients, C_1^{OBS} and C_2^{OBS} (Fig. 15a) show that the correlation coefficient is maximum ($r = 0.55$) when C_2^{OBS} leads C_1^{OBS} by 6 months. It is also high when C_1^{OBS} leads C_2^{OBS} by 6 months with $r = -0.42$. This indicates that six months before C_1^{OBS} reaches maximum with the westerly anomaly centered at the equatorial central Pacific, C_2^{OBS} reaches maximum with the westerly anomaly centered at 6°N in the western Pacific, and six months later C_2^{OBS} attains a minimum value with the westerly anomaly centered at 6°S, 150°W, which is to the southeast of the E_1^{OBS} anomaly, and easterly anomaly in the western Pacific. Thus E_1^{OBS} and E_2^{OBS} capture the eastward phase propagation of zonal wind stress anomalies already shown in Fig. 10. This eastward propagation is especially clear in the 1982/83 event. In May 1982, C_2^{OBS} reaches maximum, followed by the C_1^{OBS} maximum on December 1982 and by the C_2^{OBS} minimum on March 1983. A similar feature is also seen in the 1972/73 event. This eastward wind stress anomaly propagation is also described by data analysis by Storch *et al.*(1989) and Latif *et al.*(1990) with a similar approach used here and by Barnett (1983) with complex EOF analysis of surface winds.

Figure 16 shows the simulated EOFs, E_1^{GCM} and E_2^{GCM}, of the tropical Pacific zonal wind stress anomalies. Both the simulated EOFs have succeeded to reproduce spatial structures of the observed; that is, E_1^{GCM} is characterized by the positive anomalies over the central equatorial Pacific whereas E_2^{GCM} is characterized by the positive and negative anomalies to the northwest and southeast, respectively, of the E_1^{GCM} anomalies.

Figure 15b shows the lagged correlations between the observed and the simulated coefficients. Both show large correlation coefficients at lag = 0, but C_1 is better simulated by the

model than C_2 is. Figure 15a indicates that C_1^{GCM} and C_2^{GCM} positively correlates when C_2^{GCM} leads C_1^{GCM} and negatively correlates when C_2^{GCM} lags C_1^{GCM}. Thus the model atmosphere which is the response to the forced SSTs succeeds to reproduce the eastward propagation of the zonal wind stress anomalies with respect to ENSO as observed. The model simulation of this eastward propagation has not been reported up to this time. The simulated lagged correlation between C_1^{GCM} and C_2^{GCM} is, however, smaller than the observed in the C_2–leads–C_1 stage when anomalies propagate from the western Pacific to the central Pacific, while it is similar to the observed in the C_2–lags–C_1 stage when anomalies propagate from the central equatorial Pacific eastwards.

The amplitude of C_1^{GCM} is comparable to that observed (Fig. 14 (top) and Fig. 16 (top)). This indicates that the model tropical atmosphere is responding well to the interannually varying ENSO scale SST fluctuations at least at the mature stage of El Niño/La Niña. However, the amplitude of C_2^{GCM} is smaller than the observed. Smaller variance of E_2^{GCM} relative to that of E_1^{GCM} is manifested by their percentage contributions. The E_1^{OBS} and E_2^{OBS} explains 20.7% and 14.5% of the total variance, while the simulated ones explains 34.9% and 10.2% , respectively. This smaller contribution of E_2^{GCM} is clearly seen in the developing stage of the 1972/73 and 1982/83 El Niños. In fact, C_2^{OBS} is positive straight from early 1981, while C_2^{GCM} is positive only from early 1982. They both change their signs at November 1982. For the 1972/73 case, they are positive from November 1971 to September 1972 for the observation while from April 1972 to September 1972 for the GCM. A close examination of the spatial structures also reveals a slight but systematic difference. The simulated longitudes of the above described centers shifted at least 10° eastward of the observed.

To sum up, the observed zonal wind stress anomaly relevant to ENSO begins to propagate from the equatorial western Pacific, developes and attains its maximum amplitude near the dateline and weakens before it reaches the eastern Pacific. On the other hand, the simulated anomaly begins to form around 150°, rapidly develops and attains its maximum

strength east of the dateline. This different life stage of the anomalies has been reflected in the shape of the anomalies in the Hovmöller diagram in Figs. 10 and 11.

What makes the distortion in the simulated zonal wind stress anomalies in the western Pacific? As has been discussed in section 6a with Fig. 12, the zonal wind stress in the GCM is slightly smaller than the observed in its annual mean magnitude as well as its amplitude of the annual cycle component over the western Pacific between the equator and 20°N. This may be related to the northward displacement of the subtropical high or with the improper realization of the convergence toward the maritime continent related with the convective activity there. This smaller basic annual cycle of the zonal wind stress should affect the interannual variations over the western Pacific region.

Secondly, it is no doubt that the ocean has a strong influence on the atmospheric circulation in the tropics, but the ocean is no single source of the forcings. Some anomalous conditions, for example snow cover extent or accumulation anomalies over the Eurasian continent, would have affected the tropical atmosphere by way of extratropical–tropical interactions. Moreover if tropical cyclones or westerly wind bursts are truly indispensable at the developing stage of El Niños as hypothesized by Keen (1982), Luther *et al.*(1983), Nitta and Motoki (1987) and Nitta (1989), the coarse horizontal resolution adopted here would have prohibited such atmospheric anomalies in the western Pacific.

Figure 17 shows the observed and the simulated first EOFs of the meridional wind stress anomalies. They explain 29.0% and 20.1% of the respective total variance. They are characterized by the convergence (divergence) over the central equatorial Pacific in El Niño (La Niña) years. The model reasonably well reproduces the observed spatial structure and time-series of the coefficient. A correlation coefficient at lag = 0 is 0.93 (Fig. 18b). However the simulated magnitude is much weaker than the observed, a model deficiency as already discussed for its annual cycle (Fig. 13).

Figure 18a shows that the maximum correlation of C_1^{OBS} between the zonal and meridional components is 0.86 when the meridional component lags the zonal component by 2

month. The overall lagged correlation is also large when the meridional first component lags the zonal first component. This indicates that the meridional convergence attains its peak strength after the westerly stress anomaly moves past the dateline and before it reaches 150°W where the second EOF of the zonal stress anomaly has another peak. The model also has some indication of larger correlations when the first meridional component lags the first zonal component, but its asymmetry about lag = 0 is not clear. This is related to the fact that C_1^{GCM} is already lagging C_1^{OBS} in their zonal component (Fig. 15b).

7. Concluding remarks

An atmospheric GCM with its horizontal resolution of 4° latitude by 5° longitude is integrated for 20.5 years using the observed near–global (40°S–60°N) SST from September 1969 to February 1990 and monthly means for the last 20 years are analyzed and compared with the observation.

Prominent features of the ENSO-scale time evolutions of the simulated zonal winds and precipitation at the central equatorial Pacific are realistic. The simulated SOI also remarkably corresponds to the real atmosphere, but in some Southern Oscillation events, such as 1973/74 and 1975/76 cold events and 1982/83 warm event, it is weaker than the observed.

Using lagged correlation analysis, an eastward propagating signal is clearly demonstrated in the area from the Indian Ocean to the central Pacific for a period of about one year and a half, not only in the observed but also in the simulated 850 mb zonal wind fields. This eastward traveling disturbance preceding El Niño events is reported by Barnett (1983) but since then not well confirmed by the observational data. Here we have provided an additional evidence for that. For the 200 mb zonal wind anomalies, some differences are found between the GCM and the observation, particularly over the equatorial Indian Ocean. This needs further investigation.

The model has remarkably well simulated the annual cycle and the interannual fluctuations of the tropical Pacific zonal wind stress. The simulated first and second EOF modes of the zonal wind stress anomalies resemble the observed counterparts both in its spatial structure as well as the coefficient time-series. The eastward propagation of the zonal stress anomalies represented by these two modes has been reproduced by the GCM. However the model tends to show smaller zonal wind stresses over the western tropical Pacific during a development stage of ENSO. This may be related to the model's systematic error of northward displaced subtropical high in the western Pacific, poorer horizontal resolution, the insufficient representation of convective activities or the PBL related problems. It is possible

that the surface flux parameterization over the maritime continent where surface winds are generally weak will have large effect on the atmospheric circulations (Kitoh and Yamazaki, 1990; Palmer, 1990). As Lau and Shen (1988) have demonstrated using a simple coupled model, the unstable mode under the tropical air-sea coupling may be relevant during the growth phase of ENSO. Then one-way forcing from the ocean to the atmosphere, different from the two-way interaction in the real climate system, can also distort the atmospheric general circulation where this coupling is strong with SST > 28°C.

The simulated meridional wind stress is much weaker than the observed. For the coupled ocean–atmosphere GCM, it is of course necessary for the atmospheric GCM to be able to respond well in the zonal as well as the meridional wind stresses. But of great importance is the zonal wind stress. The complex EOF analysis of the surface zonal and meridional wind by Barnett (1983) reveals that the leading mode of the meridional wind has maxima late in the El Niño events. Figure 18a also suggests that the meridional wind anomaly is a consequence of the eastward propagating mode. Thus the smaller response of the meridional wind stress may not be of serious disadvantage for this atmospheric model to be used in the coupled model, although efforts should be done to remedy this error.

Acknowledgments

The author is grateful to T. Tokioka of Meteorological Research Institute for encouragement and discussion throughout this work and to K. Kodera for discussion. This research was a part of "Japanese Experiment on Asian Monsoon (JEXAM)" supported by Science and Technology Agency. Computations are made with HITAC S810 at MRI.

References

Alexander, R. C. and R. L. Mobley, 1976: Monthly average sea surface temperature and ice pack limits for 1 deg global grid. *Mon. Wea. Rev.*, **104**, 143-148.

Arakawa, A. and W. H. Schubert, 1974: Interactions of a cumulus cloud ensemble with the large-scale environment. Part I. *J. Atmos. Sci.*, **31**, 674-701.

Barnett, T. P., 1983: Interaction of the monsoon and Pacific trade wind system at interannual time scales. Part I: The equatorial zone. *Mon. Wea. Rev.*, **111**, 756-773.

Goldenberg, S. B. and J. J. O'Brien, 1981: Time and soace variability of tropical Pacific wind stress. *Mon. Wea. Rev.*, **109**, 1190-1207.

Graham, N. E., T. P. Barnett, R. M. Chervin, M. E. Schlesinger and U. Schlese, 1989: Comparison of GCM and observed surface wind fields over the tropical Indian and Pacific Oceans. *J. Atmos. Sci.*, **46**, 760-788.

Keen, R. A., 1982: The role of cross-equatorial tropical cyclone pairs in the Southern Oscillation. *Mon. Wea. Rev.*, **110**, 1405-1416.

Kitoh, A., 1988: Correlation between the surface air temperature over Japan and the global sea surface temperature. *J. Meteor. Soc. Japan,* **66**, 967-986.

Kitoh, A. and K. Yamazaki, 1990: Impact of surface drag of islands in the maritime continent on the atmosphere. A paper presented at the International TOGA Scientific Conference, 16-20 July 1990, Honolulu.

Latif, M., J. Biercamp, H. von Storch, M. J. McPhaden and E. Kirk, 1990: Simulation of ENSO related surface wind anomalies with an atmospheric GCM forced by observed SST. *J. Climate,* **3**, 509-521.

Lau, K.-M. and S. Shen, 1988: On the dynamics of intraseasonal oscillations and ENSO. *J. Atmos. Sci.*, **45**, 1781-1797.

Lau, N.-C., 1985: Modeling the seasonal dependence of the atmospheric response to observed El Ninos in 1962–76. *Mon. Wea. Rev.*, **113**, 1970-1996.

Lau, N.-C., 1988: Modeling of ENSO phenomena ay GFDL. *Japan-U.S. Workshop on the El Nino Southern Oscillation Phenomenon. (University of Tokyo, November 3-7, 1987) Meteor. Res. Rep.*, **88-1**, Division of Meteorology, Geophysical Institute, University of Tokyo, 160-168.

Luther, D., D. Harrison and R. Knox, 1983: Zonal winds in the central equatorial Pacific and El Niño. *Science,* **222**, 327-330.

Matthews, E., 1983: Global vegetation and land use: new high resolution data bases for climatic studies. *J. Clim. and App. Meteor.*, **22**, 474-487.

Nitta, Ts., 1989: Development of a twin cyclone and westerly bursts during the initial phase of the 1986–87 El Niño. *J. Meteor. Soc. Japan,* **67**, 677-681.

Nitta, Ts. and T. Motoki, 1987: Abrupt enhancement of convective activity and low-level westerly burst during the onset phase of the 1986–87 El Niño. *J. Meteor. Soc. Japan,* **65**, 497-506.

Palmer, T. N., 1990: Month to seasonal prediction of summer monsoon rainfall over Africa and India using high resolution NWP models. A paper presented at the International TOGA Scientific Conference, 16-20 July 1990, Honolulu.

Quiroz, R. S., 1983: The climate of the "El Nino" winter of 1982–1983 — A season of extraordinary climatic anomalies. *Mon. Wea. Rev.*, **111**, 1685-1706.

Rasmusson, E. M. and T. H. Carpenter, 1982: Variations in tropical sea surface temperature and surface wind fields associated with the Southern Oscillation/El Niño. *Mon. Wea. Rev.,* **110**, 354-384.

Storch, H. v., M. Latif and J. Biercamp, 1989: Simulation of the Southern Oscillation in an atmospheric general circulation model. *Phil. Trans. R. Soc. Lond.*, **A 329**, 179-188.

Tokioka, T., K. Yamazaki, I. Yagai and A. Kitoh, 1984: *A description of the Meteorological Research Institute atmospheric generl circulaton model (MRI·GCM-I).* Technical Report of the Meteorological Research Institute, No. 13, MRI, Tsukuba, 249 pp.

Tokioka, T., K. Yamazaki and A. Kitoh, 1986: *Mean statistics of the tropospheric MRI·GCM-I based on 12-year integration.* Technical Report of the Meteorological Research Institute, No. 20, MRI, Tsukuba, 314 pp.

Tokioka, T., K. Yamazaki, A. Kitoh and T. Ose, 1988: The equatorial 30-60 day oscillation and the Arakawa-Schubert penetrative cumulus parameterization. *J. Meteor. Soc. Japan,* **66**, 883-901.

Wallace, J. M. and Q.-R. Jiang, 1987: On the observed structure of the interannual variability of the atmosphere/ocean climate system. *Atmospheric and Oceanic Variability.* Royal Meteor. Soc., H. Cattle (ed.), 17-43.

Yagai, I. and T. Tokioka, 1987: The effect of increased surface drag coefficient over the continents on January circulations. *Short- and Medium-Range Numerical Weather Prediction. (T. Matsuno, ed.) Special Volume of J. Meteor. Soc. Japan,* 409-419.

1970-1989年の観測された海面水温で強制した大気大循環モデルにおける熱帯大気の年々変動について

鬼頭昭雄
(気象研究所気候研究部)

１９６９年９月から１９９０年２月までの年々変化する観測された全球（南緯４０度ー北緯６０度）海面水温を境界条件として与えた気象研究所大気大循環モデルの20.5年積分の熱帯大気の年々変動について議論した。

エル・ニーニョ南方振動(ENSO)に関係した太平洋域の熱帯大気の年々変動はモデルで良く再現されている。観測・モデル双方において、インド洋から中部太平洋まで約１年半かけて東進するシグナルが赤道上の850 mb東西風に見られる。

熱帯太平洋上の風応力の季節変化及び年々変動の比較を行なった。主成分解析で得られたモデルの東西風応力アノマリーの第１・第２主成分は共にその空間構造・係数の時系列双方が観測と対応している。したがって２つのモードで表わされる東西風応力アノマリーの東進がモデルでも再現されている。しかしENSO発達段階における西部熱帯太平洋での東西風応力アノマリーがモデルでは観測より小さい。モデルで得られた南北風応力の季節変化・年々変動については、その空間構造・時間発展共に観測と対応するものの、赤道付近において特にその振幅が小さい。

Figure Legends

Fig. 1 Time-series of anomalies for (a) simulated zonal wind at 200 mb (m s^{-1}) averaged for 4°S–4°N, 180°–140°W, (b) simulated zonal wind at 850 mb (m s^{-1}) averaged for 4°S–4°N, 180°–140°W, (c) simulated precipitation (mm d^{-1}) averaged for 4°S–4°N, 180°–140°W, (d) simulated SOI using sea level pressure at 150°W, 18°S and 130°E, 10°S, and (e) sea surface temperature (°C) averaged for 4°S–4°N, 180°–140°W. Original monthly means are plotted by thin lines and 5-month running means are shown by thick lines.

Fig. 2 Simulated (solid line) and observed (dashed line) Southern Oscillation Index.

Fig. 3 Simulated (solid line) and observed (dashed line) zonal surface stress anomalies averaged for 4°S–4°N, 180°–140°W. Westerly is positive. Unit: 0.01 N m^{-2}.

Fig. 4 Lagged correlation map between SST anomalies at 4°S–4°N, 180°–140°W (SST index) and SST anomalies at the equator. The abscissa is longitude and the ordinate is lagged month. Contour interval is 0.2. Values greater than 0.4 are hatched and values less than −0.4 are dotted. Correlations are calculated using the 5-month running means.

Fig. 5 As in Fig. 4 except for the correlation between the SST index and (a) simulated zonal wind anomalies at 200 mb, (b) simulated zonal wind anomalies at 850 mb and (c) simulated precipitation anomalies at the equator. Precipitation data has been smoothed by 9-point spatial smoother before calculation.

Fig. 6 As in Fig. 4 except for the correlation between the SST index and (a) observed zonal wind anomalies at 200 mb, (b) observed zonal wind anomalies at 850 mb and (c) observed OLR anomalies at the equator. Nine years' data (1979–1987) are used.

Fig. 7 Longitude-time sections of the SST anomalies at the equator. Contour interval is 0.5°C. Negative values are hatched.

Fig. 8 Longitude-time sections of the simulated precipitation anomalies at the equator. Contour interval is 1 mm d^{-1}. Negative values are hatched.

Fig. 9 Longitude-time sections of the observed OLR anomalies at the equator. Contour interval

is 10 W m^{-2}. Positive values are hatched.

Fig. 10 Longitude-time sections of the simulated zonal wind stress anomalies at the equator. Contour interval is 0.01 N m^{-2}. Negative values are hatched.

Fig. 11 As in Fig. 10 except for the observation (FSU dataset).

Fig. 12 (a) Observed (FSU dataset) annual mean zonal wind stress. Contour interval is 0.02 N m^{-2}. Positive values (westerlies) are hatched. (b) Annual component of the observed zonal wind stress. Amplitude of the component is indicated by the length, and phase by the direction of a vector at each grid point; north, maximum on 1 January: east, maximum on 1 April, etc. A reference vector is shown in the figure. (c) As in (a) except for the GCM. (d) As in (b) except for the GCM.

Fig. 13 As in Fig. 12 except for the meridional wind stress.

Fig. 14 First (top) and second (bottom) EOF modes of the observed (FSU dataset) zonal wind stress anomalies and time-series of the corresponding coefficients. They explain 20.7% and 14.5% , respectively. Contour interval is 0.02 N m^{-2}. Negative values are hatched.

Fig. 15 Lagged correlations for the EOF coefficients of zonal wind stress (τ_x) between (a) C_1^{OBS} and C_2^{OBS} (solid line) and C_1^{GCM} and C_2^{GCM} (dashed line), (b) C_1^{OBS} and C_1^{GCM} (solid line) and C_2^{OBS} and C_2^{GCM} (dashed line).

Fig. 16 As in Fig. 14 except for the GCM. They explain 34.9% and 10.2% , respectively.

Fig. 17 Observed (top) and simulated (bottom) first EOF modes of the meridional wind stress anomalies and their coefficients.

Fig. 18 Lagged correlations between (a) $C_1(\tau_y)$ and $C_1(\tau_x)$ for the observation (solid line) and the GCM (dashed line), (b) $C_1^{OBS}(\tau_y)$ and $C_1^{GCM}(\tau_y)$.

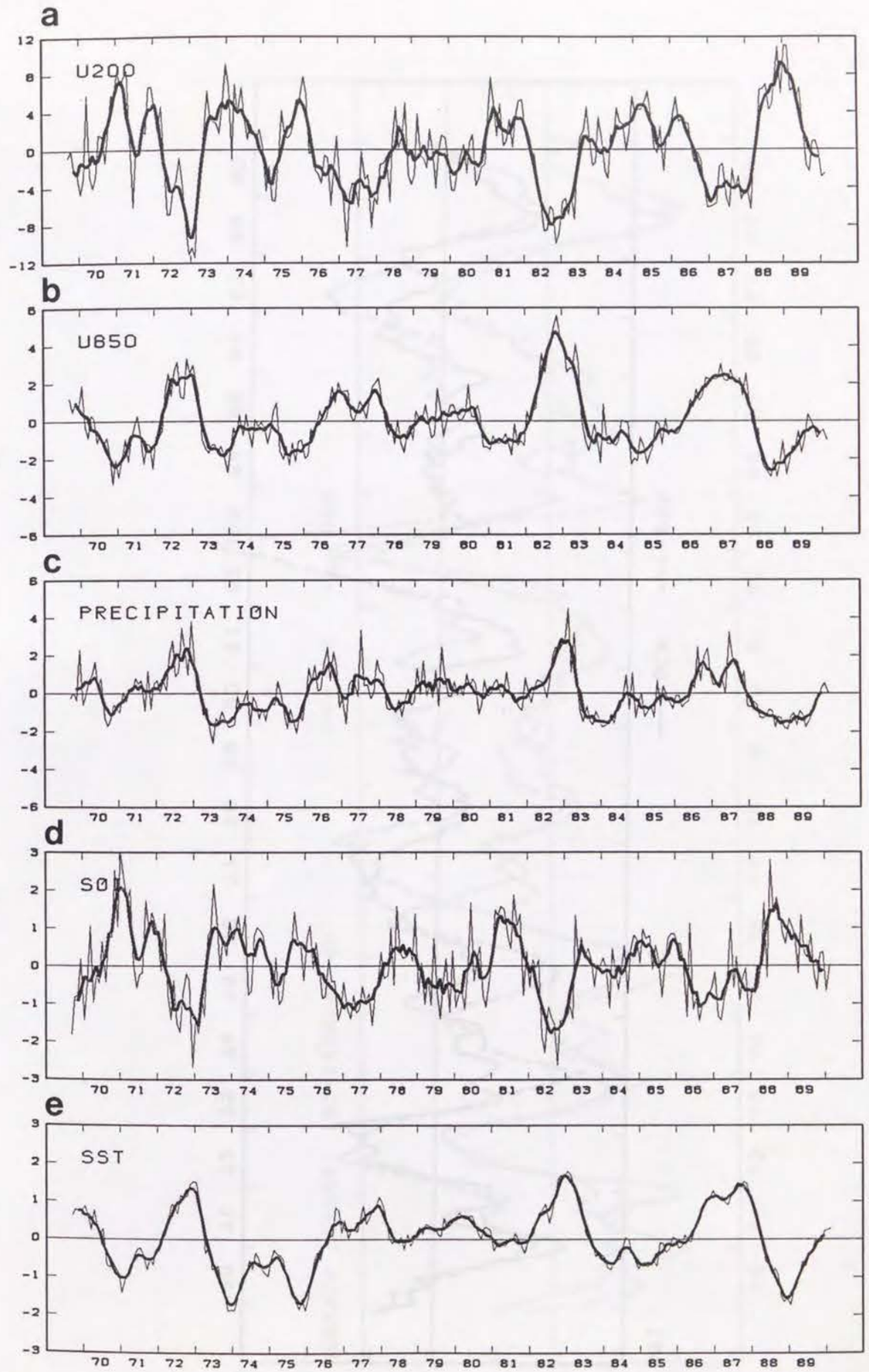

FIGURE 1

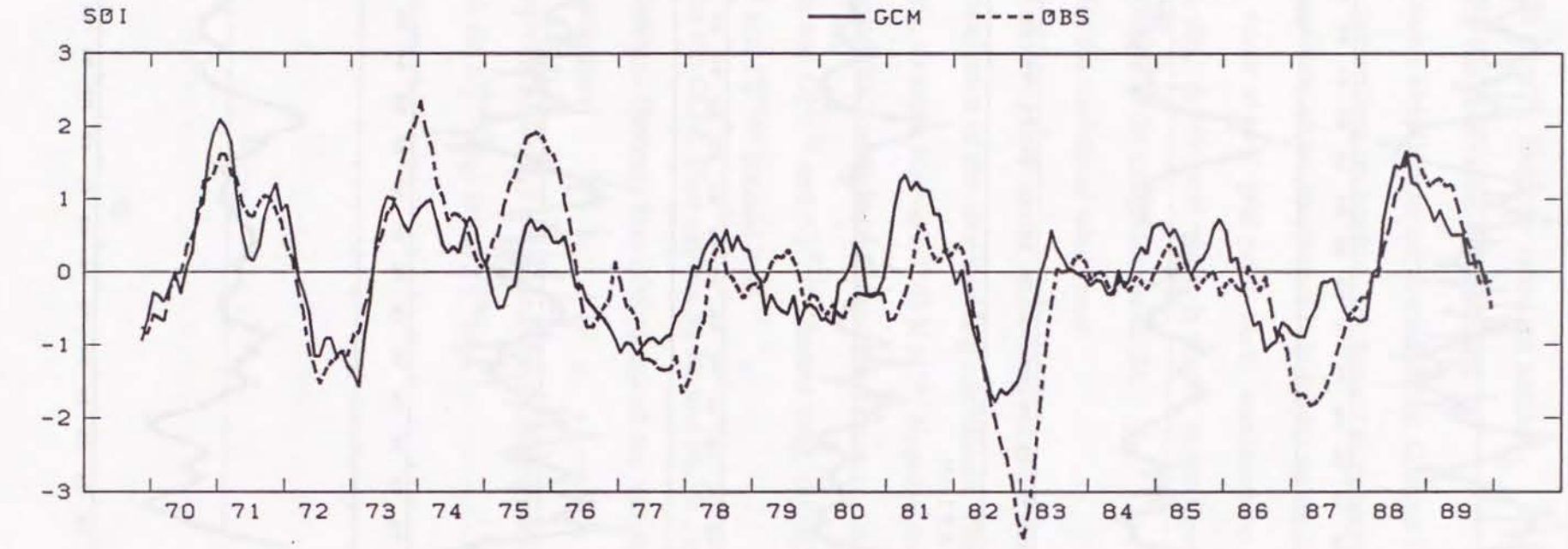

FIGURE 2

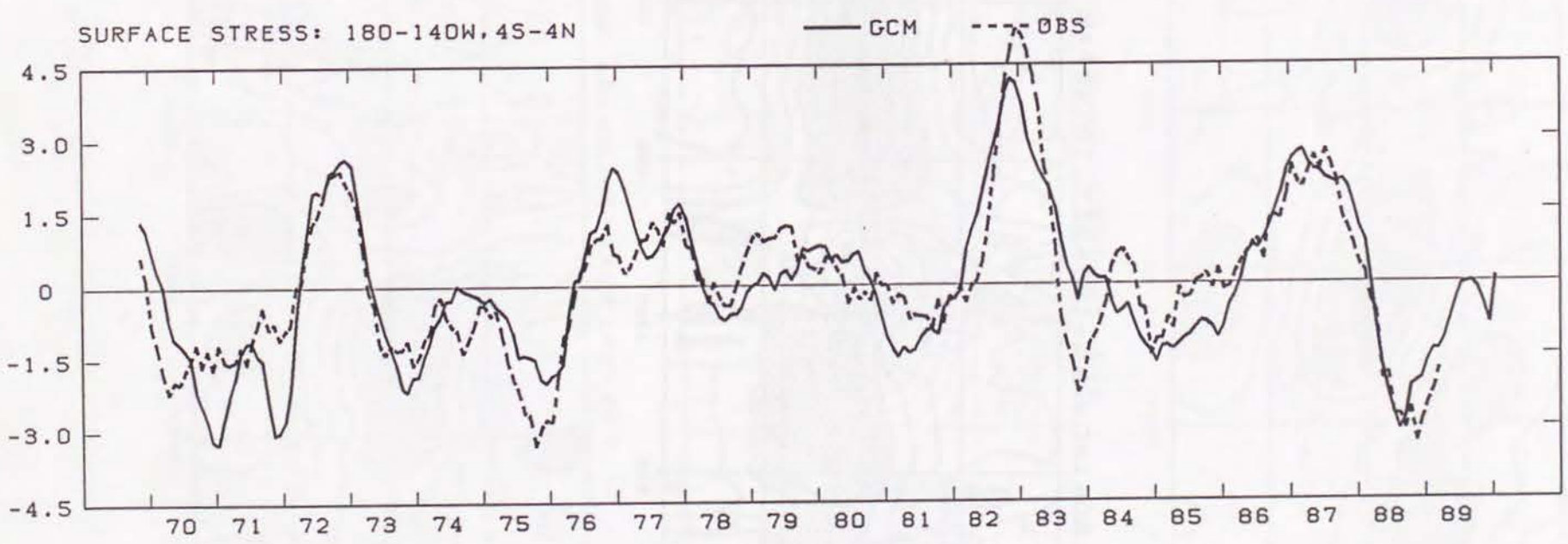

FIGURE 3

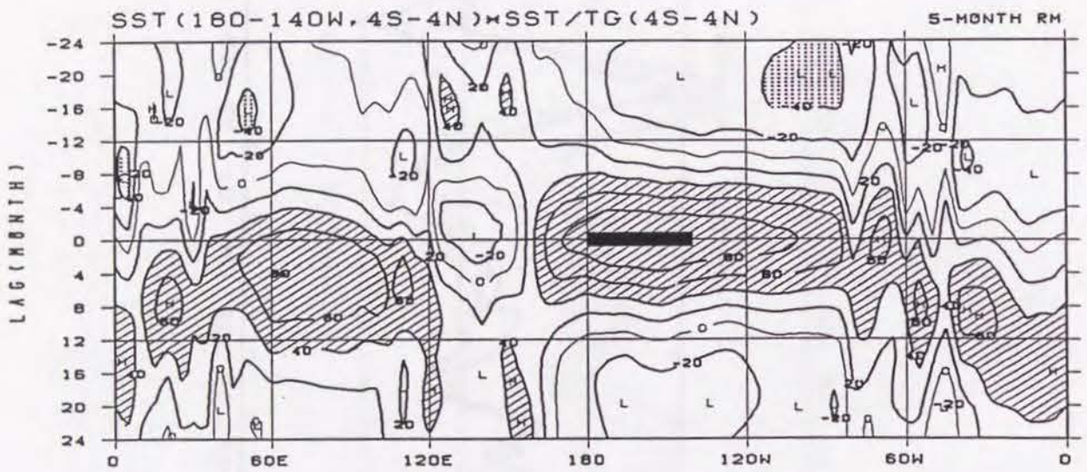

FIGURE 4

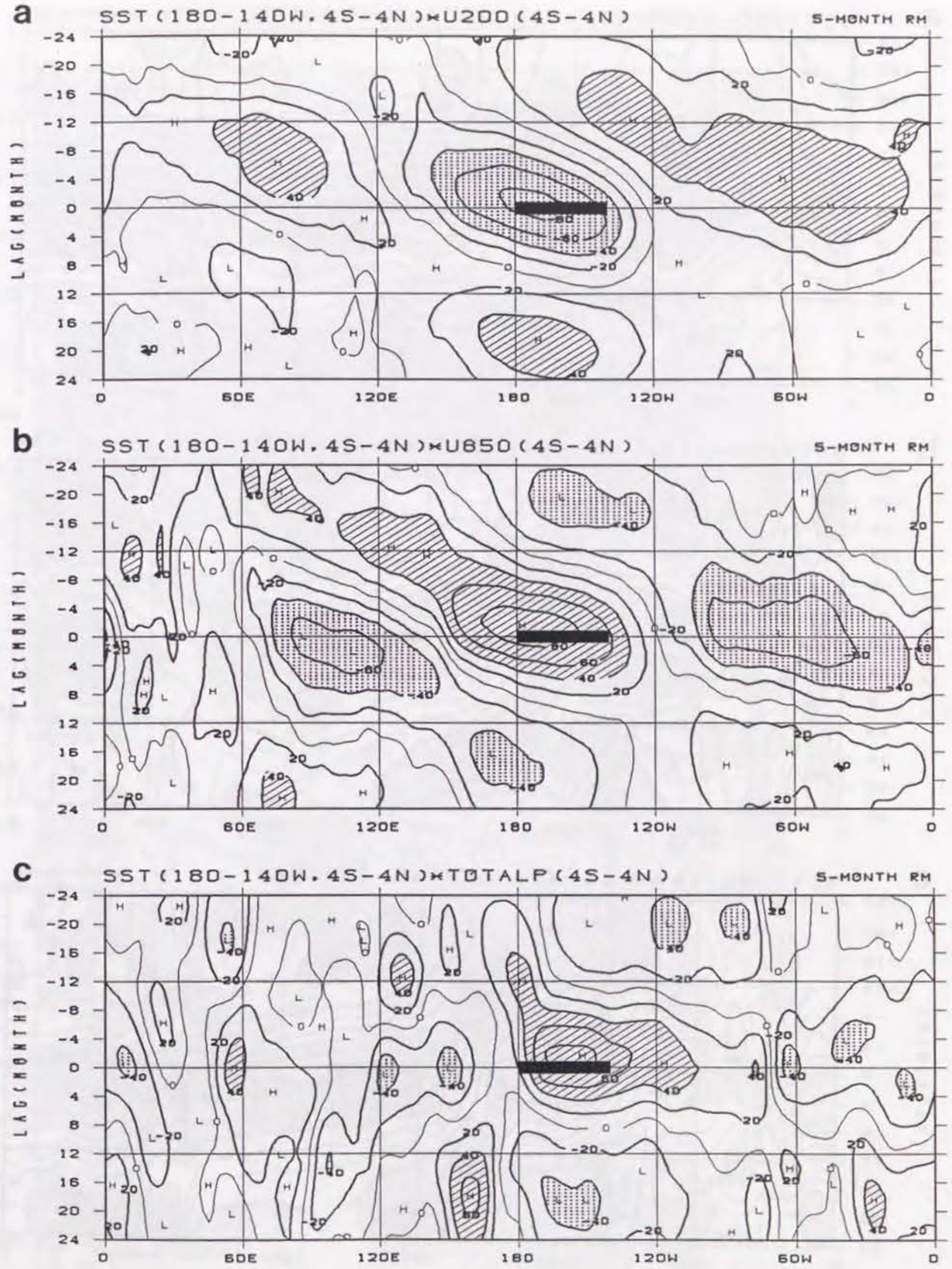

FIGURE 5

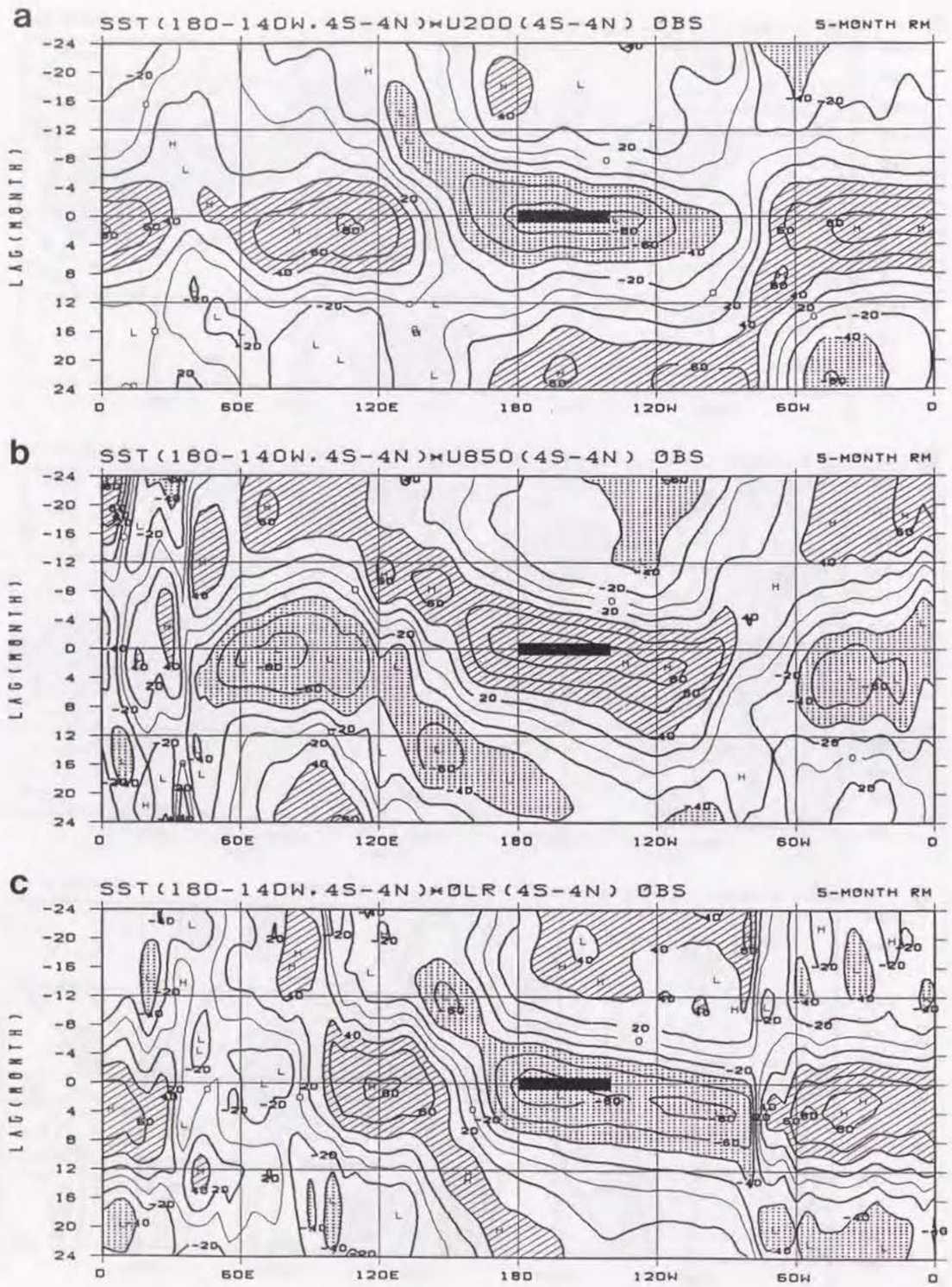

FIGURE 6

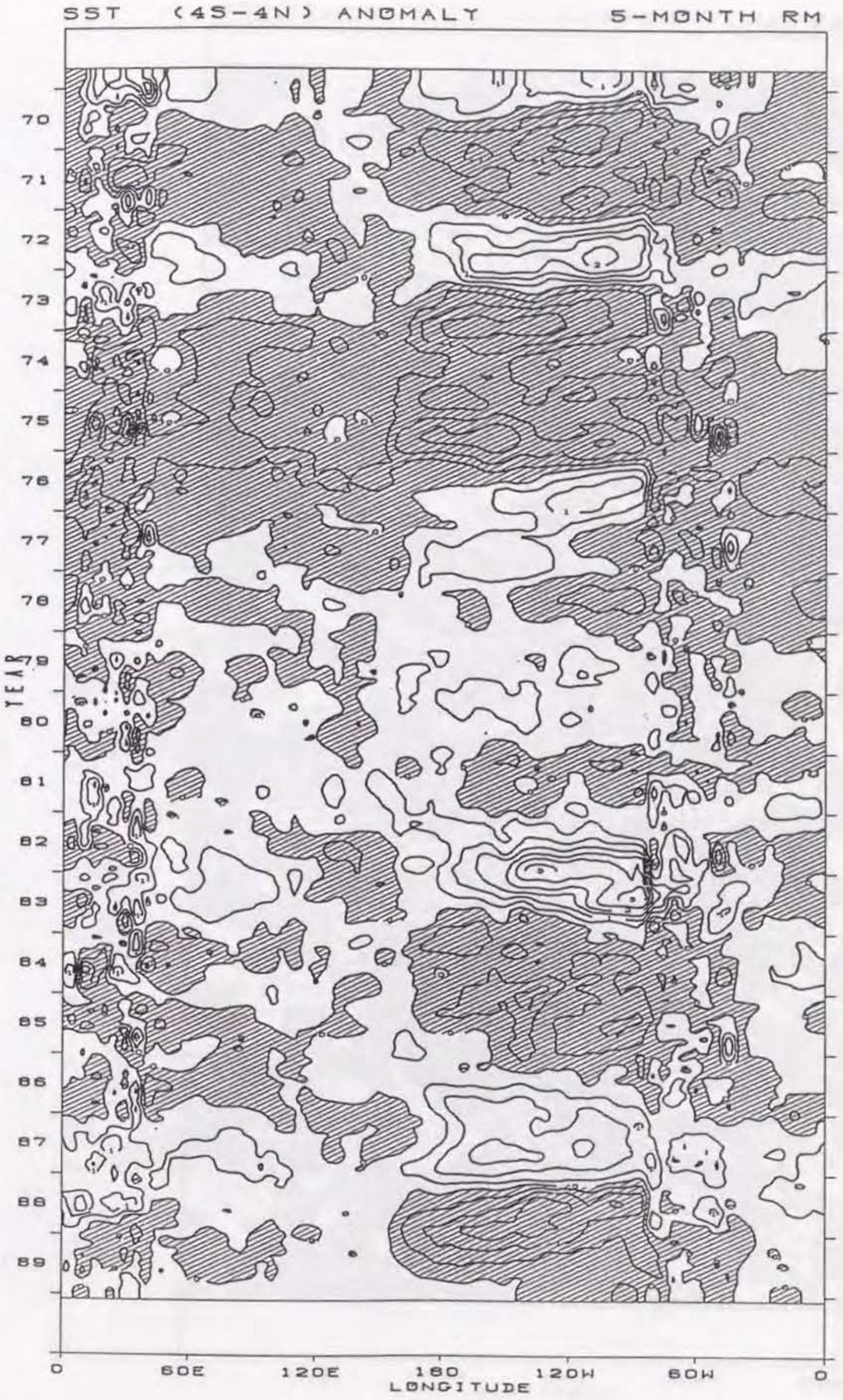

FIGURE 7

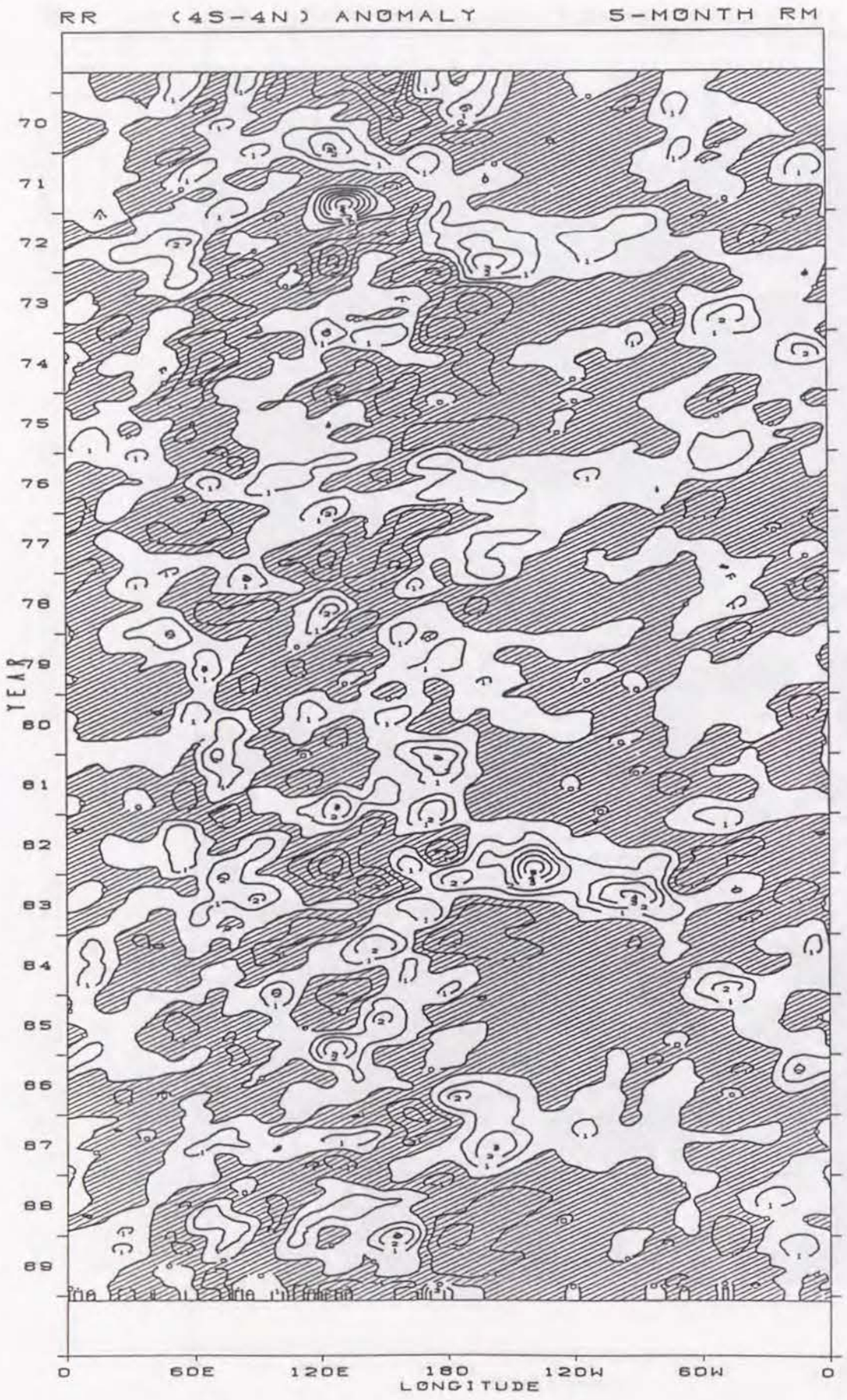

FIGURE 8

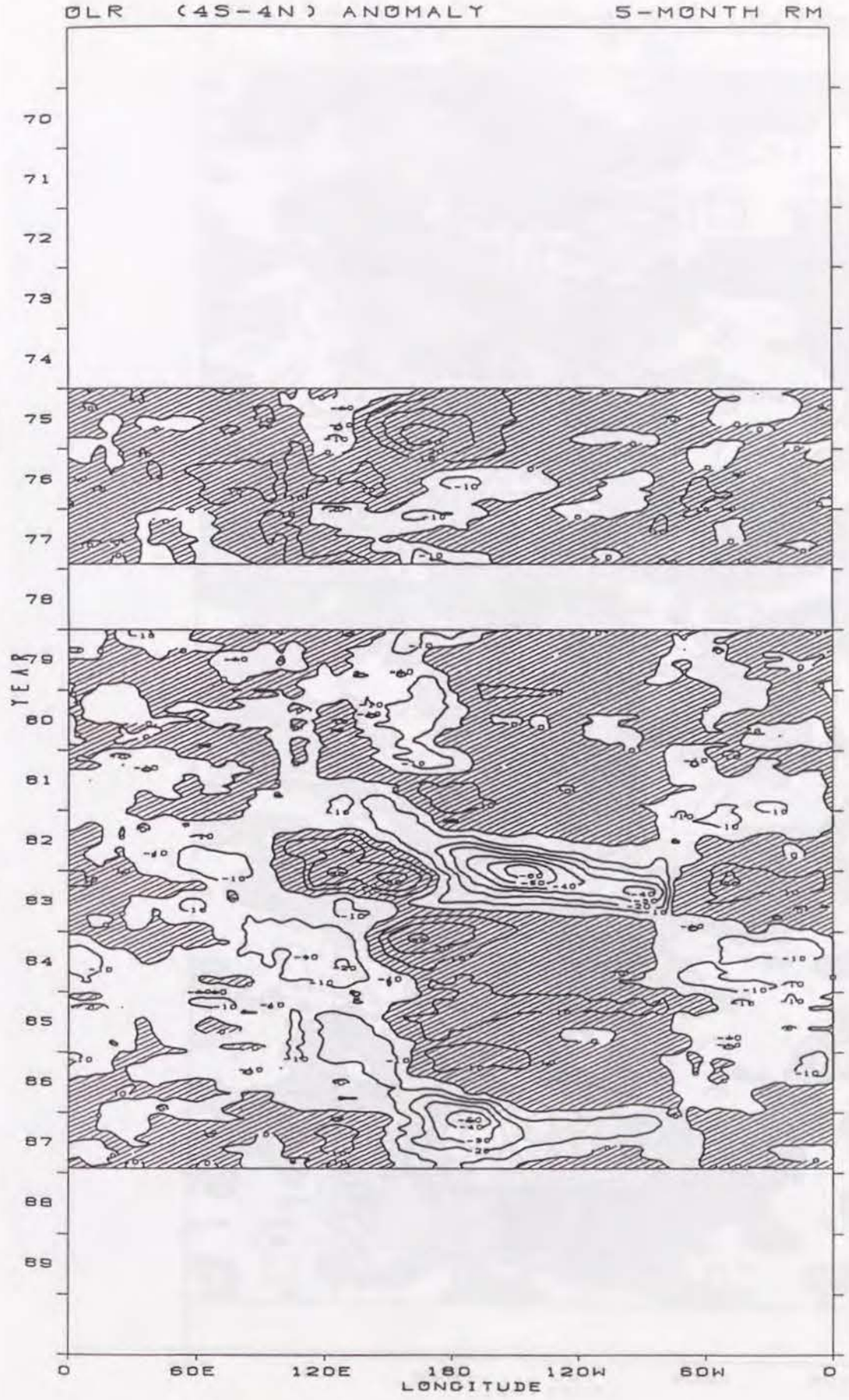

FIGURE 9

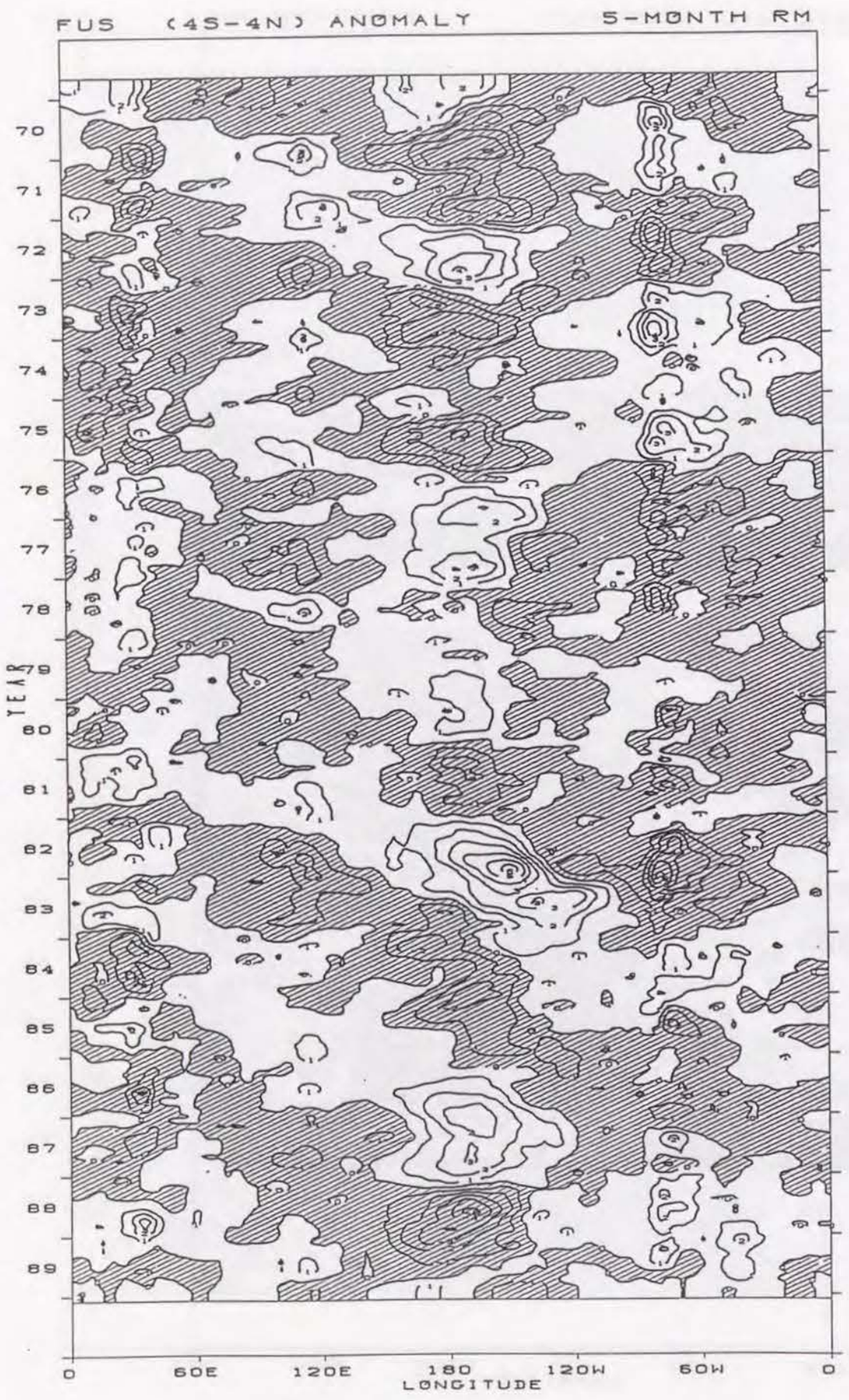

FIGURE 10

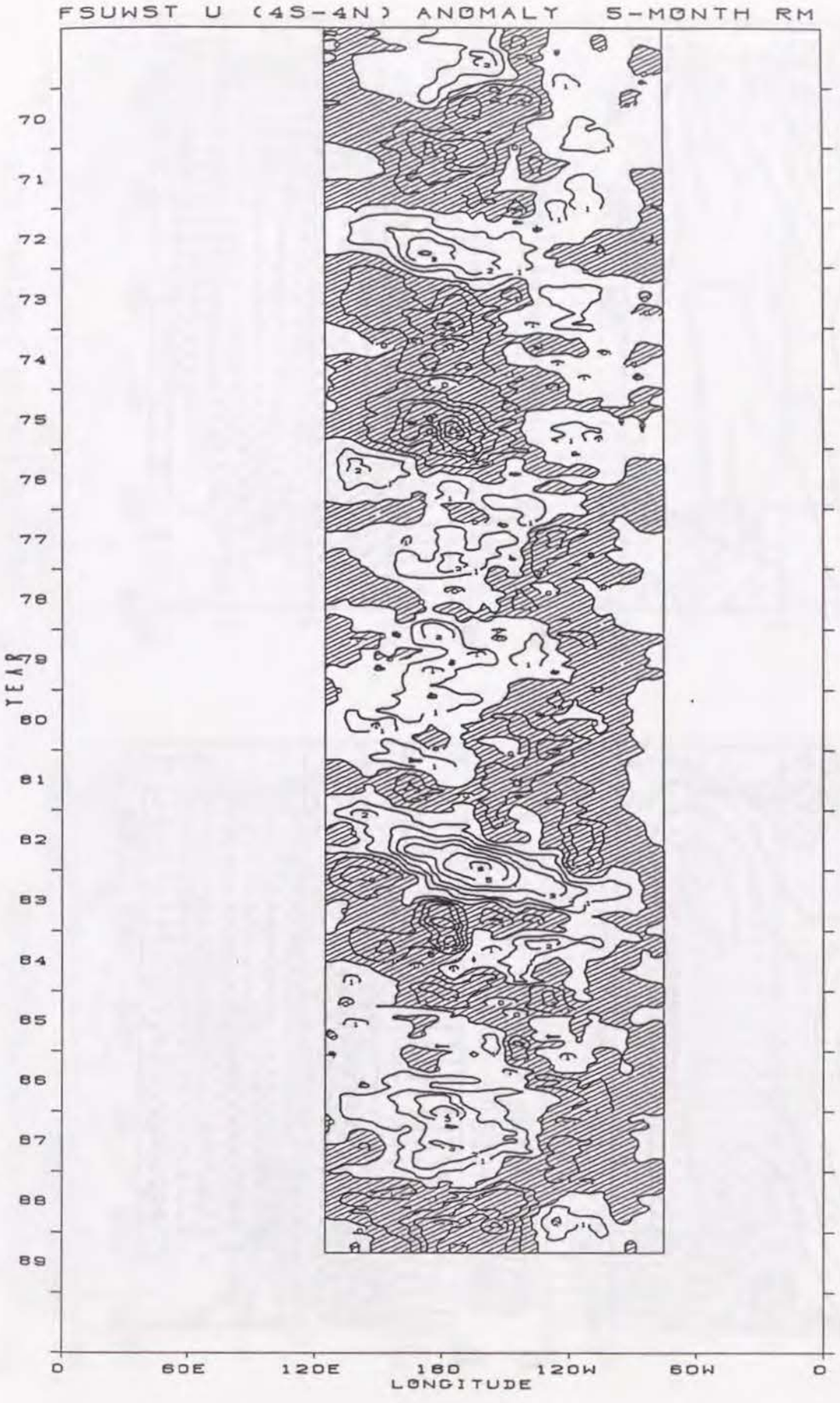

FIGURE 11

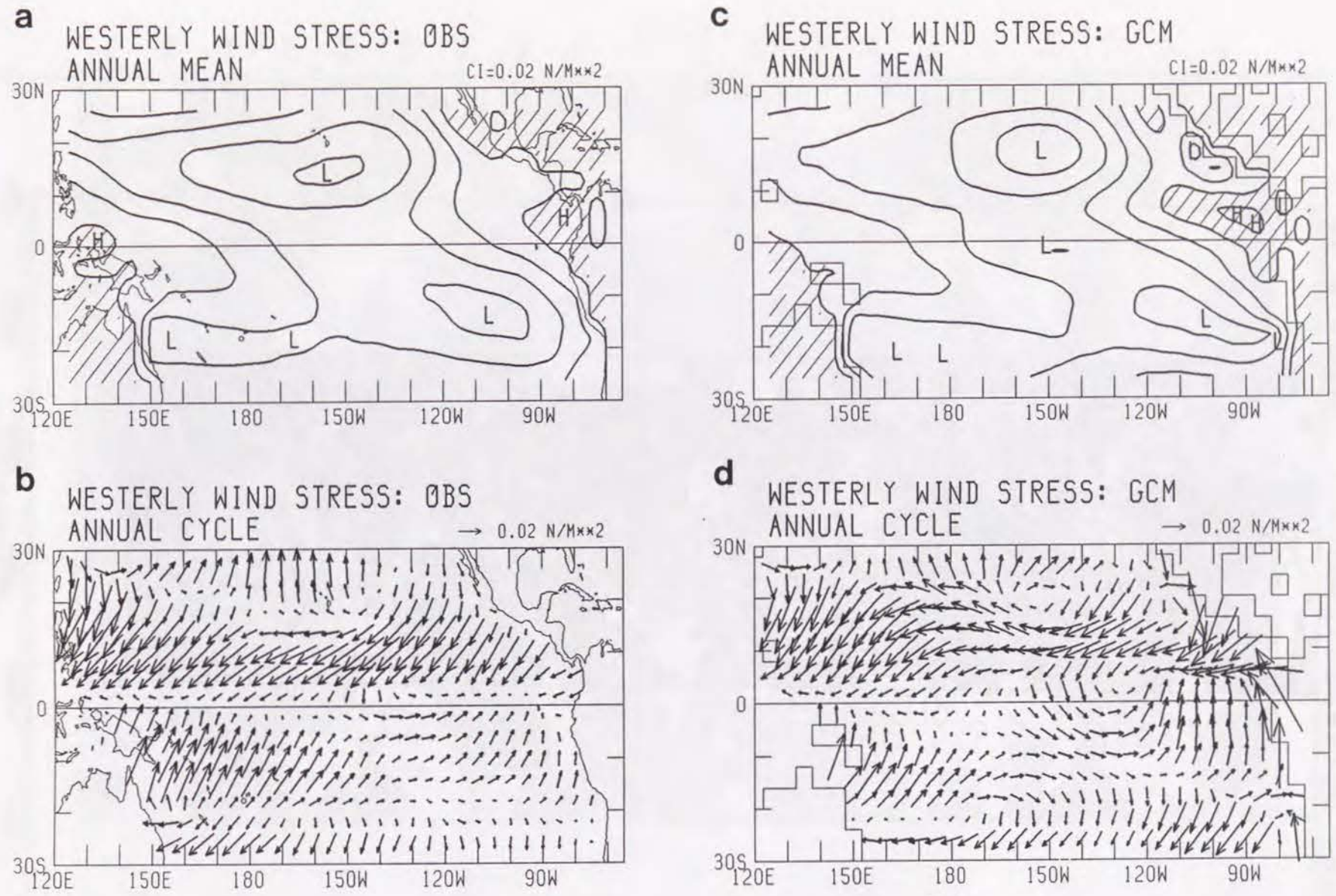

FIGURE 12

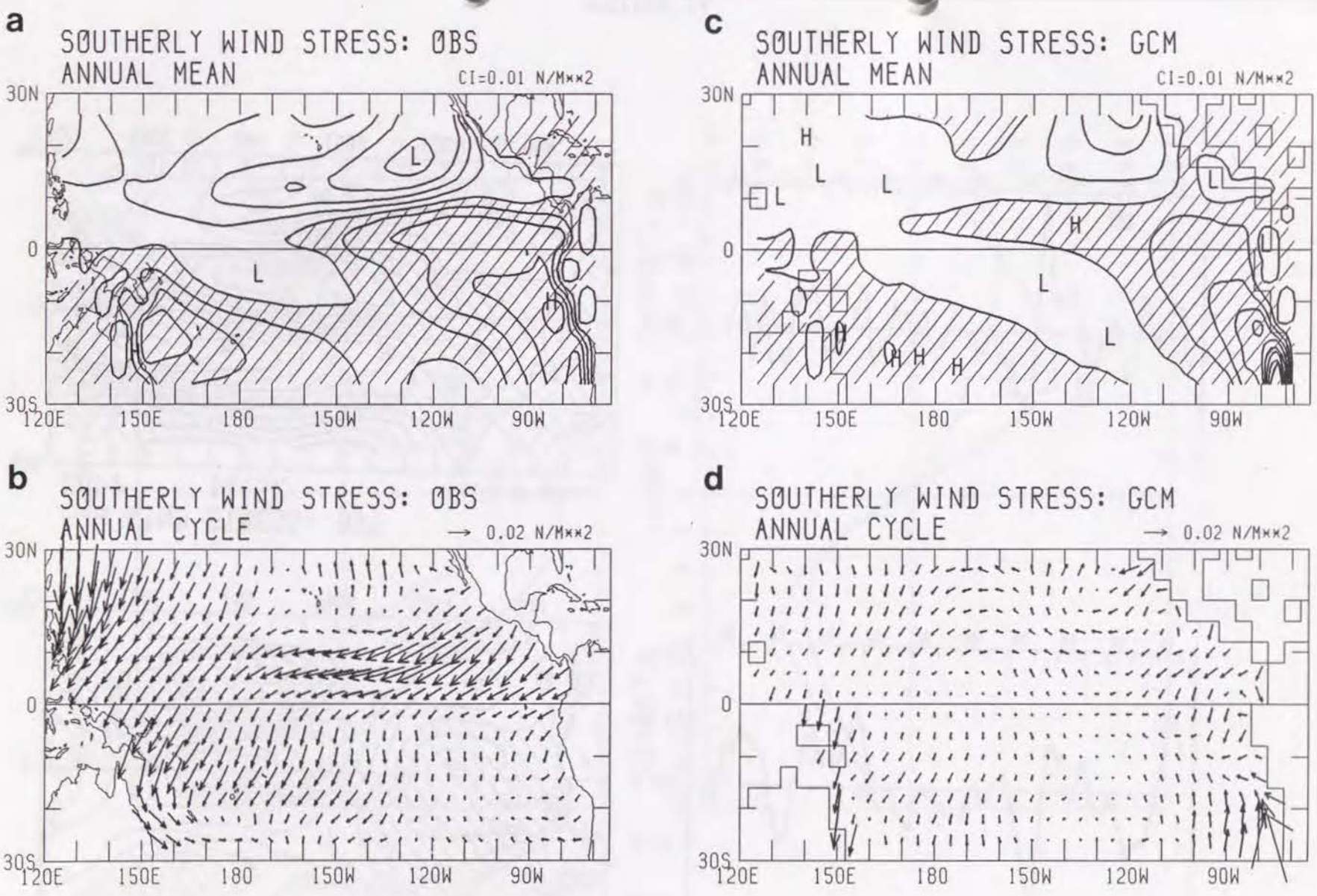

FIGURE 13

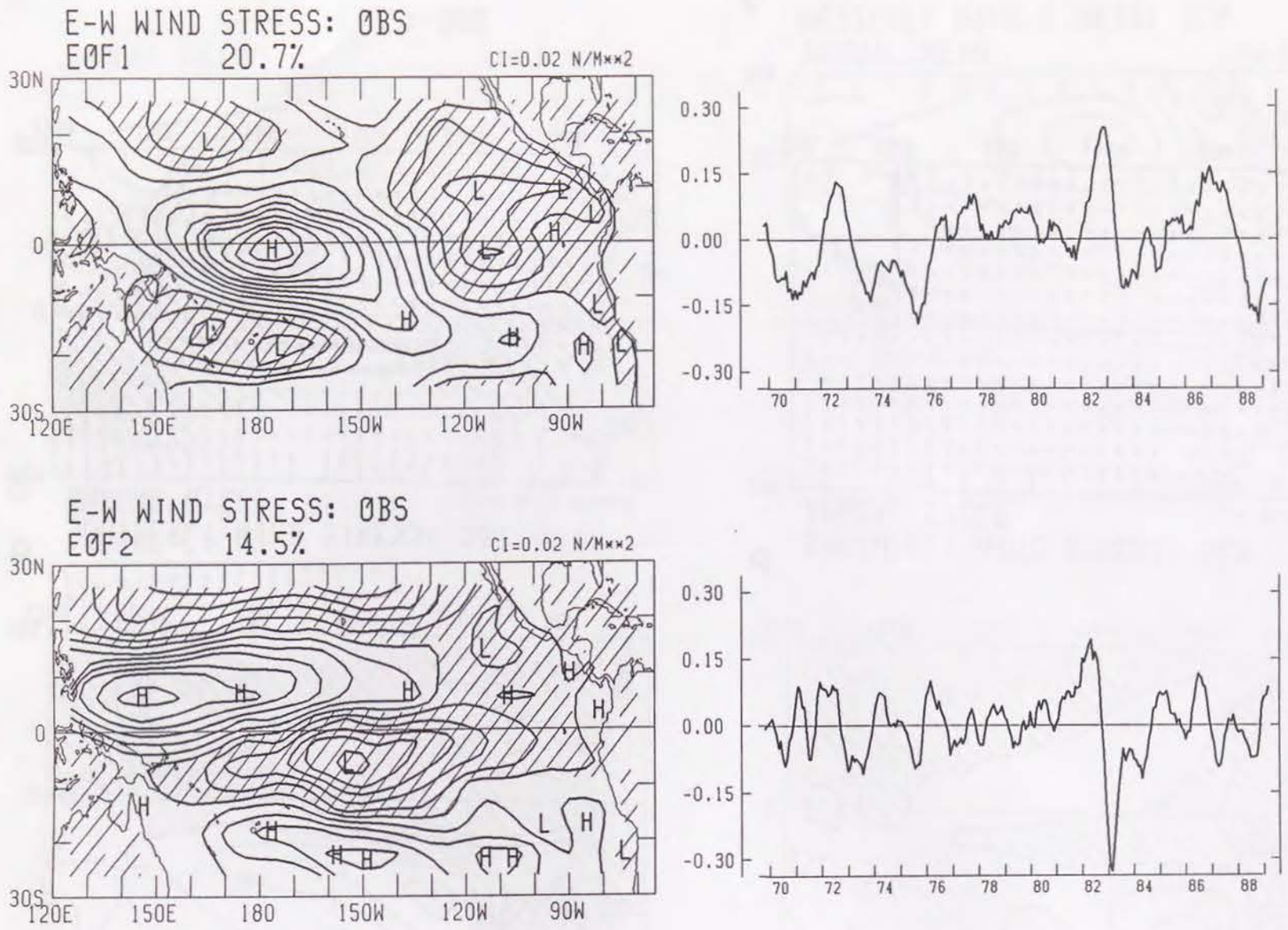

FIGURE 14

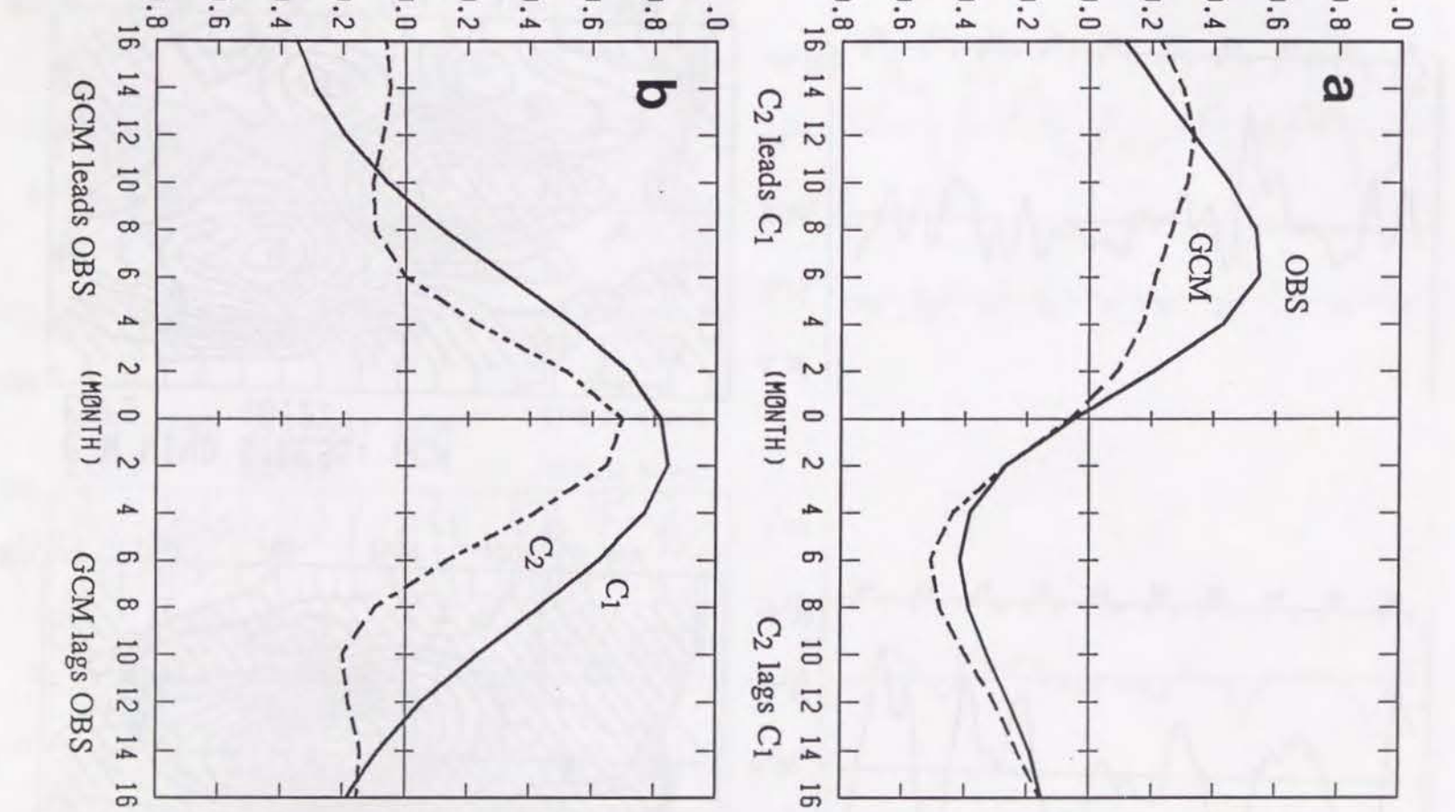

FIGURE 15

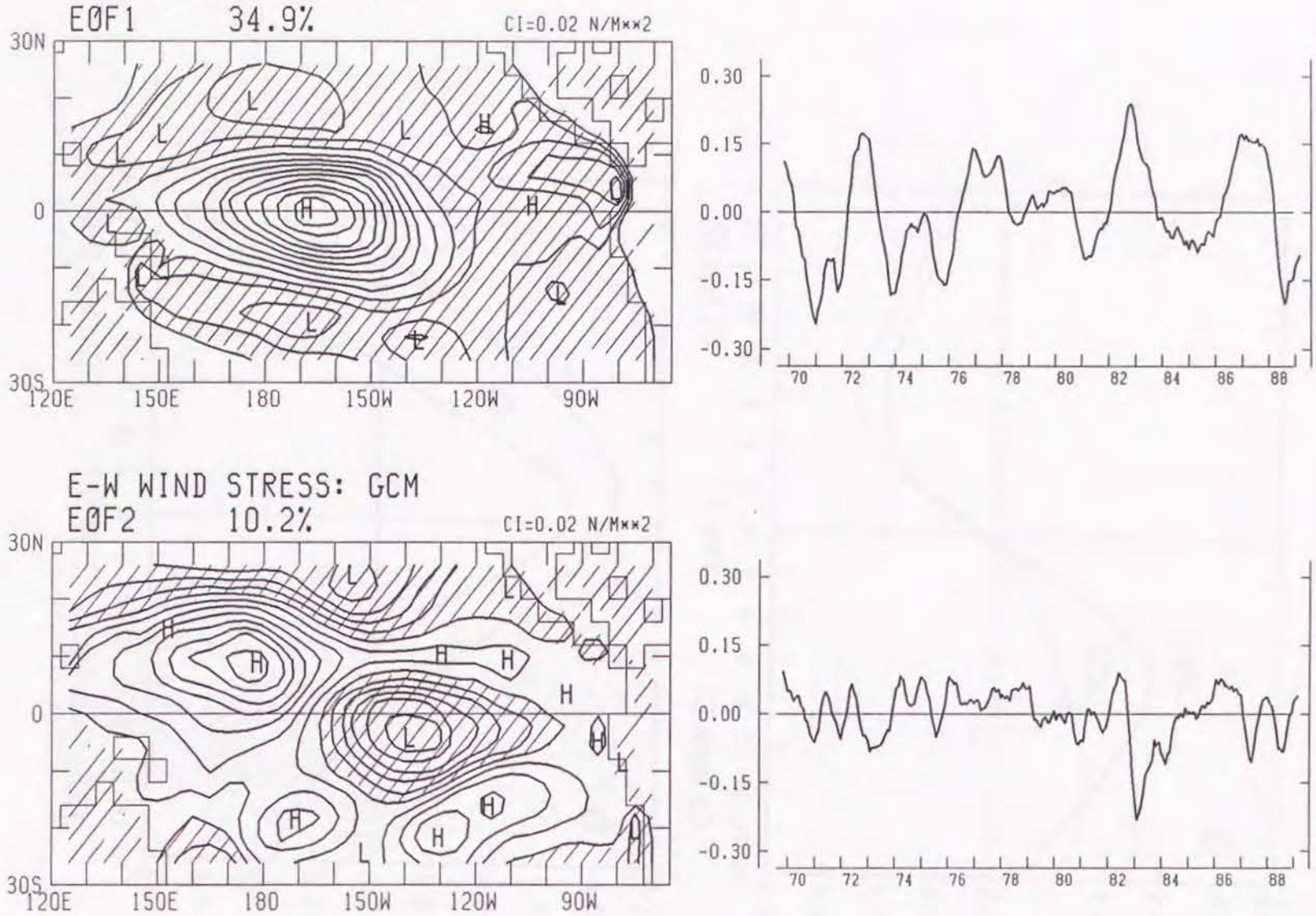

FIGURE 16

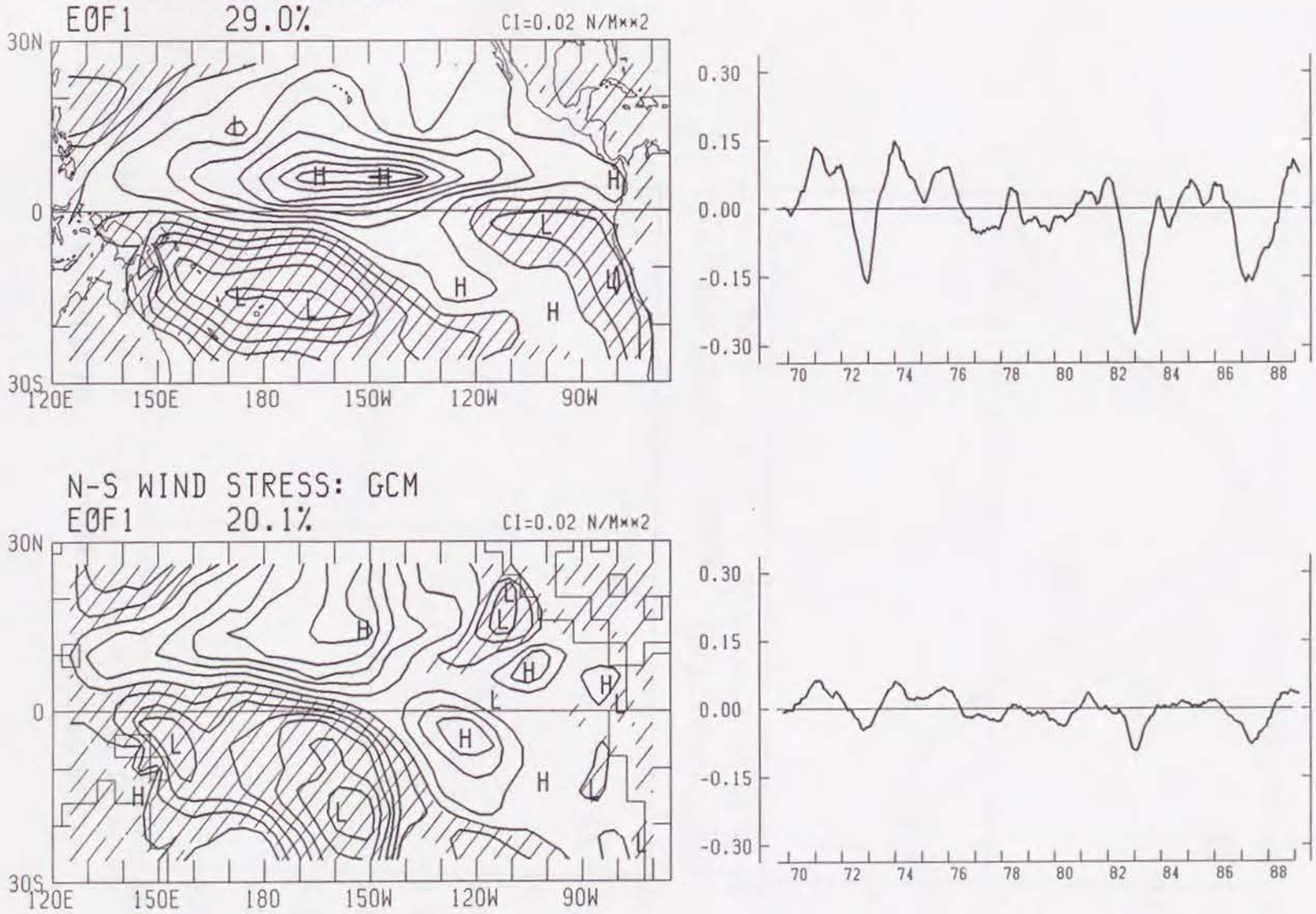

FIGURE 17

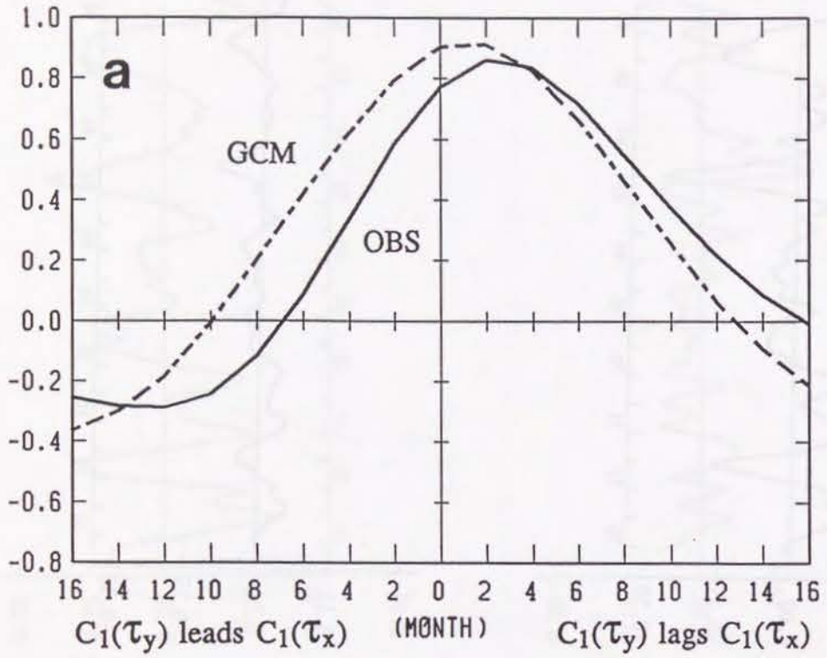

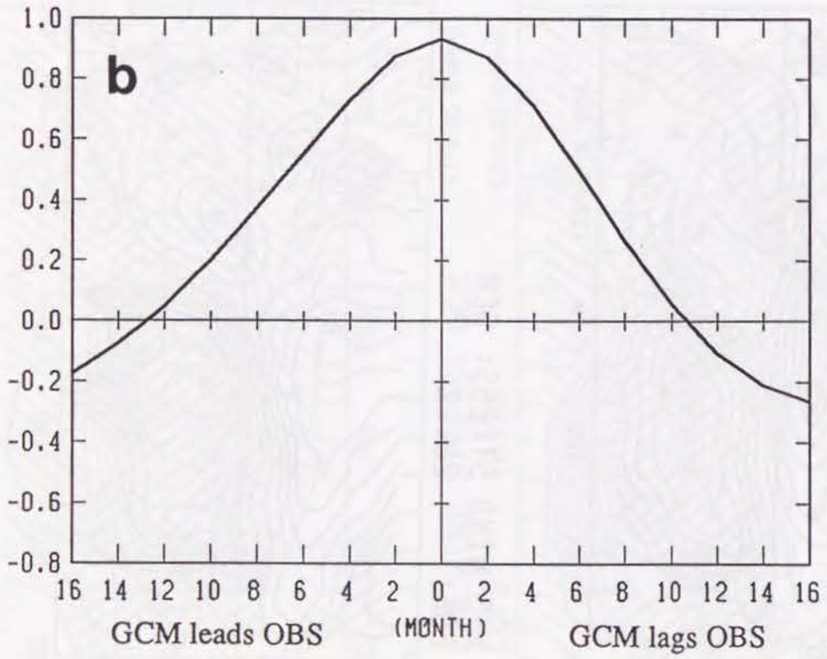

FIGURE 18

Low-Frequency Variability of the Wintertime Northern Hemisphere Extratropics in an Atmospheric GCM Forced by the 1970–1989 SST

By Akio Kitoh

Meteorological Research Institute, Tsukuba, Ibaraki 305, Japan

November 1990

Abstract

An atmospheric general circulation model is integrated forced by the observed near-global (40°S–60°N) sea surface temperatures (SST) from September 1969 to February 1990. Recurrent patterns of the monthly mean Northern Hemisphere atmosphere in the simulated 20 winters are identified and compared with the observation. The simulated first mode, in the zonal wind at 200 mb, geopotential height at 500 mb and zonal-mean zonal wind, has fluctuated with a time-scale of about 10 years. This decade scale variation seems to result from the specified SST for this period particularly over the tropical western Pacific northeast of New Guinea. Meridional shift of the East Asian subtropical jet and associated circulation changes contribute to this variation. Surface air temperature variations from around Japan to the extreme northern Pacific are mostly explained by this mode. This mode resembles the observed first *and* fourth modes of the geopotential height at 500 mb. The model's systematic error of emphasizing variability over the North Pacific than that over the North Atlantic results in extracting this mode associated with the meridional shift of the East Asian jet as the leading mode. Additionally, a trend of the equatorward shift of the Southern Hemisphere subtropical jet is also simulated related to the trend in the SST.

1. Introduction

Atmospheric temporal variability and teleconnections with time scales of a week to season have attracted much attention in the meteorological community and there are many literature on these subjects (*e.g.,* Wallace and Gutzler, 1981). Teleconnection study between the tropics and the extratropics with emphasis on the El Niño/Southern Oscillation (ENSO) is pioneered by Bjerknes (1969) and is followed by Horel and Wallace (1981) and van Loon and Rogers (1981) among others. There are also many general circulation model (GCM) studies investigating atmospheric responses to the sea surface temperature (SST) anomalies (*e.g.,* Nihoul, 1985; World Climate Programme, 1986).

There are some attempts to extract low-frequency recurrent modes such as observed by Wallace and Gutzler (1981) with a long integration of GCMs. Lau (1981) discusses recurrent anomalies in a 15-year simulation with a 9-level spectral R15 (rhomboidal truncation at 15 wavenumbers) GCM at the Geophysical Fluid Dynamics Laboratory (GFDL). The GCM was integrated with the climatological (only the seasonal cycle is included) SSTs (Manabe and Hahn, 1981). He finds that the most preferred simulated mode of oscillation is similar to that observed in the real atmosphere. Volmer *et al.*(1983, 1984) also analyze the 500 mb height field in a long integration with a 15-level T21 (triangular truncation up to zonal and meridional wavenumber 21) GCM at the European Centre for Medium Range Weather Forecasts (ECMWF).

Modeling the atmospheric variability using observed evolving SST is the logical next step. Lau (1985) forces the GFDL GCM with the tropical Pacific observed SST for the period 1962–1976 and has assessed the model capability to simulate meteorological features relevant to ENSO. Kang and Lau (1986) use this 15-year data to obtain 300 mb eddy stream function variability which is similar to the observed over the North Pacific to North American sector and is highly correlated with the tropical Pacific SST. They have also obtained a mode which is linked to a characteristic structure of the zonal-mean zonal wind. Palmer (1987, 1988) has

synthesized the GCM efforts to simulate low frequency variability of the atmosphere.

Lau (1988), Graham *et al.*(1989), Storch *et al.*(1989) and Latif *et al.*(1990), and Kitoh (1990) have extended investigations with the *near-global* SST with the GFDL R15 GCM, the National Center for Atmospheric Research Community Climate Model (NCAR CCM0), the ECMWF T21 GCM and the Meteorological Research Institute (MRI) grid point model with 4° by 5° resolution, respectively, and examined the atmospheric variability in the tropics with respect to ENSO. Model responses to the SST anomalies associated with ENSO generally resemble the observed. Kitoh (1990) shows that the MRI·GCM reproduces the observed eastward migration of the surface zonal wind stress anomalies over the tropical Pacific when forced with the 1970–1989 SST. Lau and Nath (1990) have analyzed the 30 year model data simulated by the GFDL GCM with the 1950–1979 SST. They find a close relationship between the principal modes of variability in the Northern Hemisphere winter and the middle latitude SST. Over the Pacific, the east-west SST seesaw between northwest of Hawaii and the west coast of North America is strongly correlated with the atmospheric Pacific/North American (PNA) pattern in agreement with the observational study by Wallace and Jiang (1987).

In this paper, we extract recurrent modes of the monthly mean zonal wind and the Northern Hemisphere geopotential height at 500 mb in 20 winters simulated with the MRI GCM through the empirical orthogonal function (EOF) analysis (section 4). The simulated recurrent modes have counterparts in the observed ones, but the ordering is different. This is related to the model's systematic error (section 3). Due to the error of having relatively larger variance over the North Pacific than over the North Atlantic, the model tends to show variability over the North Pacific more clearly. The simulated most recurrent mode is related to the meridional shift of the East Asian subtropical jet and shows the decade scale fluctuation (section 5). This mode also appears in the model run without year-to-year SST variations and is thus inherent in the model atmosphere. However its appearance seems to be influenced by the prescribed SST variations.

2. The model and the data

a. The model

The model (MRI·GCM) used for this study is a 5-level tropospheric atmospheric general circulation model with a horizontal resolution of 4° latitude and 5° longitude with a top at 100 mb. Physical processes included are the parameterized cumulus convection, planetary boundary layer (PBL) and radiation which is interactive with model-generated cloud. Ground hydrology parameterization predicts snow mass and ground soil moisture. Diurnal as well as seasonal variation of insolation is included. Details of this model (MRI·GCM-I) are described in Tokioka *et al.*(1984).

Some modifications have been made to MRI·GCM-I. The Arakawa and Schubert (1974) penetrative cumulus parameterization scheme is modified to impose an additional constraint between the minimum entrainment rate and the depth of the predicted PBL layer (Tokioka *et al.*, 1988). We use the observed seasonally varying surface albedo over land compiled by Matthews (1983). Surface albedo over the snow is now a function of snow depth and the terrain height dependent masking depth. For the ground hydrology parameterization, the model uses a one-layer bucket model, in which field capacity is a function of latitude with a large value in the tropics (15 g cm^{-2} at the equator) and a small value in high latitudes (3 g cm^{-2} poleward of 60° latitude). This makes an improvement of summer surface air temperatures over the Eurasian continent where the original MRI·GCM-I has shown systematically cooler temperature in summer. The effect of sub-grid scale topography is incorporated by increasing surface drag coefficients over the continents as a function of the standard deviation of sub-grid scale topography after Yagai and Tokioka (1987).

b. The data

A 20.5 year integration has been performed with the prescribed SSTs from September 1969 to February 1990 over the worldwide oceans for 40°S–60°N. Monthly means for

December, January and February from 1970/71 to 1989/90 winters are used. The SST come from the Climate Analysis Center/NMC/NOAA before 1984 and from the Numerical Prediction Division/JMA after 1985. There may be some systematic differences between the two datasets due to different analysis method, but no adjustment is made in this study. Poleward of these latitudes we use the Alexander and Mobley (1976) climatological SST. A parallel 20-year integration which employs the globally climatological SST without year-to-year variations has also been performed. Limited comparison between the two integrations will be made in this paper, but detailed comparison between the two GCM datasets will be described in a separate paper.

Observed data used are the zonal wind at 200 mb for the 9-year period 1979–1987 analyzed by the NMC/NOAA and the geopotential height at 500 mb in the Northern Hemisphere for the period 1946–1989 compiled at the Long-range Forecast Division/JMA.

3. Means and standard deviations

a. Zonal wind at 200 mb

Figure 1a shows the winter (December-January-February) mean 200 mb zonal wind in the 20-year simulation. This can be compared with the observation based on the 9-year climatology (Fig. 1c). In the Northern Hemisphere middle latitudes, the subtropical jets are simulated with their maxima around Japan and the eastern coast of North America, corresponding to the observation. The East Asian subtropical jet extends from North Africa through south of Himalaya and East Asia to the North Pacific. The strength of the jet is similar to the observed. However the simulated jet axis extends east-north-east in the jet exit region and is located far northward than the observed in the northeastern Pacific. Close inspection of the East Asian jet center reveals a slight ($< 4°$ latitude) northward shift in the GCM. The Atlantic subtropical jet in the GCM is about 10 m s^{-1} stronger than the observed along with the stronger tropical easterlies over South America. This may be related to heavier precipitation over Central America in the GCM. In the tropics, other two easterly regions are well simulated over Africa and over the maritime continent. A westerly duct in the central equatorial Pacific is also seen in the GCM, but there is a difference in a westerly duct in the Atlantic between the GCM and the observed. In the Southern Hemisphere, a single jet is properly simulated at 40°–50°S together with its zonal asymmetry (strong in the Atlantic/Indian Ocean and weak in the Pacific) (Kitoh *et al.*, 1990).

Simulated and observed standard deviations of monthly mean zonal wind at 200 mb for December, January and February are shown in Fig. 1b and 1d, respectively. Climatology for each month are subtracted from the original monthly means for each dataset to remove the seasonal variation before calculating the standard deviations.

Standard deviations of the observed 200 mb zonal wind (Fig. 1d) are large at the entrance and exit regions of the East Asian subtropical jet. It is also large at the Atlantic jet exit. The largest variability for the East Asian jet roughly coincides with the jet core, suggesting

that the intensification or weakening of the jet on the location is dominant in its fluctuations. They are accompanied by an eastward expansion into or contraction of the jet core away from the central Pacific (Lau and Boyle, 1987). On the other hand, over the Atlantic jet exit region, the variability is large to the north and to the south of the jet core, indicating the meridional shift of the jet. Variability is also large over the central Pacific and the Atlantic on the equator directly related to ENSO.

The simulated variability of the monthly mean 200 mb zonal wind in winter is large over the exit regions of the East Asian and the Atlantic jets, over the East Asian jet entrance region (North Africa to the Middle East) and over the central equatorial Pacific. Although the latter two are quite similar to the observed, the variability with respect to the East Asian subtropical jet is different. The simulated jet tends to show a meridional shift rather than the in situ intensification as observed.

The distribution of the ratio of the 200 mb zonal wind standard deviations (that of Fig. 1b divided by that of Fig. 1d) is shown in Fig. 2a. The simulated variability is generally smaller than the observed both in the tropics and in the extratropics. In the Northern Hemisphere extratropics the GCM has only 80% magnitude of standard deviations of the observed. Larger variability in the GCM than in the observed is found only over the northern and the southern flanks of the East Asian jet entrance and exit regions where the GCM shows large meridional shift of the jet core, and over Central America where the simulated zonal wind has large meridional shear (Fig. 1a and 1c).

Lau (1985) has shown by imposing observed tropical Pacific SSTs that the model atmosphere has 2–6 times variance over the tropics compared to that by using the climatological SSTs, while the same SST fluctuations are much less effective in enhancing the extratropical variability. A similar increase of variability is found in the present study when compared with a simulation with climatological SSTs (not shown). The point here is that even when we use the observed SSTs, the simulated variance is less than the observed. Smaller model variability is also reported by Lau and Nath (1990) with their 30-year GFDL GCM integrations.

They obtain 70–80% amplitudes of the observed standard deviation in the northern extratropics height field. The coarse horizontal resolution may have influenced the atmospheric variability through less baroclinic activity. Barotropic energy conversion would also be sensitive to the meridional resolution of the model. It may be that these resolution problems affect the atmospheric response to the SST anomalies. However an increase in model horizontal resolution would deteriorate many aspects of its climate and low frequency variability (Palmer, 1987) unless sub-grid scale effects of orography are parameterized. The vertical extent of the model domain will have also limited the variability of this model. The sub-grid scale parameterizations with respect to the PBL formulation and the penetrative cumulus convection might also limited the model response to the SSTs in the tropics (Graham *et al.*1989; Kitoh, 1990).

b. Geopotential height at 500 mb

Figure 3 shows the winter mean geopotential height at 500 mb and its monthly standard deviations for the GCM and for the observation. The stationary eddies are also compared. In the Northern Hemisphere middle latitudes, troughs over East Siberia to the northwestern Pacific and over eastern Canada along with ridges over the northeastern Pacific, over the eastern Atlantic and over the Urals are simulated. Amplitudes of troughs and ridges in the GCM are in good agreement with the observed, except over eastern Canada where the trough over the Hudson Bay is not well developed in the GCM. The observed stationary trough is −120 m deep over the Hudson Bay, while the GCM has a stationary low well south of the observed.

It has been known that the polar night jet structure influences the stationary planetary waves in the upper troposphere and lower stratosphere (Boville, 1984; Boville and Cheng, 1988). The model used here does not have a stratosphere, thus trapping all energy at the top of the model and influencing the stationary wave structure. Therefore the model systematic error in its stationary wave structure may be related to the model's vertical extent. But

this systematic error of the weaker trough over eastern Canada cannot be remedied simply including the stratosphere. In a version of the MRI·GCM which has a top at 1 mb, there are westerly biases in the stratosphere and tropospheric stationary eddies are even worse than with the tropospheric version. After introducing the gravity-wave drag parameterization, westerly biases are remedied and we get a reasonable stationary eddy field with a 500 mb trough near the Hudson Bay (Yagai, 1990, personal communication).

Nigam and Lindzen (1989), on the other hand, examine the sensitivity of orographically forced stationary waves to variations of basic flows with a high-resolution linear primitive equation model. They find a remarkable sensitivity to small latitudinal shift of the subtropical jet. Poleward displaced jet like a situation simulated here (compare Fig. 1a and 1c) would reduce poleward vertical wave propagation causing smaller high-latitudes stationary wave amplitudes.

Tokioka and Noda (1986) has investigated the orographic effects of the Rockies and Greenland under the perpetual January condition with the MRI·GCM-I for two situations: with and without the Asian mountains. In their experiment, a deep trough over the Hudson Bay which is very similar to the observed (Fig. 3e) is simulated downstream of the Rockies due to the orographic effect of the Rockies and Greenland forcing when there are no Asian mountains (their Fig. 10 (right)). But with Asian mountains (their Fig. 10 (left)), the effect of the Rockies and Greenland forcing is different from above, having an upstream ridge at 40°–50°N and a downstream trough at the east coast of North America, similar to the simulated stationary eddies in the present study (Fig. 3b). Both show the stationary eddy difference between with and without the Rockies and Greenland forcing, but they differ whether the Tibetan Plateau is included or not. This different situation causes a difference in the basic flow fields, particularly downstream of the Tibetan Plateau over the North Pacific. Therefore the systematic error of the basic flow over the Pacific may have resulted in an erroneous orographic response to the Rockies in the GCM.

The standard deviation of the 500 mb height increases with latitudes (Fig. 3c and 3f).

It is large downstream of the troughs and upstream of ridges, that is, over the North Pacific, over the North Atlantic and west of the Urals. Similar to the 200 mb zonal wind variability, simulated variance of the 500 mb height field is also smaller than the observed (Fig. 2b). Large variability in the North Pacific is shifted northward over Alaska in the GCM compared with the observed maximum over the ocean around 160°W, 50°N. This is related to the northeastward extension of the simulated East Asian subtropical jet (Fig. 1a). An intrusion of transient eddies from the North Pacific to Alaska and Canada was one of the systematic errors of the MRI·GCM-I (Tokioka *et al.*, 1985) and has been partly remedied by increasing surface drag coefficient over land due to sub-grid-scale topography (Yagai and Tokioka, 1987), but it still exists. Tokioka *et al.*(1985) point out the too low static stability in the model high latitudes due to the excessively cold temperature in the upper part of the model in high latitudes.

Moreover the simulated variance in the North Atlantic is smaller than the observed. Thus the model tends to stress the variability in the North Pacific than that in the North Atlantic (Fig. 2b). This could result in different principal recurrent modes appearing in the model from the observed.

4. Principal modes in the zonal wind and the 500 mb geopotential height

A conventional EOF analysis is performed to identify recurrent patterns of monthly mean anomalies. The multi-year climatology of each calendar month is subtracted from the respective monthly mean in each year. For the 200 mb zonal wind and the 500 mb geopotential height, these monthly mean data calculated at each grid point are then transformed into spherical harmonic functions which have a zonal wavenumber up to 8 and meridional nodes up to 13 as in Tokioka *et al.* (1986). The EOF analysis is applied for this time series data of truncated modes. For the zonal-mean zonal wind, data at five pressure levels (150, 300, 500, 700 and 900 mb) and at every 4° latitude from 86°S to 86°N multiplied by cosine of the latitude are used. Data for December, January and February are assumed independent. No normalizing procedure is applied (*i.e.*, covariance matrix is solved). The number of data is 60 for the GCM. For the observation it is 27 for the 200 mb zonal wind (1979–1987) and 132 for the 500 mb geopotential height (1946–1989).

a. 200 mb zonal wind

Figure 4 shows the leading four eigenvectors and eigencoefficients of the zonal wind at 200 mb (U200) in the GCM. The first eigenvector, denoted as $E_1^{GCM}(U200)$, explains 21.1% of the total variance. It is characterized by the meridional shift of the subtropical jet core at the East Asian jet entrance and exit regions and also at the Atlantic jet exit region. They are in-phase, that is, all jets shift meridionally in the same direction.

The second component ($E_2^{GCM}(U200)$, 14.9%) is characterized by large contributions from the two jet exit regions. Contrary to the first mode, the northward shift of one jet is accompanied with the southward shift of the other.

$E_3^{GCM}(U200)$ is mostly characterized by the variation in the Pacific basin. The coefficient, denoted as $C_3^{GCM}(U200)$, shows large contributions from 1972/73, 1982/83 and 1988/89 winters to this mode. The former two are the warm event years (El Niño: warm

SSTs in the central and eastern equatorial Pacific) and the last is the cold event year (La Niña: cold SSTs there). Warm event years are accompanied with easterly anomalies over the central equatorial Pacific, westerly anomalies in the subtropics in both hemispheres and again easterly anomalies to the south of Alaska over the North Pacific. By multiplying the coefficient with the spatial structure, one sees that the maximum anomaly explained by this mode is about 10 m s^{-1} at 0°N, 150°W in these three events. The similar magnitude of zonal wind anomalies are obtained in these events in the original data (Kitoh, 1990). As the observed anomaly is about -20 m s^{-1} for 1982/83 winter (Quiroz, 1983) and about $+15$ m s^{-1} for 1988/89 winter (Arkin, 1989), the simulated anomaly is more than two thirds smaller than the observed (Fig. 2a). $E_4^{GCM}(U200)$ explains only 5% of the total variance and shows rather scattered spatial distributions of variability. However in the Southern Hemisphere, this mode clearly shows the latitudinal shift of the jet.

Figure 5 shows the leading four eigenvectors and eigencoefficients of the observed U200. The first eigenvector, $E_1^{OBS}(U200)$, captures the zonal wind fluctuations in the Pacific related with ENSO, having large coefficients in 1982/83 winter. $E_2^{OBS}(U200)$ mostly retains the wind anomalies in the North Atlantic, while $E_3^{OBS}(U200)$ is characterized by the fluctuations in the jet exit regions both in the Pacific and in the Atlantic, which has in-phase relationship between the two regions. $E_4^{OBS}(U200)$ shows the out-of-phase fluctuations in the above two jet exit regions and also has a systematic north-south shift of the Southern Hemisphere jet.

In order to look at the similarity of the simulated U200 variability with the observed, pattern correlations of eigenvectors are calculated. Table 1a and 1b shows the correlation coefficients calculated for the global domain and for the Northern Hemisphere, respectively. In the global domain, $E_2^{GCM}(U200)$ corresponds to $E_2^{OBS}(U200)$, and $E_3^{GCM}(U200)$ to $E_1^{OBS}(U200)$. When the pattern is compared in the Northern Hemisphere (Table 1b), $E_1^{GCM}(U200)$ shows some similarity to $E_1^{OBS}(U200)$. In this case, $E_1^{GCM}(U200)$ and $E_3^{OBS}(U200)$, $E_2^{GCM}(U200)$ and $E_4^{OBS}(U200)$), $E_3^{GCM}(U200)$ and $E_1^{OBS}(U200)$ show

some similarity; that is, in-phase and out-of-phase jet fluctuations in the Pacific and the Atlantic and ENSO-related wind changes in the Pacific, respectively.

It is interesting to note that $C_1^{GCM}(U200)$ shows a fluctuation with a time-scale of about 10 years. The coefficients are positive and large in late '70s and late '80s and negative in early '70s and early '80s. There is an indication that $C_2^{GCM}(U200)$ also shows a similar fluctuation but with the sign reversed. When both the pattern and the sign are considered, this low-frequency variation may be a phenomenon related to the meridional shift of the East Asian jet over the North Pacific. This very low frequency variation comes from a signal inherent in the boundary condition adopted (SST) and will be discussed more later.

b. Zonal-mean zonal wind

Figure 6 shows the leading four eigenvectors and coefficients of the simulated zonal-mean zonal wind, $\overline{U}$, in the latitude-height domain. The first mode, $E_1^{GCM}(\overline{U})$, clearly shows the meridional shift of the Northern Hemisphere subtropical jet. Amplitude of the fluctuations reaches about 3 m s^{-1} in the upper troposphere. This mode is closely related to $E_1^{GCM}(U200)$. The time-series of the coefficients undergo a 10-year scale fluctuation similar to $C_1^{GCM}(U200)$.

Nigam (1990) made a rotated principal component analysis of the observed zonal-mean zonal wind using the ECMWF and NMC data for the 9-year period (1980-1988). The first mode found in the GCM corresponds to the fourth mode of the ECMWF and the fifth mode of the NMC analysis by Nigam (1990).

The variance of the mode represented by $E_2^{GCM}(\overline{U})$ is mostly confined in the Southern Hemisphere. This has a barotropic feature and shows a meridional displacement of the Southern Hemisphere subtropical jet. This mode is also observed as one of dominant modes by Nigam (1990) (the second and the first mode in the ECMWF and NMC data, respectively). It is noted here that there is an increasing trend in $C_2^{GCM}(\overline{U})$, indicating an equatorward shift of the Southern Hemisphere jet in recent 20 years at least in the GCM.

The third and the fourth modes are characterized by the upper tropospheric zonal wind variations in the tropics. This may be related to the variation of the Hadley circulation. $C_3^{GCM}(\overline{U})$ is large in 1982/83 winter, while $C_4^{GCM}(\overline{U})$ is large in 1972/73 and 1988/89 winters. This suggests different model responses to the SST anomalies in the 1972/73 El Niño and 1988/89 La Niña events from that in the strong 1982/83 El Niño event.

c. 500 mb height

In this subsection, eigenvectors of the geopotential height at 500 mb (Z500) in the Northern Hemisphere simulated with the GCM are compared with the observed. They are shown in Fig. 7 and Fig. 8, respectively.

The recurrent patterns in the real atmosphere have been known for a long time among long-range weather forecasters. Wallace and Gutzler (1981) objectively identified the Northern Hemisphere wintertime teleconnection patterns. $E_1^{OBS}(Z500)$ is similar to the Pacific/North American (PNA) pattern of Wallace and Gutzler (1981). $E_3^{OBS}(Z500)$ and $E_4^{OBS}(Z500)$ correspond to the western Atlantic (WA) and the western Pacific (WP) patterns, respectively. $E_2^{OBS}(Z500)$ shows a positive correlation between the strength of the Aleutian and Icelandic lows.

The dominant mode in the GCM is characterized by a north-south seesaw oscillation with its node around 55°N. This height contrast between the high and middle latitudes is large in the western North Pacific and in the western North Atlantic. The area from the Urals to the Caspian Sea has the same phase of oscillation as that in the polar region. This simulated pattern may be regarded as a combination of the fourth and first eigenvectors in the real atmosphere obtained for the period 1946–1989. The pattern correlation between $E_1^{GCM}(Z500)$ and $E_4^{OBS}(Z500)$ is +0.63 and that between $E_1^{GCM}(Z500)$ and $E_1^{OBS}(Z500)$ is −0.54 (Table 1c). As a matter of fact, $E_1^{GCM}(Z500)$ is similar to $E_4^{OBS}(Z500)$ over Eurasia and the North Pacific and to $E_1^{OBS}(Z500)$ particularly in the western Hemisphere.

The GCM also reproduces the observed second eigenvector of Z500. $E_2^{GCM}(Z500)$

corresponds to $E_2^{OBS}(Z500)$ with the pattern correlation of 0.81. This mode is characterized by anomalies over the North Pacific and over Greenland, and anomalies with different sign over Siberia, western Canada and the North Atlantic. There is a wavetrain over the Pacific from 180°E, 20°N, to south of the Aleutian islands to western Canada. In 1982/83 winter, both $C_2^{GCM}(Z500)$ and $C_2^{OBS}(Z500)$ are large negative, indicating a developed trough over the North Pacific as observed (Quiroz, 1983). Table 1c also shows some similarity between $E_3^{GCM}(Z500)$ and $E_4^{OBS}(Z500)$, but this mainly comes from the anomaly over the Aleutian islands.

We have shown that the leading EOF modes in the GCM correspond to those observed. The dominance of the simulated first mode, which has some similarity in part with $E_1^{OBS}(Z500)$ and in part with $E_4^{OBS}(Z500)$, can be to some extent interpreted as follows. The model climate and its variability are systematically different from those of the real atmosphere (Fig. 3). In particular, the model variability over the North Pacific is larger than that over the North Atlantic while they are in comparable magnitude in the observation. This results in that the recurrent patterns over the North Pacific can be extracted more easily in the model than in the real atmosphere.

Temporal variation of $C_1^{GCM}(Z500)$ also shows a fluctuation with its time-scale of about 10 years as found in $C_1^{GCM}(U200)$, $C_2^{GCM}(U200)$ and $C_1^{GCM}(\overline{U})$. This is not in surprise because of the equivalent barotropic nature of low-frequency variations in the extratropics (Wallace and Gutzler, 1981). This very low-frequency fluctuation is unlikely to occur purely by the atmospheric internal dynamics. Actually a similar recurrent mode to $E_1^{GCM}(Z500)$ is obtained as the first EOF mode (23.3%) of the 20-year simulation using the climatological SSTs (Fig. 9), but the coefficient of this mode does not show such a fluctuation. Therefore it can be that this mode is inherent in the model atmosphere and its appearance is somehow affected by the temporal changes of the prescribed SST variations. In the next section we investigate further this mode.

5. Decade scale fluctuation

The most recurrent pattern of the simulated monthly mean circulation in the Northern Hemisphere, captured in the 500 mb geopotential height, the 200 mb zonal wind and the zonal-mean zonal wind, has been shown to have fluctuated with its time-scale of about 10 years. It is also shown that the meridional shift of the subtropical jet in the East Asian jet exit and accompanying circulation changes have mostly contributed to this variation. Moreover a forcing of this decade scale atmospheric fluctuation may reside in the prescribed SSTs.

To give the distribution and amplitude of fluctuations of various variables with respect to this low-frequency variation, composit maps are prepared. Figure 10 shows the composit anomalies of the zonal wind at 200 mb, the geopotential height at 500 mb, the sea-level pressure, the surface air temperature, the precipitation and the vector wind at 850 mb. Composites are taken using the ensemble means of 7 months with the largest $C_1^{GCM}(U200)$ and those of 7 months with the smallest $C_1^{GCM}(U200)$.

Composit for the 200 mb zonal wind is just like the $C_1^{GCM}(U200)$ pattern itself (Fig. 4 (top)). Magnitude of this mode reaches more than $\pm$ 8 m s^{-1} at the jet exit region over the North Pacific. Composit for the 500 mb geopotential height is also similar to $E_1^{GCM}(Z500)$ (Fig. 7 (top)). Negative height anomaly over Alaska and northeast Siberia is -90 m deep and positive anomaly with $+60$ m is located at the North Pacific. Positive height anomalies cover the middle latitudes except around the Urals where the anomalous trough is situated. There are negative height anomalies in the entire tropics, suggesting below normal convective activity as a whole. The sea-level pressure distribution is similar to the 500 mb height anomaly pattern, but shows more clearly a contrast between the oceans and lands in the Northern Hemisphere middle latitudes together with the high to middle latitudes north-south seesaw oscillation. Contours of $\pm$8 mb are seen over the North Pacific, Canada and Greenland. Composit for the surface air temperature shows a southwest to northeast contrast along the east coast of the Eurasian continent and over North America. They are explained by advec-

tions by the near-surface wind anomalies. For example, warm temperature anomalies near Japan are associated with anomalous southeasterlies from relatively warm oceans; in other words, less intense northwesterly cold surge from Siberia. There are also systematic precipitation differences. In the tropics, negative precipitation anomaly over the maritime continent extending toward the dateline is distinct and makes a contrast with positive anomalies east of the dateline and over the Indian Ocean. Precipitation anomalies over the North Pacific and the North Atlantic are related to the displaced storm tracks and are balanced by evaporation anomalies due to surface wind changes and by anomalous moisture flux convergence (Kitoh, 1988a).

Above circulation composites are very similar, particularly over the North Pacific and the Eurasian continent, to the leading recurrent mode of the 500 mb height and accompanying surface air temperature anomalies obtained by Kitoh (1988a) in his SST anomaly experiment under the perpetual January condition. This mode is largely responsible to surface air temperature anomaly in the East Asia including Japan, as shown by the temperature contrast between Japan–Korea–East China and the Okhotsk–Bering Sea regions (Fig. 10). This temperature contrast between Japan and the Sea of Okhotsk is typical to the observed temperature anomaly (Kitoh, 1988a).

As already discussed, the mode in consideration is likely to be inherent in the model atmosphere but its time variation seems to be regulated somehow by the SST variations. Next we try to identify the key SST regions, if any. We calculated simultaneous correlations between time-series of the EOF coefficients of three leading U200 modes in the GCM and the SST at each grid point. They are shown in Fig. 11. On land grid points, the simulated monthly mean ground temperature is substituted.

Let us start by examining Fig. 11c, which reveals broad oceanic regions with significant correlations with $C_3^{GCM}(U200)$. When $C_3^{GCM}(U200)$ is positive, SSTs over the central and eastern equatorial Pacific and over the Indian Ocean are above normal and those over the central North Pacific centered at 170°W, 30°N and over the central South Pacific centered at

130°W, 30°S are below normal. This is a typical SST anomaly pattern in El Niño winters (Rasmusson and Carpenter, 1982; Kitoh, 1988b). In fact $C_3^{GCM}(U200)$ is large in El Niño or La Niña years.

Figure 11a shows correlations between $C_1^{GCM}(U200)$ and SST. Correlations over the oceans are generally smaller and less systematic than that found for the El Niño cases (Fig. 10c). However there are some sizable regions with definite magnitude of correlations over the equatorial Indian Ocean, around Indonesia, east of the Philippines to New Guinea, over the northwestern Pacific (around 170°E, 50°N) and over the northeast Pacific off the coast of North America (around 140°W, 40°N). Figure 11b shows that, in the western equatorial Pacific, SSTs around New Guinea are shown to have positive correlations with $C_2^{GCM}(U200)$. This region is where the correlation with the El Niño mode of $C_3^{GCM}(U200)$ is relatively small.

Figure 12 shows the distribution of simultaneous correlations between $C_1^{GCM}(\overline{U})$, $C_2^{GCM}(\overline{U})$, $C_3^{GCM}(\overline{U})$ and the SST. Figure 12a is quite similar to Fig. 11a in the western Pacific and the North Pacific. This is due to the in-phase meridional displacement of the two subtropical jets in $E_1^{GCM}(U200)$ (Fig. 4 (top)). The SST in the equatorial western Pacific east of the Philippines to northeast of New Guinea and over the northwestern Pacific are again below normal when $C_1^{GCM}(\overline{U})$ is positive. Based on these correlation maps (Figs. 11a, 11b and 12a), the SST variations around New Guinea and/or over the northwestern Pacific would be responsible to the decade scale fluctuation of the leading mode in the model atmosphere. As $C_1^{GCM}(U200)$ and $C_2^{GCM}(U200)$ show the out-of-phase fluctuation, the key SST region will be located where Fig. 11a and Fig. 11b have opposite polarity. Thus the most probable candidate is the region around New Guinea.

Up to this point, correlations are calculated with unfiltered data. In order to confine ourselves to the variation with its time scale longer than 5 years, a recursive band-pass filter (Murakami, 1979) is applied to the EOF coefficient and SST. The filter has a 1.0 response at 10 years and a 0.5 response at 5 and 20 years. Figure 13 shows the simultaneous correlations

between the filtered $C_1^{GCM}(\overline{U})$ and the filtered SST. It is shown that the SST anomalies northeast of New Guinea has the highest correlation with $C_1^{GCM}(\overline{U})$ in this time scale. Based on above results we consider the tropical western Pacific northeast of New Guinea as the key region for the decade scale fluctuation related to the East Asian jet displacement.

Other high correlation areas found over the North Pacific around 50°N (Figs. 11a, 12a and 13) and over the subtropical Pacific around 30°N (Fig. 12a) coincide with stronger and weaker than normal surface westerlies, respectively (Fig. 10). These SST anomalies may be a consequence of atmospheric circulation changes (Kawamura, 1984, 1986; Iwasaka *et al.*, 1987). The present experiment procedure is to give the SST which seasonally and interannually evolves as observed and to obtain the atmospheric responses to these continuously changing forcing. Therefore if strong relations are found between the SST and the simulated atmosphere, this implies that the local SST anomaly is truly and directly influencing the atmosphere or that the atmosphere is forced by another SST anomaly elsewhere which is also closely related to the other SST anomaly. Therefore although a possible positive role of the middle latitude SST in inducing the extratropical atmosphere to some special state cannot be discarded (Wallace and Jiang, 1987; Pitcher *et al.*, 1988; Lau and Nath, 1990), this might not be the case.

There are many investigations about the importance of the SST anomaly over the western tropical Pacific. Geisler *et al.*(1985) and Palmer and Mansfield (1986b) investigate the wintertime extratropical response to various SST anomalies in the equatorial Pacific and obtain the largest response to the western Pacific SST anomaly. Tokioka *et al.*(1986) show large impact of the SST anomaly over the equatorial western Pacific not only on the equatorial atmosphere but also on the extratropical atmosphere. Keshavamurty (1982) shows sensitivity to the location of the forcing in the northern summer case. Simmons *et al.*(1983) show that the forcing over the equatorial western Pacific most easily excite the response over the North Pacific in a barotropic model linearized about the 300 mb climatological January flow.

Kitoh (1988a) has studied the impact of the SST anomalies on wintertime atmospheric

circulations. He has performed the experiment under the perpetual January condition and used modest SST anomalies which is 1°C at most. Thus the experimental condition is very different from the present case where there is a seasonal cycle and the SST is changing as observed for 20 years with its maximum anomalies exceeding 3°C in some years. Despite these differences Kitoh (1988a) has obtained the leading mode similar to $E_1^{GCM}(Z500)$ shown in Fig. 7. Other variables also resemble the composit shown in Fig. 10. This mode, both in his and in the present case, accompanies the above normal precipitation west of Hawaii as well as the below normal precipitation around the maritime continent. In the western Pacific, the latter is accompanied by the upper troposphere mass convergence in the tropics and the divergence in the subtropics near 30°N. This configuration is favorable, through ageostrophic deceleration by divergent winds, for weakening the subtropical jet at its equatorside and shifting the jet poleward. This is consistent with Kitoh (1988a) who interprets this mode as an atmospheric response to subtropical mass source/sink under the framework of a linear theory.

Once the zonal flow has been changed, the orographically forced stationary waves are greatly influenced (Nigam and Lindzen, 1989). Perturbations which grow by barotropic and/or baroclinic instability are also modulated and cause different circulations in the extratropics. Even the atmospheric response to a given SST anomaly is very sensitive to the basic zonal flow. This is shown, for example, by Palmer and Mansfield (1986a) who use two versions of the GCM with and without an envelope orography and show very different extratropical response to a composit El Niño SST anomaly. It is thus plausible that the very low-frequency SST variations in the western tropical Pacific can exert influences on the atmospheric circulations in the middle latitudes through the modification of the East Asian subtropical jet.

There are a few comments on Fig. 12b and 12c. They are the correlations between the SST at each grid point and $C_2^{GCM}(\overline{U})$ and $C_3^{GCM}(\overline{U})$, respectively. They both show significant positive correlations over the tropical central and eastern Pacific surrounded by

negative correlations to its northwest and southwest, and positive correlations south of Japan and over the Indian Ocean. However the details are different between them over the Pacific. The SST anomaly distribution in Fig. 12c resembles that in the mature phase of El Niño (Rasmusson and Carpenter, 1982). The SST anomaly in Fig. 12b has higher correlations than that in Fig. 12c over the eastern Pacific both in the tropics and in the North Pacific. This also shows positive correlations over the tropical Atlantic. As shown in $C_2^{GCM}(\overline{U})$, it is this SST anomalies which has an increasing trend through 1970s and 1980s. Note that $C_2^{GCM}(\overline{U})$ is positive in the 1972/73 event. This SST anomaly distribution is also similar to what reported by Nitta and Yamada (1989) and is responsible to recent deepening of the Aleutian low.

6. Conclusions

An atmospheric GCM at the MRI is integrated using the observed SST which changes month-to-month from September 1969 to February 1990. These SST covers from 40°S to 60°N. Outside of this domain the climatological SST is used. For this 20.5 year data, monthly means for December, January and February from 1970/71 to 1989/90 winter seasons are analyzed to investigate low-frequency variability in the Northern Hemisphere extratropics.

First of all, model's systematic biases from the observation are identified. The simulated East Asian subtropical jet is slightly shifted northward at the longitude of its maximum strength over Japan and more at the jet exit region over the North Pacific. The trough over eastern Canada in the 500 mb geopotential height is not established well in the GCM. The variability of the model atmosphere as seen in U200 and Z500 is weaker than the observed in the tropics as well as in the extratropics. Probably due to these systematic errors, the model has larger variability over the North Pacific than over the North Atlantic, while the real atmosphere has comparable magnitude of variability over the two northern oceans. This may lead to that the present model is more sensitive to recurrent atmospheric circulation patterns occurring over the North Pacific than those in other regions.

The EOF analysis has been performed with the wintertime U200, Z500 and zonal-mean zonal wind. It has been shown that the simulated leading recurrent patterns have their counterparts in the real atmosphere. The first mode in Z500 is characterized by the north-south seesaw oscillation with its node around 55°N with the Western Pacific pattern superposed. The corresponding first mode in U200 is characterized by the meridional shift of both the East Asian and the Atlantic subtropical jets. This mode resembles the observed first and fourth EOF modes in Z500 and the observed first and third modes in U200. The first EOF mode of the simulated zonal-mean zonal wind shows the meridional shift of the Northern Hemisphere jet. Nigam (1990) reports a similar mode in the ECMWF and NMC data for the 9-year period 1980–1988.

Eigencoefficients of these modes related to the meridional shift of the East Asian subtropical jet are shown to be fluctuating with its time scale of about 10 years. Correlations with the SST suggests that the western Pacific northeast of New Guinea is likely to be the key regions of this very low-frequency fluctuation. This mode is accompanied with the above normal sea-level pressure and anticyclonic surface wind anomalies over the North Pacific, resulting in weaker cold surge from Siberia and warmer than normal surface air temperatures in East Asia. This is contrasted with the cold surface air temperature anomalies over East Siberia and the Bering Sea region.

Surface air temperature around Japan is influenced by this mode as well as the ENSO mode. The former mostly accounts for the temperature variation northward of 40°N while the latter dominates southward of 40°N. This may be one of the reasons why winter climate of Japan is not well correlated with the El Niño phenomenon. On the other hand, the west coast of North America is more influenced by this ENSO mode. There the model succeeds to simulate warmer than normal surface air temperatures and less snowfall particularly along the U.S.–Canada border of the west coast of North America when the SST over the equatorial central Pacific (0°N, 160°W) is warmer than normal.

The very low-frequency mode mentioned above seems to be very easily detected in this particular model because there is a systematic error to intensify the atmospheric variation over the North Pacific more than that over the North Atlantic due to the larger model atmosphere variability in the Pacific than in the Atlantic.

It is also shown that the second EOF mode of the zonal-mean zonal wind is characterized by the meridional shift of the Southern Hemisphere jet and its principal component (coefficients) has an increasing trend, corresponding to the equatorward shift of the Southern Hemisphere jet for the period 1970–1989. This is associated with the trend found in the SST.

Acknowledgments

The author is grateful to T. Tokioka for discussion. This research is a part of "Japanese Experiment on Asian Monsoon (JEXAM)" supported by the Science and Technology Agency. Computations are made with HITAC S810/10 at Meteorological Research Institute.

References

Alexander, R. C. and R. L. Mobley, 1976: Monthly average sea surface temperature and ice pack limits for 1° global grid. *Mon. Wea. Rev.,* **104**, 143-148.

Arakawa, A. and W. H. Schubert, 1974: Interactions of a cumulus cloud ensemble with the large-scale environment. Part I. *J. Atmos. Sci.,* **31**, 674-701.

Arkin, P. A., 1989: The global climate for December 1988–February 1989: Cold episode in the tropical Pacific continues. *J. Climate,* **2**, 737-757.

Bjerknes, J., 1969: Atmospheric teleconnections from the equatorial Pacific. *Mon. Wea. Rev.,* **97**, 163-172.

Boville, B. A., 1984: The influence of the polar night jet on the tropospheric circulation in a GCM. *J. Atmos. Sci.,* **41**, 1132-1142.

Boville, B. A. and X. Cheng, 1988: Upper boundary effects in a general circulation model. *J. Atmos. Sci.,* **45**, 2591-2606.

Geisler, J. E., M. L. Blackmon, G. T. Bates and S. Munoz, 1985: Sensitivity of January climate response to the magnitude and position of equatorial sea surface temperature anomalies. *J. Atmos. Sci.,* **42**, 1037-1049.

Graham, N. E., T. P. Barnett, R. M. Chervin, M. E. Schlesinger and U. Schlese, 1989: Comparison of GCM and observed surface wind fields over the tropical Indian and Pacific Oceans. *J. Atmos. Sci.,* **46**, 760-788.

Horel, J. D. and J. M. Wallace, 1981: Planetary-scale atmospheric phenomena associated with the Southern Oscillation. *Mon. Wea. Rev.,* **109**, 813-829.

Iwasaka, N., K. Hanawa and Y. Toba, 1987: Analysis of SST anomalies in the North Pacific and their relation to 500 mb height anomalies over the Northern Hemisphere. *J. Meteor. Soc. Japan,* **65**, 103-114.

Kang, I.-S. and N.-C. Lau, 1986: Principal modes of atmospheric variability inmodel atmospheres with and without anomalous sea surface temperature forcing in the tropical Pacific. *J. Atmos. Sci.,* **43**, 2719-2735.

Kawamura, R., 1984: Relation between atmospheric circulation and dominant sea surface temperature anomaly pattern in the North Pacific during the northern winter. *J. Meteor. Soc. Japan,* **62**, 910-916.

Kawamura, R., 1986: Seasonal dependency of atmosphere-ocean interaction over the North Pacific. *J. Meteor. Soc. Japan,* **64**, 363-371.

Keshavamurty, R. N., 1982: Response of the atmosphere to sea surface temperature anomalies over the equatorial Pacific and the teleconnections of the Southern Oscillation. *J. Atmos. Sci.,* **39**, 1241-1259.

Kitoh, A., 1988a: A numerical experiment on sea surface temperature anomalies and warm winter in Japan. *J. Meteor. Soc. Japan,* **66**, 515-533.

Kitoh, A., 1988b: Correlation between the surface air temperature over Japan and the global sea surface temperature. *J. Meteor. Soc. Japan,* **66**, 967-986.

Kitoh, A., K. Yamazaki and T. Tokioka, 1990: The double-jet and semi-annual oscillations in the Southern Hemisphere simulated by the Meteorological Research Institute general circulation model. *J. Meteor. Soc. Japan,* **68**, 251-264.

Kitoh, A., 1990: Interannual variations of the tropical atmosphere in an atmospheric GCM forced by the 1970–1989 SST. *(Submitted to J. Meteor. Soc. Japan)*

Latif, M., J. Biercamp, H. von Storch, M. J. McPhaden and E. Kirk, 1990: Simulation of ENSO related surface wind anomalies with an atmospheric GCM forced by observed SST. *J. Climate,* **3**, 509-521.

Lau, K.-M. and J. S. Boyle, 1987: Tropical and extratropical forcing of the large-scale circulation: A diagnostic study. *Mon. Wea. Rev.,* **115**, 400-428.

Lau, N.-C., 1981: A diagnostic study of recurrent meteorological anomalies appearing in a 15-year simulation with a GFDL general circulation model. *Mon. Wea. Rev.,* **109**, 2287-2311.

Lau, N.-C., 1985: Modeling the seasonal dependence of the atmospheric response to observed El Niños in 1962–76. *Mon. Wea. Rev.,* **113**, 1970-1996.

Lau, N.-C., 1988: Modeling of ENSO phenomena at GFDL. *Japan-U.S. Workshop on the El Niño Southern Oscillation Phenomenon. (University of Tokyo, November 3-7, 1987)* Meteor. Res. Rep., 88-1, Division of Meteorology, Geophysical Institute, University of Tokyo, 160-168.

Lau, N.-C. and M. J. Nath, 1990: A general circulation model study of the atmospheric response to extratropical SST anomalies observed in 1950–79. (manuscript)

Manabe, S. and D. G. Hahn, 1981: Simulation of atmospheric variability. *Mon. Wea. Rev.,* **109**, 2260-2286.

Matthews, E., 1983: Global vegetation and land use: new high resolution data bases for climatic studies. *J. Clim. and App. Meteor.,* **22**, 474-487.

Murakami, M., 1979: Large-scale aspects of deep convective activity over the GATE area. *Mon. Wea. Rev.,* **107**, 994-1013.

Nigam, S., 1990: On the structure of variability of the observed tropospheric and stratospheric zonal-mean zonal wind. *J. Atmos. Sci.,* **47**, 1799-1813.

Nigam, S. and R. S. Lindzen, 1989: The sensitivity of stationary waves to variations in the basic state zonal flow. *J. Atmos. Sci.,* **46**, 1746-1768.

Nihoul, J. C. J (Editor), 1985: *Coupled Ocean-Atmosphere Models.* Elsevier Science Publishers, Amsterdam.

Nitta, Ts. and S. Yamada, 1989: Recent warming of tropical sea surface temperature and its relationship to the Northern Hemisphere circulation. *J. Meteor. Soc. Japan,* **67**, 375-383.

Palmer, T. N., 1987: Modelling low frequency variability of the atmosphere. *Atmospheric and Oceanic Variability.* Royal Meteor. Soc., H. Cattle (ed.), 75-103.

Palmer, T. N., 1988: Large-scale tropical, extratropical interactions on time-scales of a few days to a season. *Aust. Met. Mag.,* **36**, 107-125.

Palmer, T. N. and D. A. Mansfield, 1986a: A study of wintertime circulation anomalies during past El Niño events using a high resolution general circulation model. I: Influence of model climatology. *Quart. J. R. Met. Soc.,* **112**, 613-638.

Palmer, T. N. and D. A. Mansfield, 1986b: A study of wintertime circulation anomalies during past El Niño events using a high resolution general circulation model. I: Variability of the seasonal mean response. *Quart. J. R. Met. Soc.,* **112**, 639-660.

Pitcher, E. J., M. L.Blackmon, G. T. Bates and S. Munoz, 1988: The effect of North Pacific sea surface temperature anomalies on the January climate of a general circulation model. *J. Atmos. Sci.,* **45**, 173-188.

Quiroz, R. S., 1983: The climate of the "El Niño" winter of 1982–1983 — A season of extraordinary climatic anomalies. *Mon. Wea. Rev.,* **111**, 1685-1706.

Rasmusson, E. M. and T. H. Carpenter, 1982: Variations in tropical sea surface temperature and surface wind fields associated with the Southern Oscillation/El Niño. *Mon. Wea. Rev.,* **110**, 354-384.

Simmons, A. J., J. M. Wallace and G. W. Branstator, 1983: Barotropic wave propagation and instability, and atmospheric teleconnection pattern. *J. Atmos. Sci.,* **40**, 1363-1392.

Storch, H. v., M. Latif and J. Biercamp, 1989: Simulation of the Southern Oscillation in an atmospheric general circulation model. *Phil. Trans. R. Soc. Lond.*, **A 329**, 179-188.

Tokioka, T., K. Yamazaki, I. Yagai and A. Kitoh, 1984: *A description of the Meteorological Research Institute atmospheric generl circulaton model (MRI·GCM-I).* Technical Report of the Meteorological Research Institute, No. 13, MRI, Tsukuba, 249 pp.

Tokioka, T., A. Kitoh, I. Yagai and K. Yamazaki, 1985: A simulation of the tropospheric general circulation with the MRI atmospheric general circulation model. Part I: The January performance. *J. Meteor. Soc. Japan,* **63**, 749-778.

Tokioka, T. and A. Noda, 1986: Effects of large-scale orography on January atmospheric circulation: A numerical experiment. *J. Meteor. Soc. Japan,* **64**, 819-840.

Tokioka, T., A. Kitoh and A. Katayama, 1986: Atmospheric response to the sea surface temperature anomalies in the mature phase of El Niño: Numerical experiment under the perpetual January condition. *J. Meteor. Soc. Japan,* **64**, 347-362.

Tokioka, T., K. Yamazaki, A. Kitoh and T. Ose, 1988: The equatorial 30-60 day oscillation and the Arakawa-Schubert penetrative cumulus parameterization. *J. Meteor. Soc. Japan,* **66**, 883-901.

van Loon, H. and J. C. Rogers, 1981: The Southern Oscillation. Part II: Associations with changes in the middle troposphere in the northern winter. *Mon. Wea. Rev.,* **109**, 1163-1168.

Volmer, J. P., M. Deque and M. Jarraud, 1983: Large-scale fluctuations in a long-range integration of the ECMWF spectral model. *Tellus,* **35A**, 173-188.

Volmer, J. P., M. Deque and D. Rousselet, 1984: EOF analysis of 500 mb geopotential: a comparison between simulation and reality. *Tellus,* **36A**, 336-347.

Wallace, J. M. and D. S. Gutzler, 1981: Teleconnections in the geopotential height field during the Northern Hemisphere winter. *Mon. Wea. Rev.,* **109**, 784-812.

Wallace, J. M. and Q.-R. Jiang, 1987: On the observed structure of the interannual variability of the atmosphere/ocean climate system. *Atmospheric and Oceanic Variability.* Royal Meteor. Soc., H. Cattle (ed.), 17-43.

World Climate Programme, 1986: *Comparison of Simulations by Numerical Models of the Sensitivity of the Atmospheric Circulation to Sea Surface Temperature Anomalies.* NCAR, Boulder, Colo., December 1985. WMO/TD-No.138, WCP-121, 188 pp.

Yagai, I. and T. Tokioka, 1987: The effect of increased surface drag coefficient over the continents on January circulations. *Short- and Medium-Range Numerical Weather Prediction. (T. Matsuno, ed.) Special Volume of J. Meteor. Soc. Japan,* 409-419.

Table 1. Pattern correlations (%) of the EOF eigenvectors between the model and the observation. Correlations are calculated for global (90°S-90°N) or over the Northern Hemisphere (10°N-90°N). The EOF eigenvectors for the GCM are obtained from 20 year data, while those for the observation are obtained from 9 year (1979-1987) for the zonal wind at 200 mb (U200) and from 44 year (1946-1989) for the geopotential height at 500 mb (Z500).

(a) U200 global

	GCM1	GCM2	GCM3	GCM4
OBS1	-37	10	**49**	-3
OBS2	23	**57**	5	-32
OBS3	23	-2	8	24
OBS4	-31	33	-12	23

(b) U200 N.H.

	GCM1	GCM2	GCM3	GCM4
OBS1	**-54**	20	39	-15
OBS2	21	**73**	-10	-30
OBS3	35	-11	2	20
OBS4	-32	45	9	32

(c) Z500 N.H.

	GCM1	GCM2	GCM3	GCM4
OBS1	**-54**	-29	-25	18
OBS2	-19	**81**	1	1
OBS3	14	-9	6	-26
OBS4	**63**	-9	**-51**	25

大気大循環モデルにおける北半球冬季の長周期変動
—1970-1989 年の観測された海面水温による強制実験

鬼頭昭雄
(気象研究所気候研究部)

１９６９年９月から１９９０年２月までの年々変化する観測された全球（南緯４０度ー北緯６０度）海面水温を与えて気象研究所大気大循環モデルの積分を行ない、２０年の冬の北半球大気の長周期変動について主成分解析により解析し、観測と比較した。モデル中に現われた 200 mb 東西風、500 mb 高度および帯状平均東西風の第１主成分は約１０年の時間スケールで変動している。この変動は熱帯西部太平洋ニューギニア北東方の海面水温変動と関係が深い。東アジア亜熱帯ジェットの南北シフトとそれに伴う北半球スケールの循環変動が顕著で、特に日本付近とベーリング海からアラスカにかけての北大平洋との気温コントラストを伴っている。観測では 500 mb 高度場の第１及び第４主成分に対応するモードが見られる。モデルでは北大西洋より相対的に北太平洋での変動度が大きい系統誤差があり、このため東アジアジェットの変動に伴うモードが主要モードとして現われていると考えられる。またモデル中の帯状平均東西風の第２主成分として、南半球ジェットの南北シフトが得られた。このモードはモデル積分期間にわたって赤道方向へシフトするトレンドがあり、全球スケールの海面水温のこの期間のトレンドと関係している。

Figure Legends

Fig. 1 (a) Simulated 20-year averaged zonal wind at 200 mb for December–February. Contour interval is 5 m s^{-1}. Values greater than 50 are hatched and values less than 0 are dotted. (b) Simulated standard deviations of the monthly mean zonal wind at 200 mb for December–February. Contour interval is 0.5 m s^{-1}. Values greater than 5 are hatched. (c)–(d) As in (a)–(b) except for the observation for the period 1979–1987.

Fig. 2 (a) Ratio (%) of the standard deviation of the simulated monthly mean zonal wind at 200 mb for December–February to that observed. Standard deviations are calculated from 20-year data for the GCM and 9-year data (1979–1987) for the observed. Contour interval is 20 %. Values greater than 100 % are hatched. (b) As in (a) except for the geopotential height at 500 mb.

Fig. 3 (a) Simulated geopotential height at 500 mb for December–February. Contour interval is 60 m. Contours between 5400 m and 5700 m are dashed. (b) Simulated geopotential height at 500 mb for December–February with the zonal mean removed. Contour interval is 30 m. Negative values are dashed. (c) Simulated standard deviations of the monthly mean geopotential height at 500 mb for December–February calculated from the value with the zonal mean retained. Contour interval is 10 m. Contours less than 50 m are dashed. (d)–(f) As in (a)–(c) except for the observation for the period 1946–1989.

Fig. 4 (top to bottom) First, second, third and fourth EOFs and coefficients of the simulated zonal wind at 200 mb for December–February. Contribution from each EOF is shown at the top of the figure. Contour interval is 0.5 m s^{-1}. Negative values are hatched. Coefficients for consecutive months are connected by lines.

Fig. 5 As in Fig. 4 except for the 9-year (1979–1987) observation.

Fig. 6 As in Fig. 4 except for the zonal-mean zonal wind in the GCM. A thick dashed line in the first and second EOF maps indicates the jet axis in the Northern Hemisphere and in the Southern Hemisphere, respectively.

Fig. 7 As in Fig. 4 except for the geopotential height at 500 mb in the Northern Hemisphere.

Contour interval is 0.5 m.

Fig. 8 As in Fig. 7 except for the 44-year (1946–1989) observation.

Fig. 9 As in Fig. 7 except for the first EOF for the 20-year GCM run with the climatological SST.

Fig. 10 Composit maps of the zonal wind at 200 mb, the geopotential height at 500 mb, the sea-level pressure, the surface air temperature, the precipitation and the vector wind at 850 mb for the large seven and small seven events of $C_1^{GCM}(U200)$. Contour intervals are 2 m s^{-1}, 20 m, 2 mb, 1 °C and 0.5 mm d^{-1}, respectivecne vector is 2 m s^{-1}.

Fig. 11 Correlations between (a) $C_1^{GCM}(U200)$, (b) $C_2^{GCM}(U200)$ and (c) $C_3^{GCM}(U200)$ and the SST (ocean grid points) or the simulated ground temperature (land grid points). Contour interval is 20 %. Negative values are hatched. Siginificant grid points with the 95 % level are indicated by dots.

Fig. 12 As in Fig. 11 except for $C_1^{GCM}(\overline{U})$, $C_2^{GCM}(\overline{U})$ and $C_3^{GCM}(\overline{U})$.

Fig. 13 Correlations between the filtered $C_1^{GCM}(\overline{U})$ and the filtered SST. A filter has a 1.0 response at 10 years and a 0.5 response at 5 and 20 years. Values less than -60% are hatched and values greater than 60% are dotted.

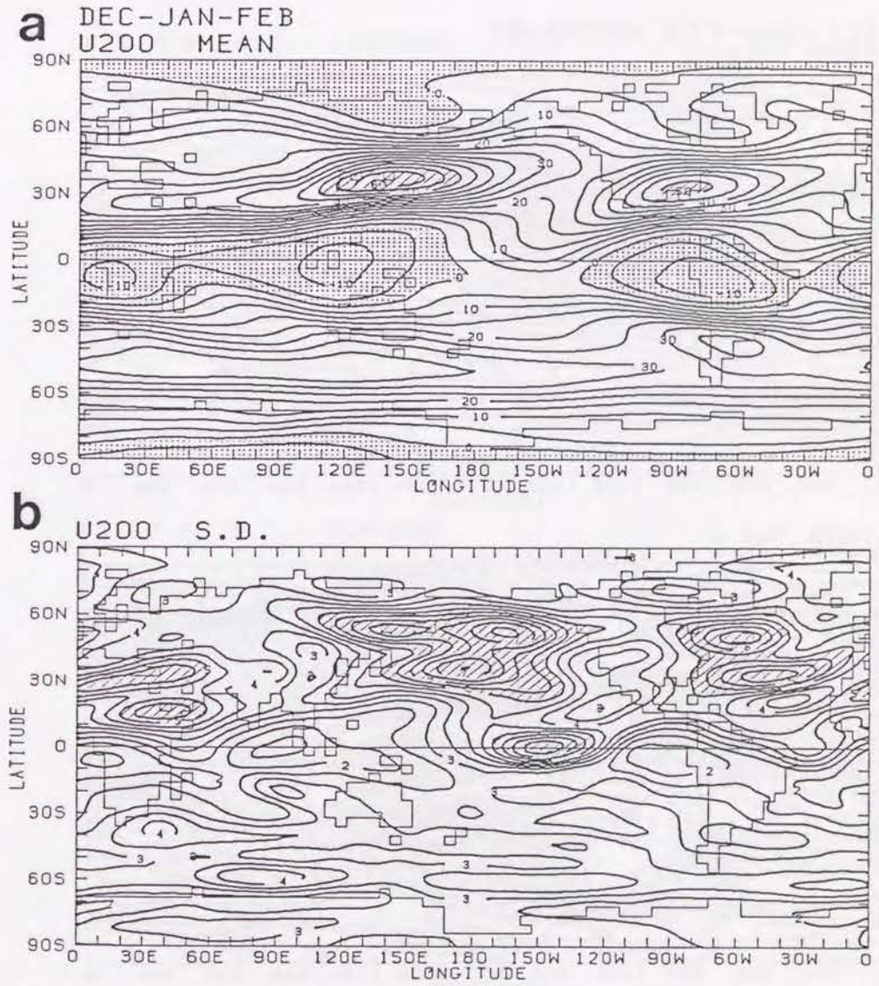

FIGURE 1

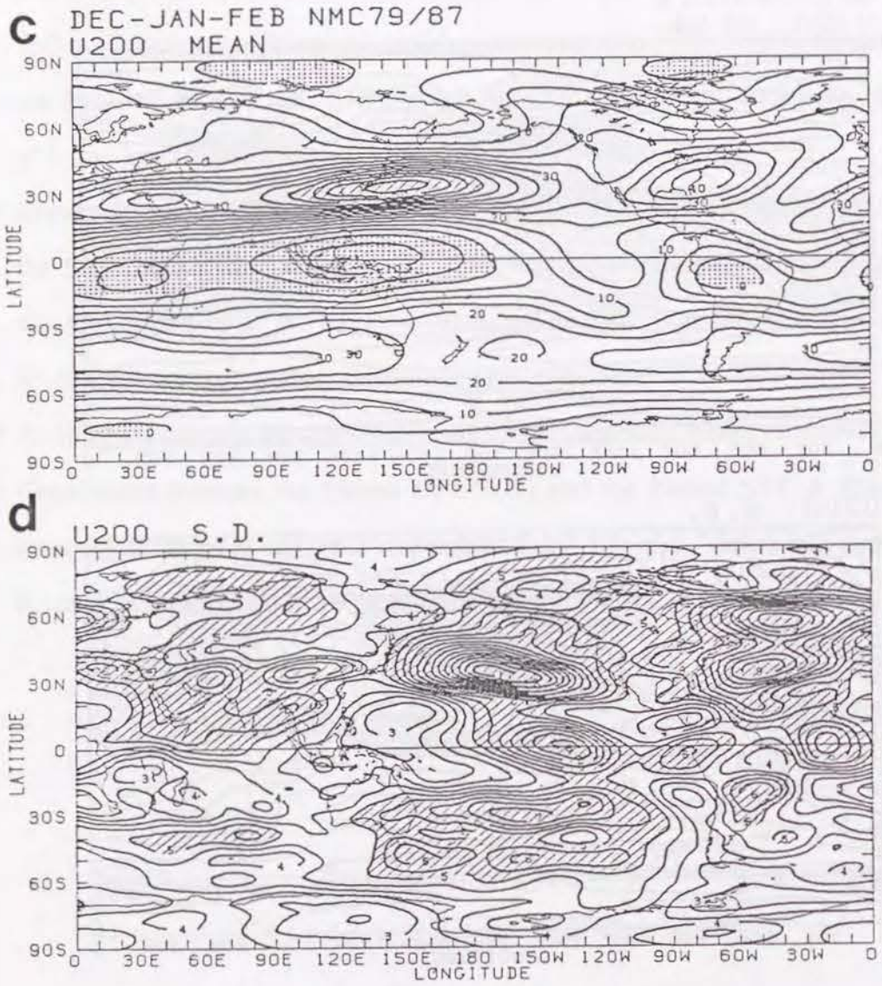

FIGURE 1 (cont)

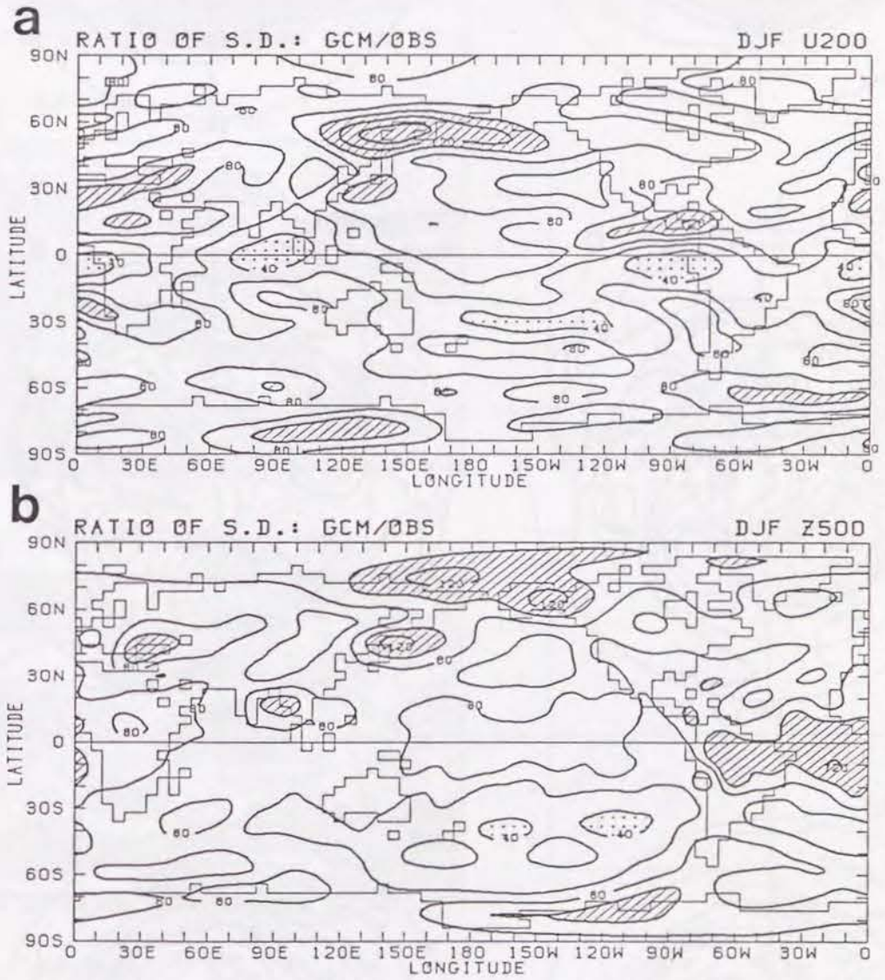

FIGURE 2

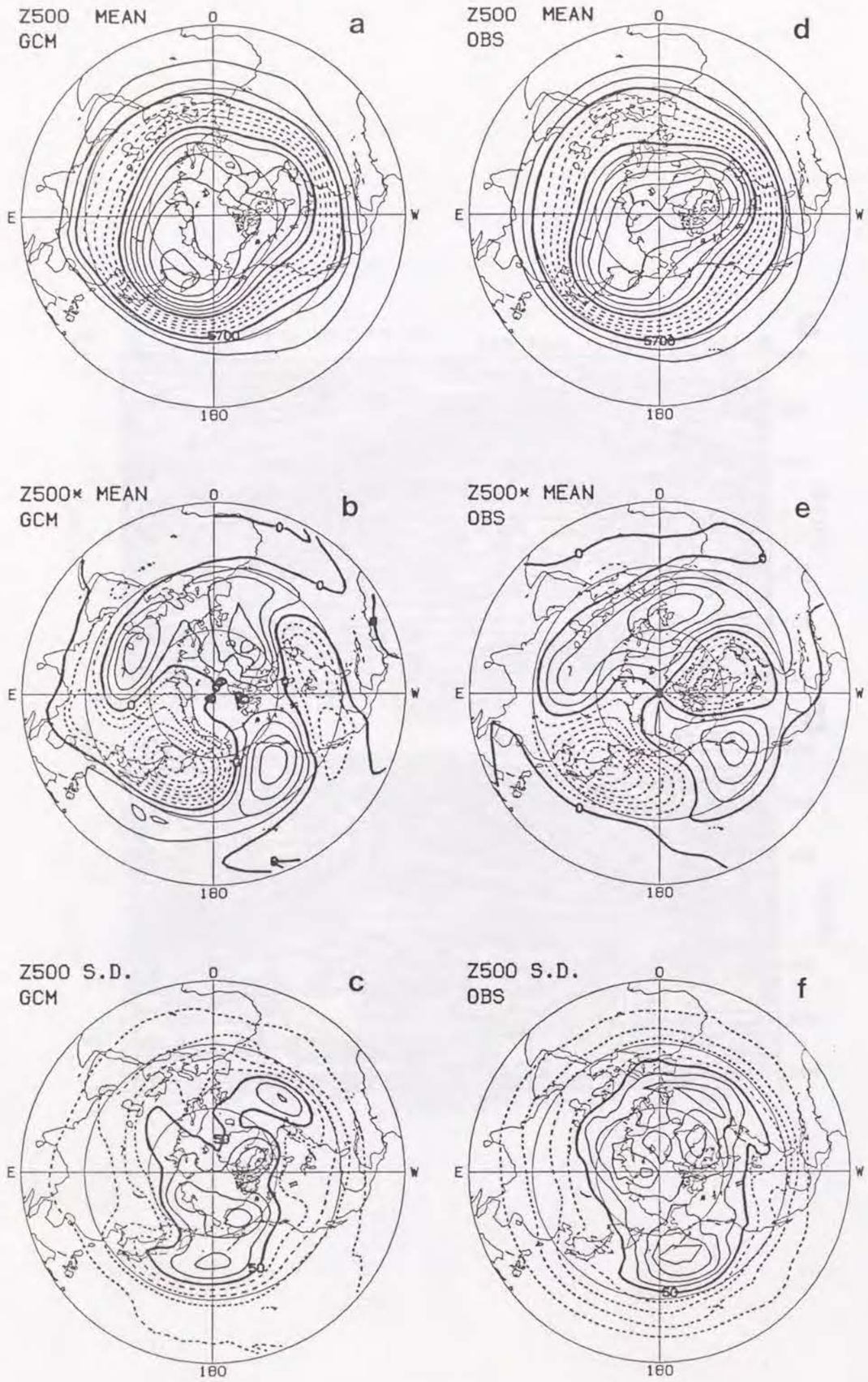

FIGURE 3

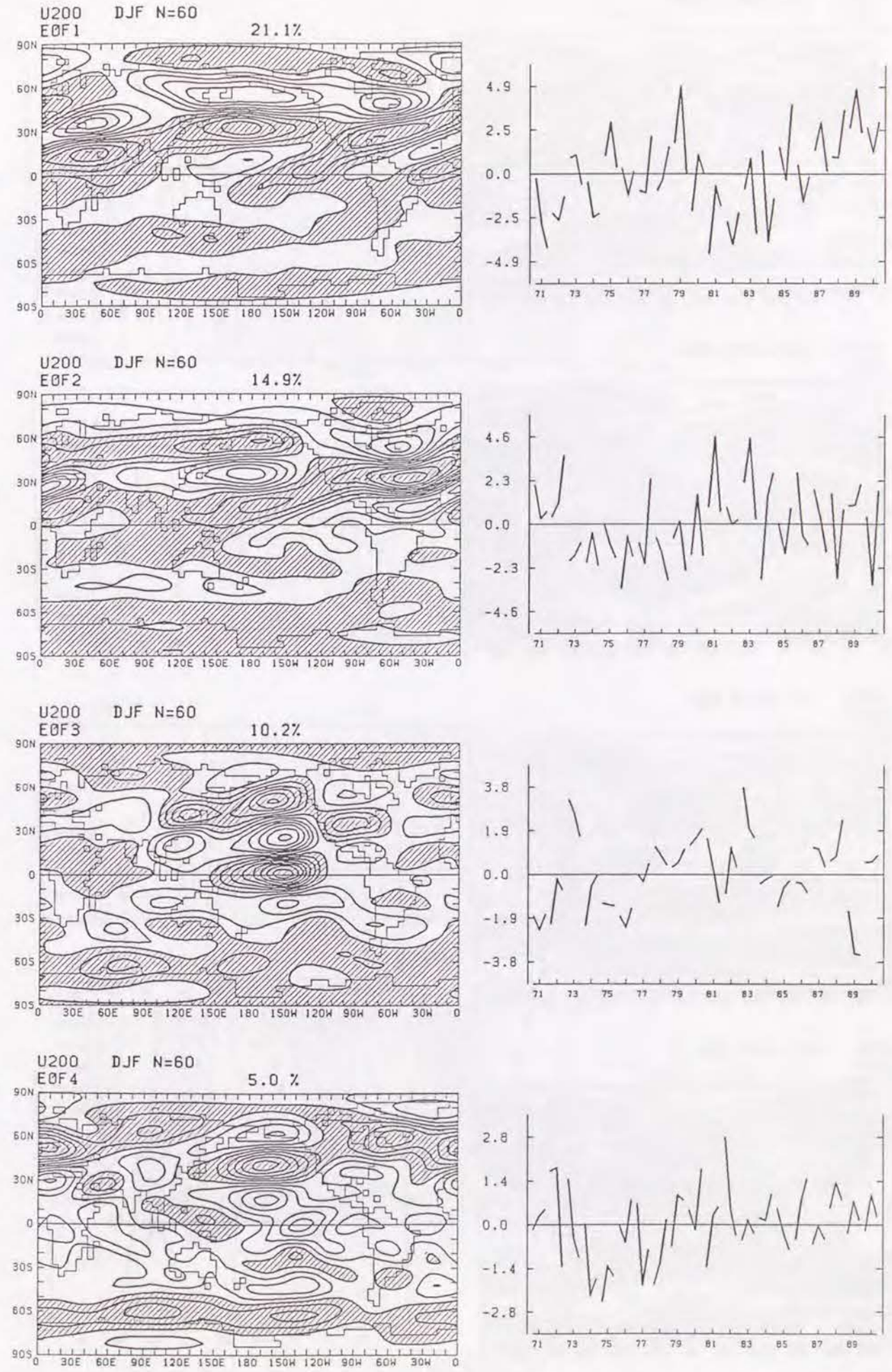

FIGURE 4

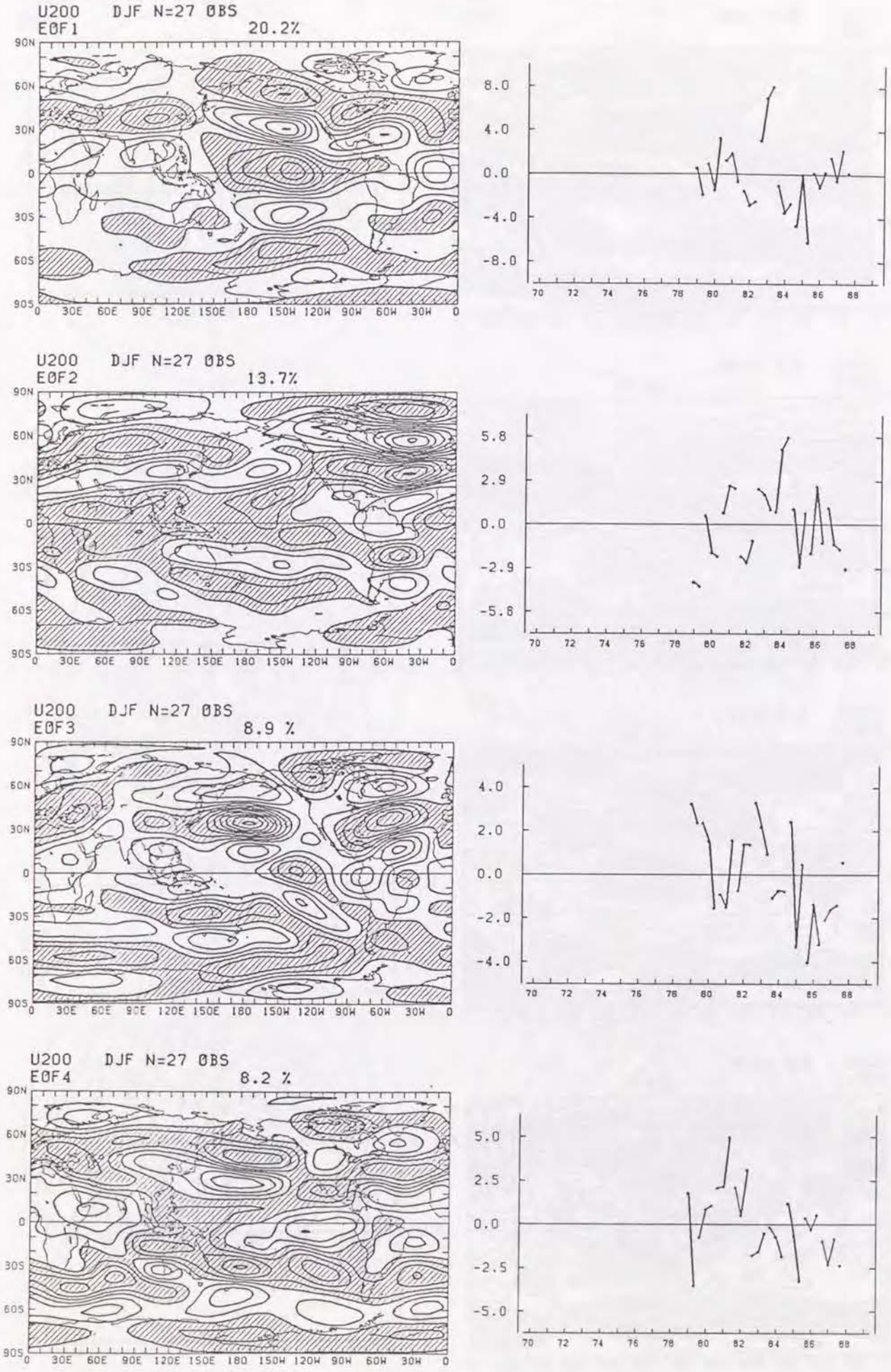

FIGURE 5

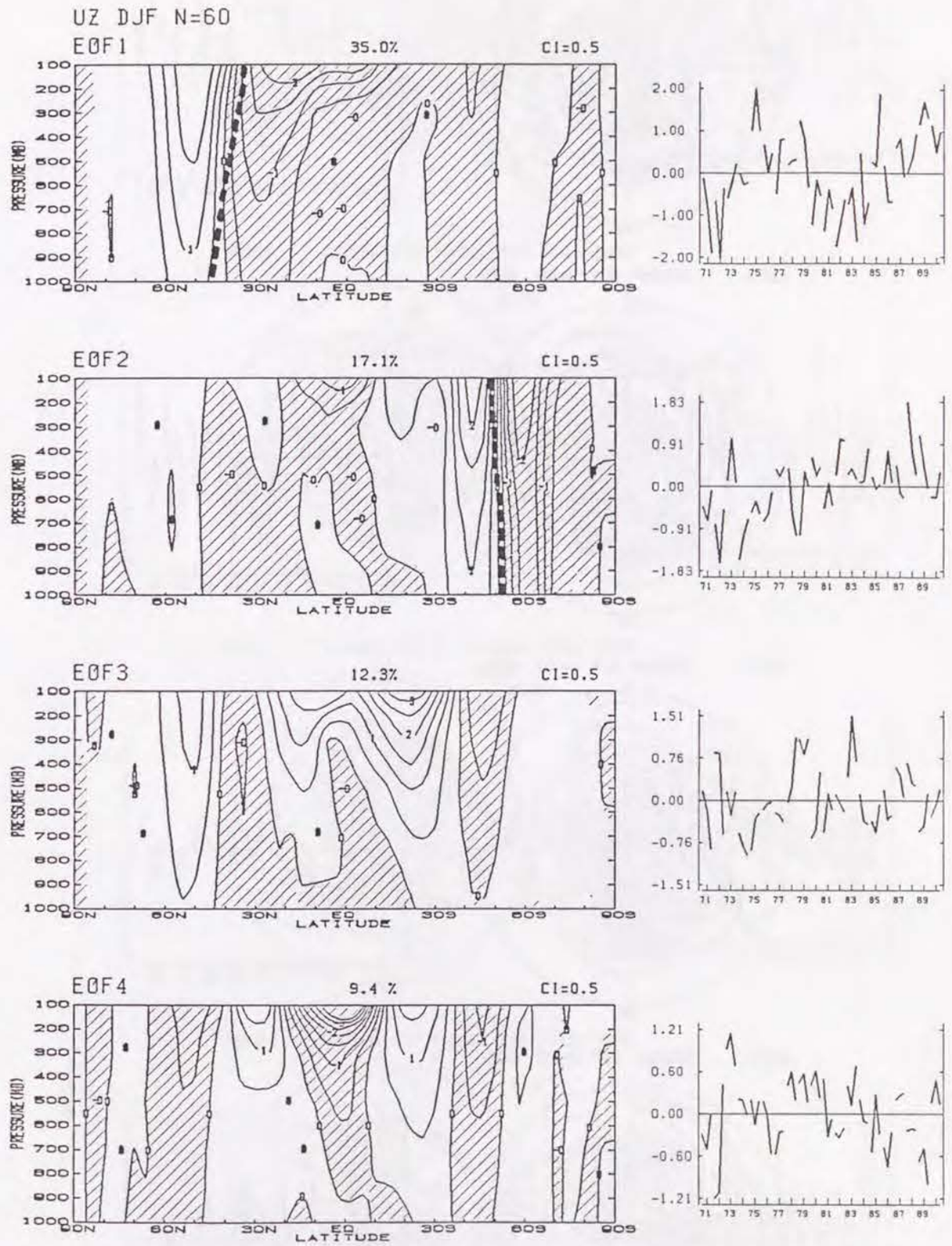

FIGURE 6

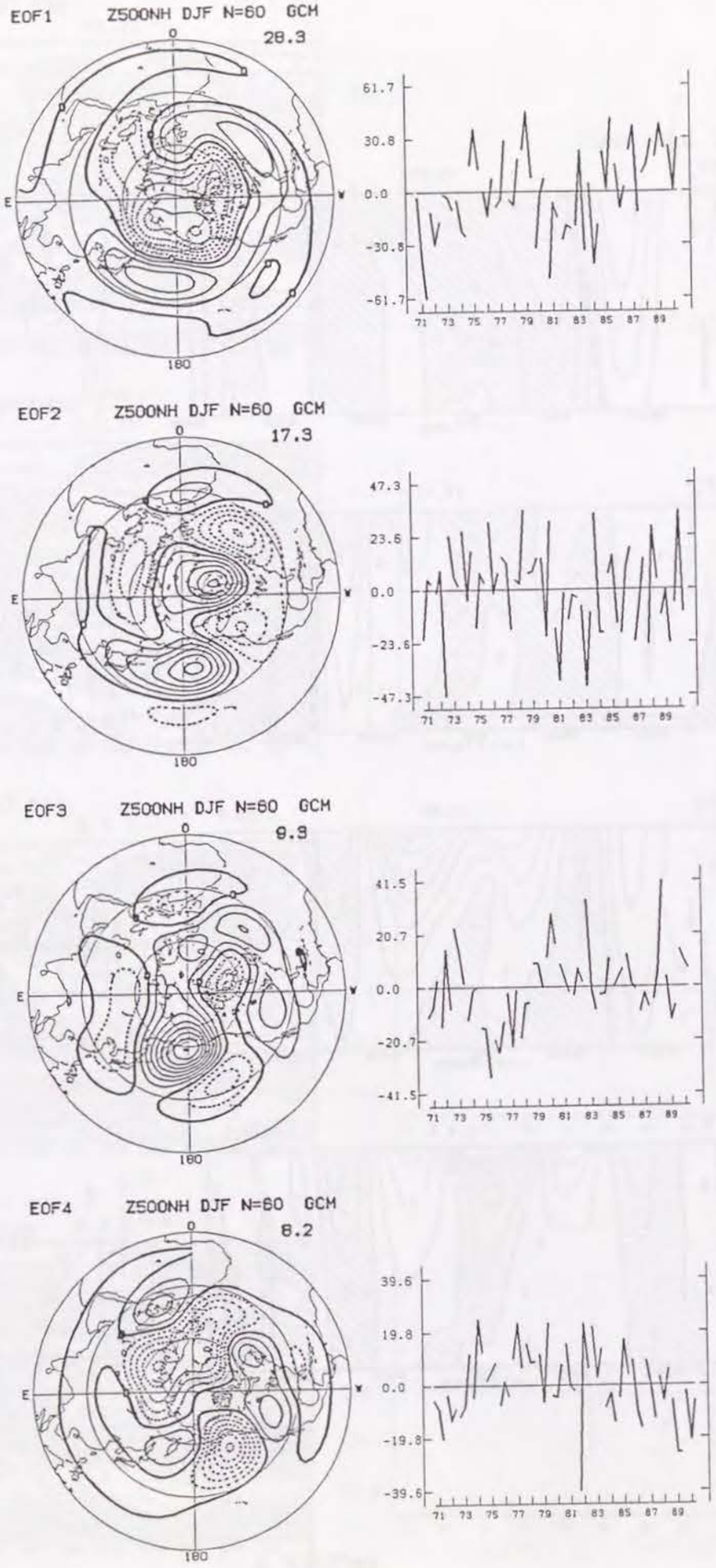

FIGURE 7

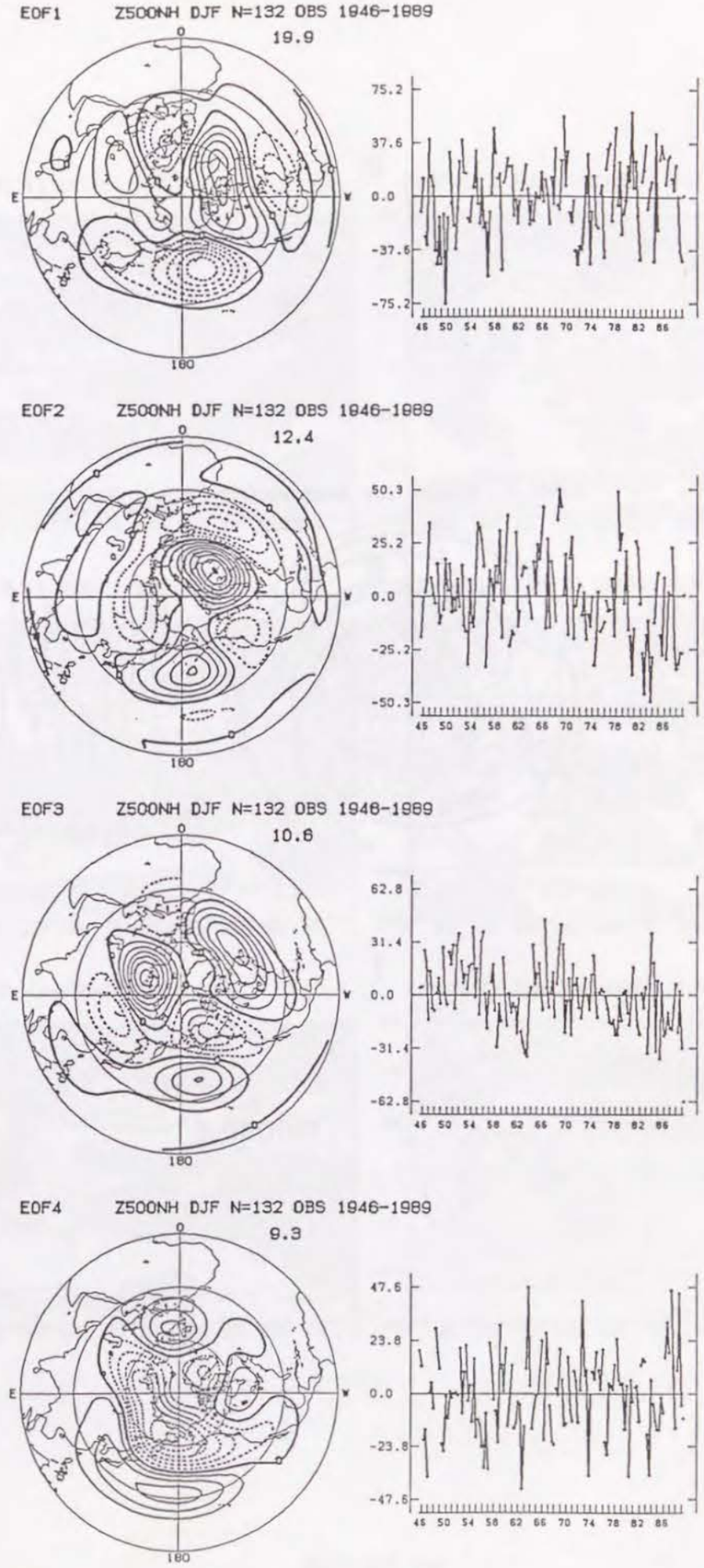

FIGURE 8

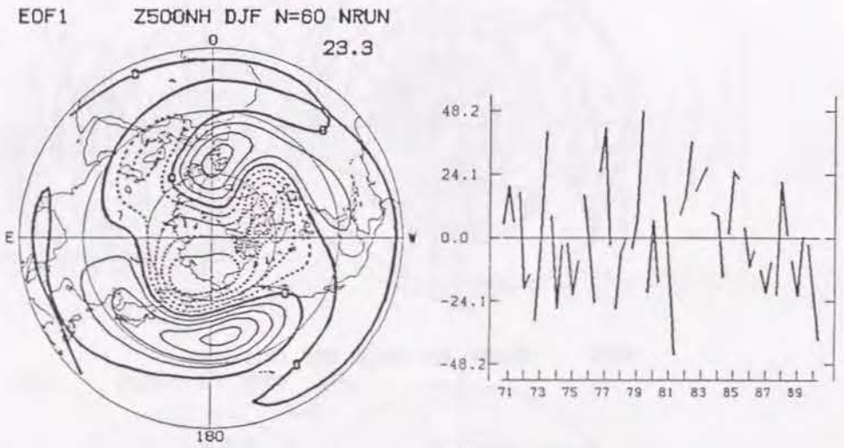

FIGURE 9

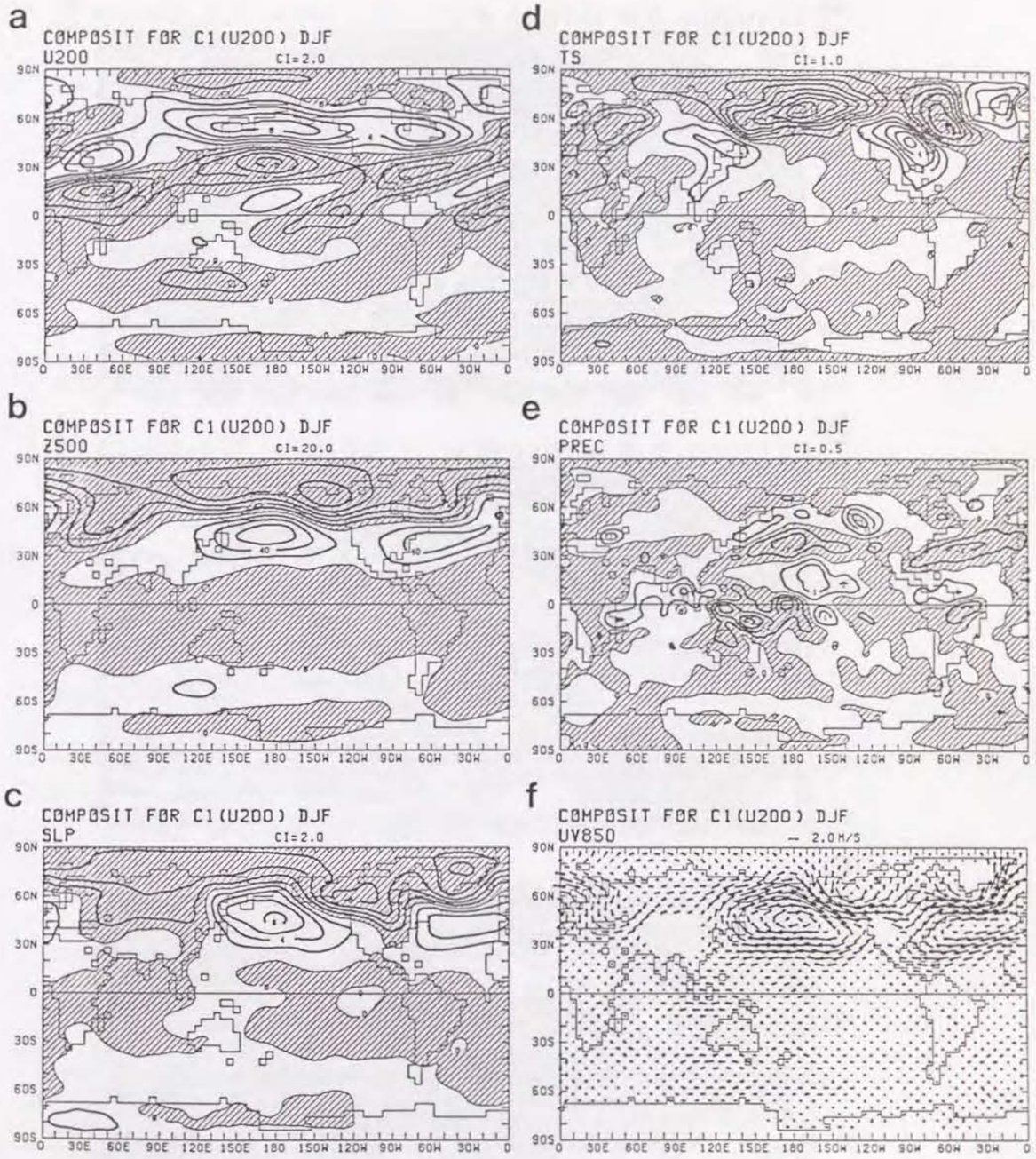

FIGURE 10

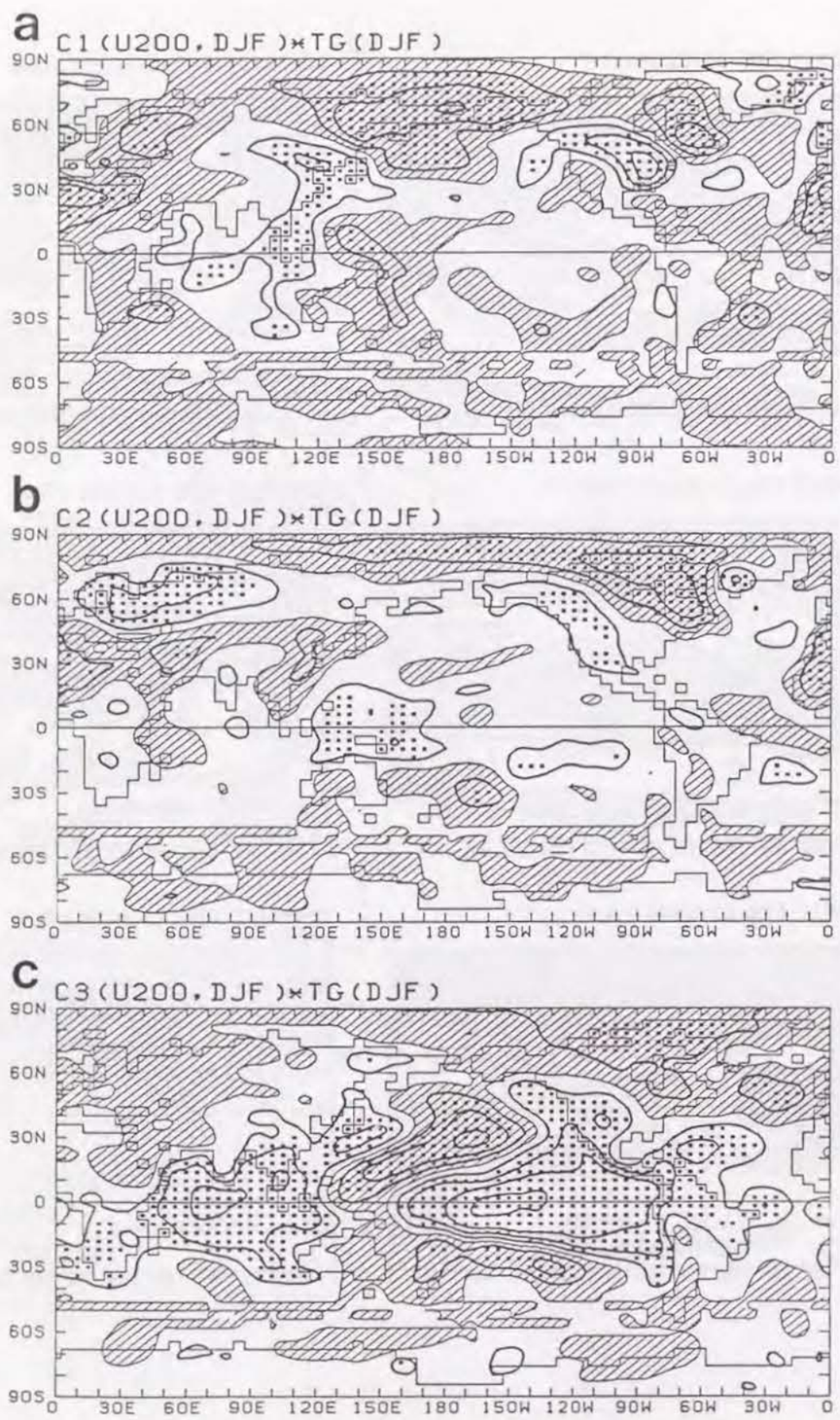

FIGURE 11

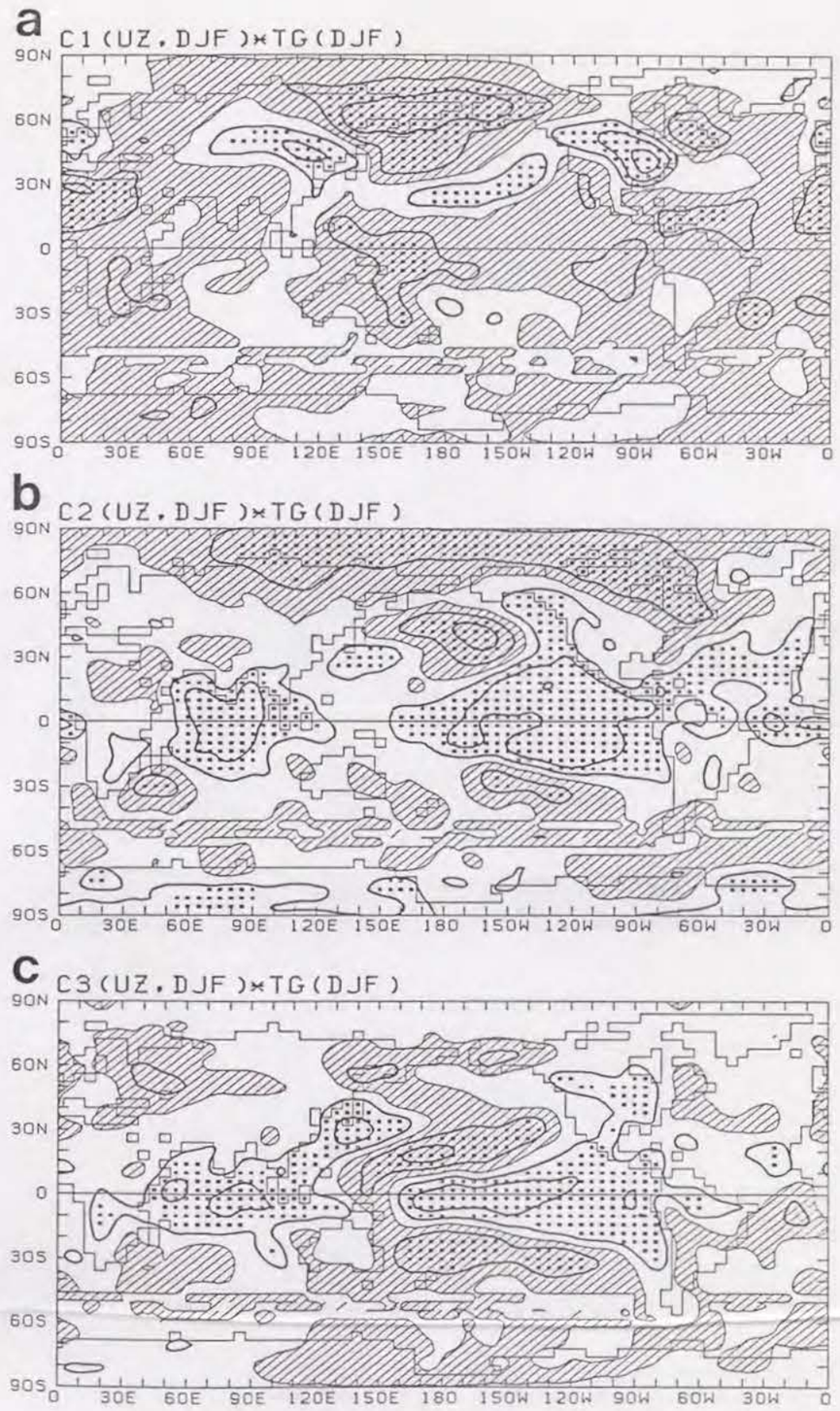

FIGURE 12